UNIVERSITY OF CALIFORNIA

Los Angeles

High-Throughput Tumor Organoid Models for Functional Precision Medicine

A dissertation submitted in partial satisfaction of the

requirements for the degree

Doctor of Philosophy in Bioengineering

by

Peyton John Tebon

2022

ABSTRACT OF THE DISSERTATION

High-Throughput Tumor Organoid Models for Functional Precision Medicine

by

Peyton John Tebon

Doctor of Philosophy in Bioengineering

University of California, Los Angeles, 2022

Professor Michael A. Teitell, Co-Chair

Professor Alice Soragni, Co-Chair

Precision medicine has the potential to revolutionize cancer care by identifying promising treatment strategies specific to each patient's disease. While advances in genome sequencing have facilitated the identification of mutations within tumors, only a small number of strict relationships between gene alterations and drug response have been established. Functional precision medicine is an emerging paradigm that exposes living patient-derived tissue to drugs to observe response. The work presented in this thesis will describe the development and implementation of high-throughput platforms for organoid screening. First, I will discuss the varied approaches that have been used to model tumors *in vitro*. Then, I will present our findings from screening organoids derived from 127 patients with sarcoma specimens collected at UCLA. Next, I describe the development of a pipeline for screening bioprinted organoids with high-speed live cell interferometry to enhance consistency and assess response to treatment with single-organoid resolution. Finally, I will detail the development of new methods for screening radiotherapy and liver-metabolized prodrugs on tumor organoids. This work contributes to the overall goal of creating robust, automated, and informative organoid screening pipelines for the implementation of functional precision medicine in clinical oncology.

The dissertation of Peyton John Tebon is approved.

Andrea M. Kasko

Noah C. Federman

Steven J. Jonas

Dino Di Carlo

Michael A. Teitell, Committee Co-Chair

Alice Soragni, Committee Co-Chair

University of California, Los Angeles

2022

To my wife, Shauna, for her endless patience and support

&

To my late grandparents, Joe and Karen, for being teachers and role models throughout my life

Table of Contents

List of Figures

Chapter 4

Chapter 5

Acknowledgements

I would like to acknowledge the colleagues, collaborators, and mentors that have supported this work and my personal growth throughout my training. Tyler Hoffman, Brooke Jackson, Dr. Marcus Goudie, Dr. Alberto Libanori, and Vishwesh Shah have pushed me to grow as a scientist and person while sharing unforgettable memories along the way. Dr. George E. Aninwene II and Dr. Renea Sturm have been indispensable friends and mentors that have continually provided support and new opportunities to learn. I would like to thank Dr. Ali Khademhosseini for recruiting me to UCLA, investing in my training, and preparing me for the opportunities to come. I would also like to extend special thanks to Dr. Steven Jonas and Dr. Andrea Kasko for their unyielding support during my transition into the Soragni Lab.

I am grateful for my colleagues in the Soragni Lab that have been fundamental in not only making this work possible, but also making it enjoyable. Dr. Ahmad Al Shihabi, Dr. Sara Sartini, and Huyen Nguyen were instrumental in helping me develop new skills in the laboratory while also becoming dear friends who generously supported me when I needed it most. I have learned immensely from each of them, and their generosity and care will not be forgotten. I would also like to acknowledge Bowen Wang for being a great friend and collaborator, his dedication to detail contributed to the rigor and success of our work. Dr. Ardy Davarifar was also an excellent mentor, colleague, and friend who pushed me to learn new skills and consider different points of view. Luda Lin and Dr. Jomjit Chantharasamee were wonderful colleagues that have made great contributions to our work and my learning, and Dr. Maite Calucho, Dr. Nasrin Tavanaie, Hillary

Vita

Education

Milwaukee School of Engineering	Bachelor of Science, BioMolecular Engineering
	BioMolecular Engineering Program Valedictorian
	Graduated with High Honors, May 2018
	Minors in Mathematics and Chemistry

Fellowships

UCLA Jonsson Comprehensive Cancer Center (JCCC) Fellowship - $10,000	2021-2022

Awards and Honors

UCLA Bioengineering Research Day – First Prize Oral Presentation	February 2022

Presentations

Invited Talks

"High-speed live cell interferometry captures heterogeneity in bioprinted tumor organoids." UCLA Bioengineering Research Day. University of California, Los Angeles. 11 February 2022.

"Bioprinting sarcoma organoids for precision medicine." UCLA Sarcoma Research Meeting. University of California, Los Angeles. 21 July 2021.

"Functional screening of tumor organoids for precision medicine." Orthopaedic Hospital Research Center Musculoskeletal Seminar Series. University of California, Los Angeles. 24 March 2021.

"Clinical and commercial applications of microfluidic organ-on-a-chip devices." Microfabrication and Microfluidics. Milwaukee School of Engineering. 20 December 2018.

Posters

Peyton Tebon, Bowen Wang, Alexander L. Markowitz, Graeme Murray, Ardalan Davarifar, Huyen Thi Lam Nguyen, Nasrin Tavanaie, Thang L. Nguyen, Paul C. Boutros, Michael A. Teitell, Alice Soragni. High-speed live cell interferometry captures heterogeneity in bioprinted tumor organoids. AACR Annual Meeting 2022. New Orleans, LA. 12 April 2022.

Ahmad Al Shihabi, **Peyton Tebon**, Jomjit Chantharasamee, Huyen Thi Lam Nguyen, Sara Sartini, Ardalan Davarifar, Nasrin Tavanaie, Scott Nelson, Noah Federman, Jane Yanagawa, Alice Soragni. A pipeline for functional precision medicine in bone and soft tissue sarcoma organoids. AACR Annual Meeting 2022. New Orleans, LA. 12 April 2022.

Peyton Tebon, Alice Soragni. Engineered mini-livers for high-throughput tumor organoid screening of prodrugs. AACR-NCI-EORTC International Conference on Molecular Targets & Cancer Therapeutics. Virtual. 25-27 October 2021.

Selected Publications

Peyton J Tebon*, Bowen Wang*, Alexander L Markowitz*, Ardalan Davarifar, Patrycja Krawczuk, Alfredo Enrique Gonzalez, Graeme Murray, Huyen Thi Lam Nguyen, Nasrin Tavanaie, Thang L Nguyen, Paul C Boutros, Michael A Teitell, Alice Soragni. (2022). High-speed

live cell interferometry for screening bioprinted organoids. Submitted, Nature Communications.

Ahmad Al Shihabi*, **Peyton J Tebon***, Huyen Thi Lam Nguyen*, Jomjit Chantharasamee, Sara Sartini, Ardalan Davarifar, Alexandra Jensen, Miranda Diaz-Infante, Hannah Cox, Alfredo Enrique-Gonzalez, Nasrin Tavanaie, Sarah Dry, Arun Singh, Bartosz Chmielowski, Joseph Crompton, Anusha Kalbasi, Fritz Eilber, Fran Hornicek, Nicholas Bernthal, Scott D Nelson, Paul C Boutros, Noah Federman, Jane Yanagawa, Alice Soragni. (2022). "The landscape of drug sensitivity and resistance in sarcoma organoids". In preparation.

Xing Jiang*, Li Ren*, **Peyton Tebon***, Canran Wang*, Xingwu Zhou, Moyuan Qu, Jixiang Zhu, Haonan Ling, Shiming Zhang, Yumeng Xue, Qingzhi Wu, Praveen Bandaru, Junmin Lee, Han-Jun Kim, Samad Ahadian, Nureddin Ashammakhi, Mehmet R. Dokmeci, Jinhui Wu, Zhen Gu, Wujin Sun, Ali Khademhosseini. (2021). Cancer-on-a-Chip for Modeling Immune Checkpoint Inhibitor and Tumor Interactions. Small 17, 2004282.

Christian D. Seger, Libing Wang, Xuezhi Dong, **Peyton Tebon**, Sebastian Kwon, Elaine C. Liew, Jure Marijic, Soban Umar, Nir N. Hoftman. (2020). A Novel Negative Pressure Isolation Device for Aerosol Transmissible COVID-19. Anesthia & Analgesia 131(3):664-668.

Xingwu Zhou, Moyuan Qu, **Peyton Tebon**, Xing Jiang, Canran Wang, Yumeng Xue, Jixiang Zhu, Shiming Zhang, Rahmi Oklu, Shiladitya Sengupta, Wujin Sun, Ali Khademhosseini. (2020). "Screening Cancer Immunotherapy: When Engineering Approaches Meet Artificial Intelligence." Advanced Science News 7, 2001447.

Tyler Hoffman, Petar Antovski, **Peyton Tebon**, Chun Xu, Nureddin Ashammakhi, Samad Ahadian, Leonardo Morsut, Ali Khademhosseini. (2020). "Synthetic Biology and Tissue Engineering: Toward Fabrication of Complex and Smart Cellular Constructs." Advanced Functional Materials: 1909882.

Kirsten Fetah*, **Peyton Tebon***, Marcus J. Goudie, James Eichenbaum, Li Ren, Natan Barros, Rohollah Nasiri, Samad Ahadian, Nureddin Ashammakhi, Mehmet Dokmeci, Ali Khademhosseini. (2019). "The emergence of 3D bioprinting in organ-on-chip systems." Progress in Biomedical Engineering 1(1): 012001.

Patents

Alice Soragni, **Peyton Tebon**, Bowen Wang, Nasrin Tavanaie, Luda Lin. *Tissue organoid bioprinting and high-throughput screening methodology.* 63/122,258. 2020.

Alice Soragni, **Peyton Tebon**. *Mini-liver insert for in vitro drug metabolism studies.* 63/122,275. 2020.

Nir Hoftman, Christian Seger, Sebastian Kwon, **Peyton Tebon**, Libing Wang. *The Vaccushield.* 63/008,114. 2020.

Peyton Tebon, Darin Williams. *Well plate and petri dish fluid exchange plug.* 62/988,840. 2020.

Renea Sturm, George E. Aninwene II, **Peyton Tebon**, Mohammad Ali Darabi. Alireza Khademhosseini. *Bio-Zipper surgical closure device.* 62/915,361. 2019.

Peer-Review

Molecular Biomedicine, July 2022

STAR Protocols, February 2022

Nature Communications Biology, February 2021

Chapter 1: Introduction to functional precision medicine

Precision medicine is based on the concept that each patient is unique and requires tailored treatment to achieve the best possible clinical outcomes[1,2]. Though precision medicine strategies are becoming commonplace in some aspects of clinical care[3], treatment decisions for patients with cancer are rooted in clinical trials examining the efficacy of therapeutic regimens across large patient cohorts[4]. Personalized medicine solutions tailoring treatment to individual tumors are attractive, especially given the enormous heterogeneity found across patients[5–10], amongst tumors from the same patient[11–13], and even within individual lesions[11–14]. Traditionally, these techniques have tailored treatment to individuals based on genetic aberrations found through sequencing[15]. While advances in next-generation sequencing have facilitated the identification of mutations within tumors, only a small number of actionable alterations, genetic aberrations with a well-defined relationship to patient response to a specific drug, have been established[16].

One of the major studies investigating these relationships is the NCI-MATCH trial. The NCI-MATCH trial is a landmark Phase II clinical trial that is designed to investigate the genomic precision medicine approach to cancer treatment[17,18]. Each tumor is screened for genetic aberrations and patients are assigned to a trial arm that matches a targeted therapy to their specific abnormality. Though any cancer patient that has failed at least one prior line of therapy qualifies for enrollment, the proportion of patients harboring the aberrations of interest are relatively low (**Figure 1.1**). Amongst study arms with results available, the range of genetic aberration prevalence was 0.03% (ALK translocations) to 3.47% (PIK3CA mutations) in the cancer patient population[19]. The scarcity of actionable mutations significantly limits the number of patients that can benefit from the genomic precision medicine approach. The more sobering finding, however, has been the broad lack of efficacy of the targeted treatments. Across the 20 trial arms with publicly available results, only four have met the primary benchmark of a 16%

overall response rate[20–23]. Several of the trial arms failed to see a complete or partial response in a single patient (**Figure 1.1**) [24–27]. While this trial does have limitations such as a pretreated patient population, relatively low power in individual subprotocols, and a limited set of targeted drugs for the genetic abnormalities found, the lackluster results demonstrate that genomic precision medicine, in its current form, is largely ineffective. For the majority of cancer patients, genomic analyses are unable to inform clinical decisions regarding treatment (**Figure 1.1**) [28–30].
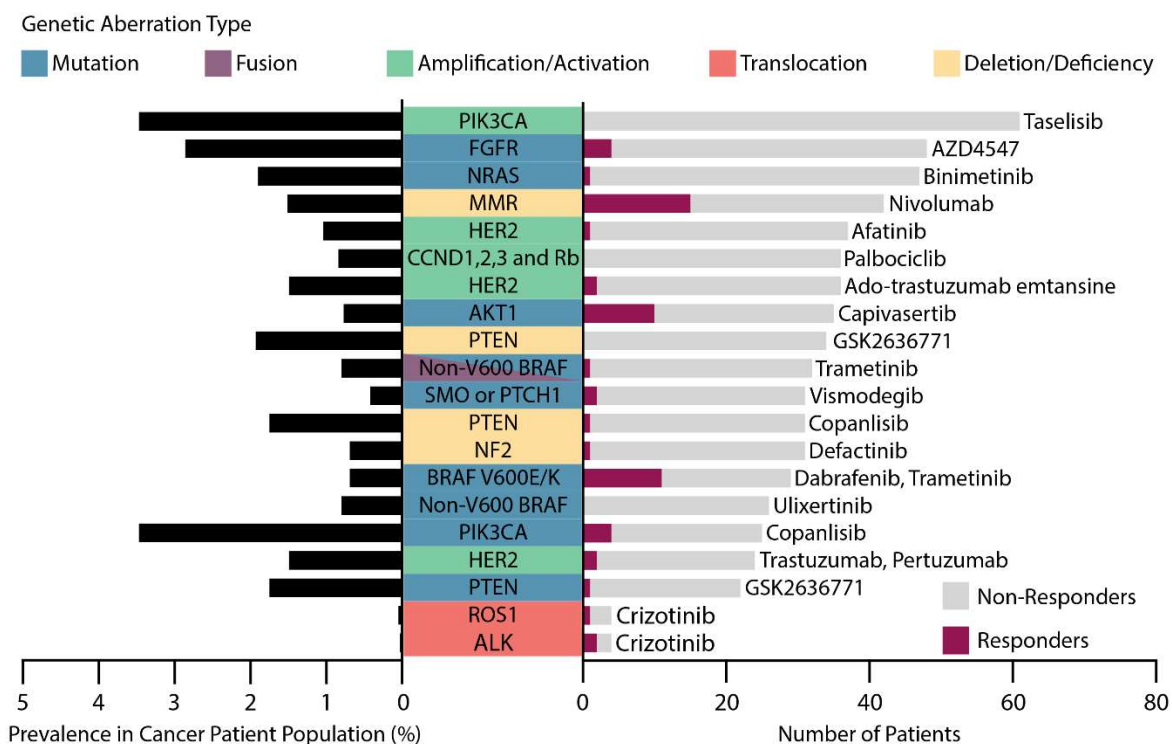
Figure 1.1: Summary of current NCI-MATCH Clinical Trial results. The NCI-MATCH trial is a Phase II clinical trial investigating the efficacy of drugs within a cohort of pretreated cancer patients. Arm assignment is exclusively based on the presence of pre-specified genetic characteristics of patient tumors. The prevalence of each mutation found within the first 6000 patients screened in the NCI-MATCH trial (left). The number of responsive versus non-responsive patients for each trial arm based on data available for completed trial arms as of September 16, 2022 (right).

Despite the underwhelming results based on genomic insights, new approaches to precision medicine, including functional assays, have shown promise[31,32]. Functional precision

medicine differs from traditional genomics-based personalized medicine in that it exposes living patient-derived tissue to drugs to observe response[33]. One model used for this purpose is patient-derived tumor organoids. Tumor organoids are three-dimensional (3D), multicellular tissue constructs representative of native cancer physiology and histopathology[33–35]. Compared to two-dimensional (2D) cell cultures, 3D models better recreate cell-matrix and cell-cell interactions and generate more representative phenotypes, gene expression profiles, and responses to treatment[36–38]. The leading in vivo models used for personalized drug testing are patient-derived xenografts (PDXs); these are generated by injecting patient cells into immunodeficient animals (most often mice)[33]. While PDX models have been shown to recapitulate patient response to therapy[39], they become less representative over time due to genetic mutations and clonal selection[40] and are resource-intensive, requiring months to yield potentially actionable information[33]. The key to implementing functional precision medicine into clinical oncology lies within the development of high-throughput systems for the creation, screening, and analysis of personalized tumor models.

This doctoral thesis describes progress towards making such a platform a reality. In the coming pages, I will discuss the diverse approaches taken to model tumors, the utility of organoids in functional precision medicine for sarcoma patients, a platform that synergizes bioprinting and high-speed live cell interferometry for organoid screening, and additional work towards expanding functional screening to different treatment modalities.

Chapter 2 features a section from Kirsten Fetah*, Peyton Tebon*, Marcus J. Goudie, James Eichenbaum, Li Ren, Natan Barros, Rohollah Nasiri, Samad Ahadian, Nureddin Ashammakhi, Mehmet Dokmeci, Ali Khademhosseini. (2019). "The emergence of 3D bioprinting in organ-on-chip systems." Progress in Biomedical Engineering 1(1): 012001. I wrote and edited the featured section under the direction of corresponding author and principal investigator Ali Khademhosseini.

Chapter 3 is a version of Ahmad Al Shihabi*, Peyton J Tebon*, Huyen Thi Lam Nguyen*, Jomjit Chantharasamee, Sara Sartini, Ardalan Davarifar, Alexandra Jensen, Miranda Diaz-Infante, Hannah Cox, Alfredo Enrique-Gonzalez, Nasrin Tavanaie, Sarah Dry, Arun Singh, Bartosz Chmielowski, Joseph Crompton, Anusha Kalbasi, Fritz Eilber, Fran Hornicek, Nicholas Bernthal, Scott D Nelson, Paul C Boutros, Noah Federman, Jane Yanagawa, Alice Soragni. (2022). "The landscape of drug sensitivity and resistance in sarcoma organoids". I was responsible for the conducting experiments, performing data analysis, and preparing the manuscript under the direction of principal investigator Alice Soragni.

Chapter 4 is currently under review at Nature Communications as Peyton J Tebon*, Bowen Wang*, Alexander L Markowitz*, Graeme Murray, Huyen Thi Lam Nguyen, Nasrin Tavanaie, Thang L Nguyen, Paul C Boutros, Michael A Teitell, Alice Soragni. (2022). High-speed live cell interferometry for screening bioprinted organoids. Submitted, Nature Communications. I was responsible for conducting experiments, developing analytical methods, and preparing the manuscript under the direction of co-corresponding authors Michael Teitell and Alice Soragni.

Chapter 5 is original work conducted with Miranda Diaz-Infante, Hannah Cox, Jie Deng, Scott Chin, and Anusha Kalbasi under the direction of principal investigator Alice Soragni. This collective body of work joins that of millions of scientists, engineers, and clinicians across the globe searching for ways to combat cancer and improve patient lives.

Chapter 2: Studying cancer through tumor models

"All models are wrong, but some are useful."

-George Box, 1987

Models provide a method to simplify the complexity of intricate systems into approximations that are easier to understand and easier to use. When it comes to the abstraction of biological systems for the purpose of investigating tumors, the models that have been developed are abundant and diverse[41–43]. From basic 2D cell cultures to microfluidic systems, tumor models have supported the investigation of tumor physiology and have played an integral role in moving treatments from bench to bedside. Each model has unique utility and may be suitable for investigating specific biological questions. Simple models, though not entirely representative of native tissue, are typically easier to handle, sample, and analyze[44,45]. More complex models may allow the interrogation of cellular behavior in niche biological environments, but often come with added economic and usability costs[45]. In theory, the simplest model that can accurately answer the scientific question is the best choice. In practice, the diversity in the models implemented is demonstrative of the varying opinions on the fine line between too simple and too complex. The remainder of this chapter provides an overview of the commonly used tumor models and their respective roles in understanding cancer (**Figure 2.1**).
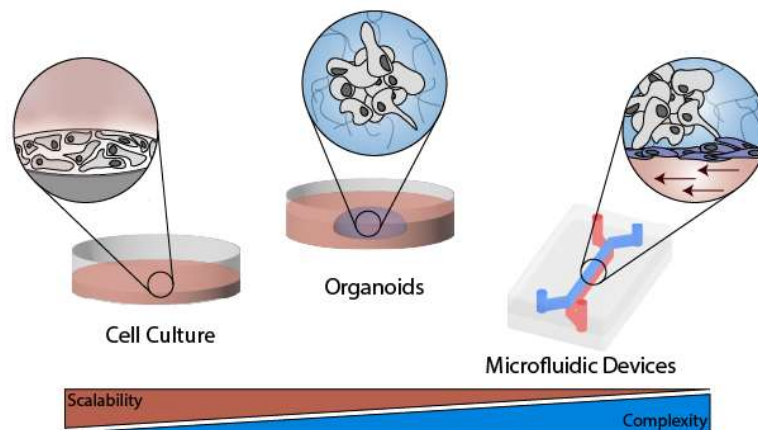
Figure 2.1: *In vitro* models of cancer. Cancer cell lines cultured in 2D are widely accessible and easy to scale but lack the complexity of native tissue. Microfluidic devices are capable of recapitulating specific microenvironmental features but are often used in low-throughput settings. Organoids are a 3D alternative that balance the scalability of 2D models while maintaining some of the complexity in microfluidic devices.

Two-dimensional cell culture

Though 2D cell cultures were central to the development of our current understanding of tumors[44], the utility of these cultures has diminished due to their limited capability to recapitulate typical physiological behavior[45]. As the simplest tumor model used in research, cell lines cultured on treated glass and plastics have the benefits of being inexpensive, broadly accessible, and amenable to high-throughput techniques[44,45]. These models fall short in capturing the genetic heterogeneity of tumors[45] and fail to recreate physiologically relevant microenvironments that are fundamental to *in vivo*-like cell behavior[46,47].

Several studies have investigated whether *in vivo* response of patient-derived cell lines to treatment correlate with clinical outcomes for the patient[48,49]. For example, Wagner et al. studied a small cohort of colorectal cancer patients by screening commonly used chemotherapies[48]. The results were mixed, as one cell line correctly predicted patient response patient to 5-FU and oxaliplatin but another failed to predict the resistance of a second patient to 5-FU and irinotecan. Brodin et al. conducted a similar study investigating the utility of patient-derived cell lines from bone and soft-tissue sarcomas[49]. While the cell lines derived from the specimens maintained the genetic mutations unique to each tumor in early passages, these unique features were lost over extended culture times. Patient-specific drug response profiles were observed, and the cell lines were largely able to predict the negative clinical responses of patients to standard-of-care drugs.

Though there is a strong argument to be made for the utility of using broad panels of cancer cell lines for the identification of new drugs and early pre-clinical testing[44], the data

collected thus far on the use of patient-derived cell lines for precision medicine suggests that these models may be too simple to successfully predict patient-response to treatment.

Organoid models

Tumor organoids are multicellular, three-dimensional constructs that incorporate both cell-cell and cell-matrix interactions found in physiological conditions[50]. Standard organoid models typically involve the suspension of tumor cells harvested from cell lines or derived from primary tissue in a hydrogel matrix[46,51]. Traditional organoid cultures are centered around hydrogel droplets deposited in well plates cultured over extended periods of time. The theory is that given sufficient time, space, and nutrients, these suspended cells will self-assemble into the tissue-mimicking structures known as organoids[47,52]. Organoids have been developed for both healthy and diseased models, both of which have been shown to recapitulate key structures and functions of the native tissues[47,52,53]. This added complexity makes them an attractive candidate for modelling cancer as they better match the behavior of native tissue compared to 2D cell cultures[45] with marginal increases in cost and difficulty of use. Organoids have been developed for a variety of cancer types including colorectal[54–60], sarcoma[10,61], breast cancer[6,62], head and neck cancer[46,63], and ovarian cancer[9,64].

Given their enhanced ability to model native tissue and relative ease to work with, the use of organoids has exploded in recent years. Because of their ability to recapitulate the molecular, histological, and behavioral features of the tissue of origin, many groups have investigated the utility of organoids to predict patient response to therapy; a thorough review of these studies to date has been published by Wensink et al[51]. Based on the data available thus far, organoids have great promise to revolutionize clinical cancer care. For example, Vlachogiannis et al. demonstrated that organoids representing colorectal and gastroesophageal cancers matched patient clinical outcomes when treated with regorafenib. These organoids resulted in 100%

sensitivity and 93% specificity with 88% positive predictive value and 100% negative predictive value[59]. Yao et al had similar findings from a larger cohort of patients and found the organoids to be 84.43% accurate, 78.01% sensitive, and 91.97% specific when it came to matching chemoradiation outcomes clinically[65].

Organoids also have the potential to go beyond investigating chemotherapies and targeted drugs. Forsythe, et al developed a platform to seed immune-competent sarcoma organoids in a hyaluronic acid and collagen-based hydrogel for drug screening purposes. They included three immunotherapies in their drug screening panel (pembrolizumab, nivolumab, and ipilimumab) and found two unique responders to nivolumab and four responders to pembrolizumab[61]. In another example, Park et al. developed rectal cancer organoids for screening radiotherapy. This study is one of several that demonstrates the feasibility of radiating organoids for precision medicine applications. They found that the organoids not only recapitulated the characteristics of the parent tumor, but also showed a positive correlation with patient response to radiation[60].

Organoids represent a powerful and versatile model for studying patient-specific response to treatment across a variety of therapeutic interventions. As a result of the promising findings published thus far, clinical trials are underway aiming to rigorously characterize the fidelity of organoids at recapitulating patient-specific features and assess their predictive value as a biomarker (for example, NCT04555473, NCT04859166, NCT05351983, and NCT04931381). Should these trials provide additional evidence to support the clinical use of organoids to gain actionable information, organoids are poised to play a foundational role in the future of precision cancer care.

Microfluidic models

Organ-on-chip platforms are fluidic devices containing organized biological structures that emulate the physiological function, behavior, and response of their analogous organs in the human body[66,67]. While there is extensive diversity amongst organ-on-chip platforms, each of them shares the same goal: to recreate the structure and physiological behavior of human organs outside of the body. Though organ-on-chip systems can be used to recreate healthy tissue, extensive effort has also been devoted to recreating diseases within microfluidic devices[68,69]. Perhaps the most well studied disease with organ-on-chip technology is cancer. Cancer-on-chip systems are designed for three main purposes: to understand the role of the tumor microenvironment in cancer progression, to study the biological processes associated with metastasis, and examine the efficacy of drug therapies. While the governing phenomena of these three areas vary greatly, the use of microfluidic devices allows customized geometries that facilitate the study of specific biological and environmental factors in each domain. Most microfluidic devices study recreated 2D tissue interfaces, which allow optimal observation of artificially created gradients and cell mobility. Though they are easy to observe, 2D models do not incorporate the necessary 3D architecture and cellular interactions that are prerequisites for demonstration of physiologically relevant behavior[70,71]. The tumor spheroid has been the most widely adopted 3D construct for studying each factor as they are easy to observe, provide quantitative data, can be composed of several cell types, produce their own ECM, and can exhibit metastatic events[70]. These spheroids have been studied in a variety of environments ranging from well plates to microfluidic devices and have potential to contribute to precision oncology.

The application of cancer-on-chip models for drug screening may yield excellent tools for the development of high-throughput assays used to identify compounds as potential drugs or to evaluate the toxicity and efficacy of existing pharmaceuticals[72]. While current industrial practice primarily uses 2D culture systems and research is being conducted on well-based spheroid

assays[73], microfluidics has the potential to revolutionize drug screening. Lab-on-chip platforms such as the system developed by Yu et al show potential for creating 3D cell aggregates for drug screening[74]. This device both creates the aggregates and organizes them into an easily observable array of breast cancer models for pharmaceutical testing. Another device created by Fan et al formed and analyzed glioblastoma multiform (GBM) spheroids in a poly(ethylene) glycol diacrylate (PEGDA) chip[75]. This system facilitated the study of concurrent application of two common anti-GBM drugs, pitavastatin and irinotecan, and observed cell detachment and death on the surface of the spheroids. With the increased complexity of microfluidic systems comes greater diversity in the models developed and the research questions addressed with each one; this topic is comprehensively reviewed in Fetah, Tebon, et al[41].

Though the number of clinical trials implementing organ-on-chip devices for precision oncology is limited, there are ongoing studies evaluating the utility of microfluidic models in formulating custom treatment regimens for patients with cancer (NCT04996355). The early success of organoids has drawn attention from sophisticated cancer-on-chip devices for personalized tumor models thus far, but these models have maintained interest due to their unique ability to recreate controlled physiological microenvironments to study the multiple aspects of cancer progression.

Chapter 3: The utility of 3D organoid models in sarcomas

One of the primary goals of our work was to establish the feasibility and utility of patient-derived organoids as a means for providing clinically actionable information. We focused our effort on studying bone and soft tissue sarcomas, a family of rare malignancies with enormous heterogeneity[7–9,76] and persistently low 5-year survival rates[77]. Given the scarcity of tumor models for bone and soft tissue sarcomas, studying the underlying biology and identifying effective therapies remain difficult. Patient-derived tumor organoids (PDTOs) are representative of the native physiology of tumors across an array of malignancies, including sarcoma[9,10]. For patients diagnosed with bone and soft tissue sarcomas, these organoids can be used as an important tool to better understand their disease and identify treatments most likely to be effective. We collected tumor specimens from 127 patients diagnosed with sarcomas, spanning 25 distinct subtypes of these rare tumors. We generated organoids from over 100 samples collected from biopsies, resections, and metastasectomies. We use our mini-ring platform[9,78] to create an array of three-dimensional tumor models for high-throughput drug screening aimed at identifying drug susceptibilities of chemotherapeutics, targeted agents, and combination therapies. Here, we describe our organoid pipeline from sample procurement to organoid analysis. We share our findings from screening sarcoma organoids with a drug library of over 500 compounds and assess drug sensitivity across cancer types and patient demographics. Our findings further support the feasibility of generating organoid models from bone and soft tissue sarcomas to facilitate drug discovery and predict patient response to treatment, especially in the context of rare sarcoma subtypes. Furthermore, we demonstrate that functionally testing organoids derived from clinical specimens provides actionable information to clinicians selecting treatment regimens. Our work is exemplary of the potential of functional precision medicine to provide additional insight into the biology of rare tumors that may contribute to improving patient outcomes.

Introduction

Sarcomas are a family of rare and heterogeneous tumors of mesenchymal origin[79]. Clinically, these tumors primarily present in bone and soft tissue and disproportionately impact young patients[79–81]. Despite a low case count, with ~13,000 soft tissue sarcoma and ~4,000 bone sarcoma diagnoses annually in the United States[81], fatalities remain high. Bone sarcomas for instance are the third leading cause of cancer deaths in patients under 20 years old[81]. The treatment regimen varies greatly by disease subtype and stage; therapeutic options include surgical resection, chemotherapy, targeted systemic therapy, and radiotherapy in certain cases[1,2]. Despite some significant advances for specific subtypes, current treatment approaches are rarely curative and contribute to aggregate overall 5-year survival rates of ~65% in soft tissue sarcoma and ~50-60% for bone cancers.

The heterogeneity of sarcoma manifests in over 100 distinct subtypes. Diversity is observed across and within sarcoma diagnosis: for instance, classifications include over 10 distinct osteosarcoma subtypes. About a third of sarcoma cases are driven by specific chromosomal fusions, such as subsets of Ewing sarcoma, synovial sarcoma, infantile fibrosarcoma and rhabdomyosarcoma[82]. Other key genetic events across bone and soft tissue sarcomas are thought to impact cell cycle regulation, growth factor signaling, and angiogenesis[83]. Specific high-prevalence mutations include RTK/RAS driver mutations among epithelioid sarcomas[84], CDK aberrations in liposarcomas[84], and PI3K mutations in PEComa and myxoid liposarcomas[84]. This vast heterogeneity compounds the challenge to identify effective regimens for this family of rare and ultra-rare cancers and contributes to persistently low survival rates.

Precision medicine approaches are attracting increasing interest as tools to identify actionable characteristics and improve outcomes on a per-patient basis[85]. Technologies such as next-generation sequencing (NGS) and immunohistochemistry are widely used to identify

molecular alterations and druggable targets[85–87]. In the case of fusion-positive sarcoma, most of the aberrant oncogenes cannot be targeted directly, with the notable exception of NTRK[82]. Studies have evaluated the theoretical utility of NGS findings in 6'693 patients with bone and soft tissue sarcomas and found an average of ~42% of tumors harboring actionable alterations[85]. Despite this, few sarcoma patients show clinical benefit when treated with drugs selected via NGS[83,85,88,89].

Because of this genetic diversity and the limited efficacy of chemotherapeutic and targeted agents both in the conventional or precision medicine setting, alternative approaches are needed to both evaluate the landscape of drug sensitivity and resistance in sarcoma and to identify individualized therapeutic solutions. Here, we leverage patient-derived tumor organoid-based functional assays as an alternative yet complementary approach to genetic-based precision medicine in sarcoma[78]. Previous studies have shown that patient-derived organoids (PDTOs) are an effective model to predict response to treatment for patients with various types of epithelial cancers[58,59,90–94]. The development of sarcoma PDTOs has lagged, with limited applications so far[95,96].

We have procured n=193 specimens from n=127 patients undergoing biopsies or surgical resections at UCLA Health hospitals and successfully generated PDTOs from over 100 samples so far originating from primary, recurrent, or metastatic bone and soft tissue sarcomas. Here we describe our pipeline in procuring and generating sarcoma PDTOs and we characterize both the parent tumor and PDTO through histopathology, genetic sequencing and high-throughput drug screening to gain insight on the biology of rare sarcomas. By performing high-throughput drug screening on the generated organoids we can identify patient-specific and subtype specific vulnerabilities. We discuss the trends of drug sensitivity and resistance that we have observed

across the landscape of sarcoma samples and highlight the heterogeneity of sarcoma drug sensitivity. We also discuss the utility of these organoids for sarcoma precision medicine.

Results

Sarcoma Patient Characteristics

We collected a total of n=193 sarcoma specimens between February 2018 and May 2022 from 127 patients treated at UCLA for a sarcoma diagnosis (**Figure 3.1**). Tissue was obtained from biopsies (n=10) or surgical resections (n=183) of primary, recurrent, and metastatic lesions (**Figure 3.1A and 3.1B**). The patient population was majority adult (n = 65/127) with 35% of patients in the adolescent and young adult (AYA) age group (n = 45/127) and 13% of pediatric patients in the pediatric cohort (n = 17/127) at time of diagnosis (**Figure 3.1B, Figure S3.2**). We collected samples from 79 (62%) male and 48 (38%) female patients, which closely resembles the proportion of incidence of bone and soft tissue sarcomas in the United States (57% male, 43% female)[77]. While the majority of patients identified as white, 15% identified as Asian, 5% as Black, 1% as Pacific Islander: Samoan and 18% as other.

Our study includes tumor samples from 25 distinct subtypes of bone and soft tissue sarcomas. The most common diagnosis in this cohort is osteosarcoma, for which we collected 72 samples from 28 patients, followed by chordoma (14 samples from 10s patients), chondrosarcoma (13 samples from 12 patients), and leiomyosarcoma (12 samples from 10 patients) (**Figure 3.1C**). The proportion of patients enrolled generally reflects the proportional incidences of the major subtypes with the exceptions of chordoma (over-represented in our study) and leiomyosarcoma (under-represented in our study)[97].

In 20% of cases (n = 26 patients), we collected multiple specimens from the same patient, either from different anatomical locations (12/26), time (20/26) or both (6/26). We collected

samples from metastatic and primary lesions most frequently, composing 45% and 42% of our specimens, respectively, while recurrent tumors represent 13% of the total. The tumors in this study were heavily pretreated with only 31% (n = 59/193) naïve to systemic treatment and 22% (n = 43/193) of tumors exposed to three or more prior lines of systemic therapy. Most tumors (70%) were treated with various systemic regimens while 30% were treated with radiotherapy (**Figure 3.1D**). The proportion of tumors treated with each modality varied widely across diagnostic subtypes, reflecting the heterogeneity in the clinical management of each unique sarcoma subtype (**Figure 3.1E**)[1,2]. For instance, myxoid liposarcomas are commonly known for their radiosensitivity and are treated with radiation pre-operatively which is captured in all of the myxoid liposarcoma specimens we have procured (**Figure 3.1E**)[98].
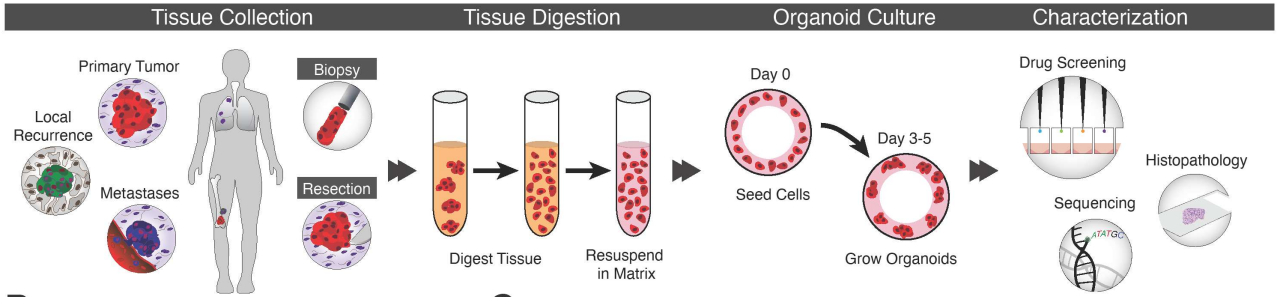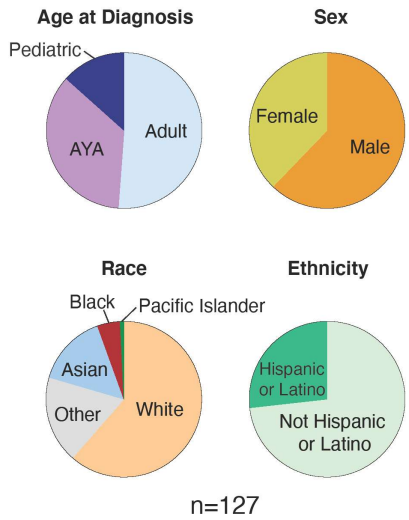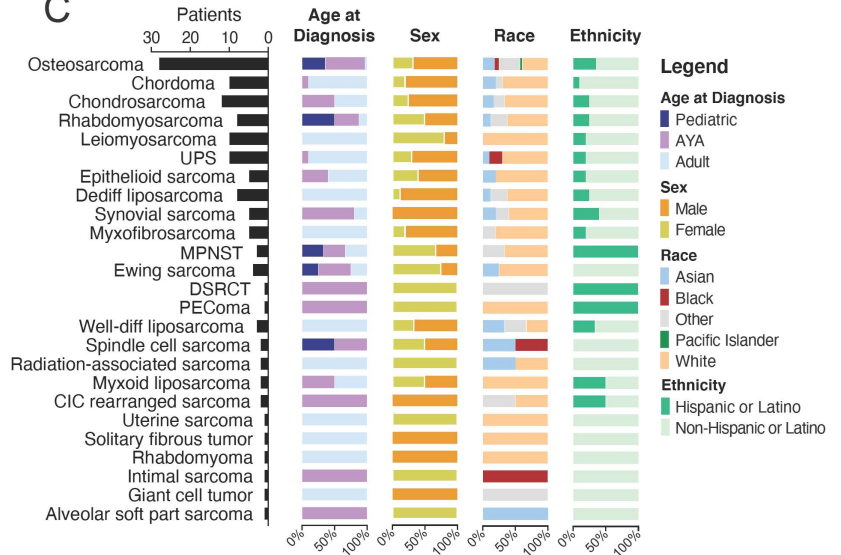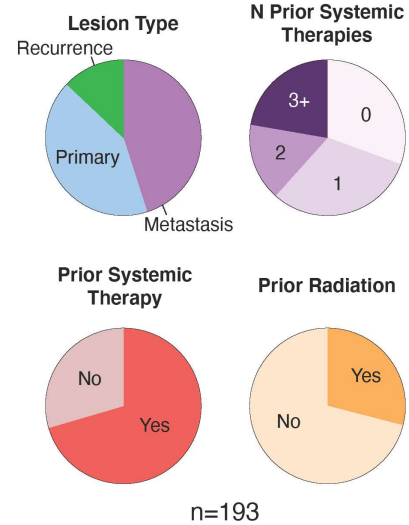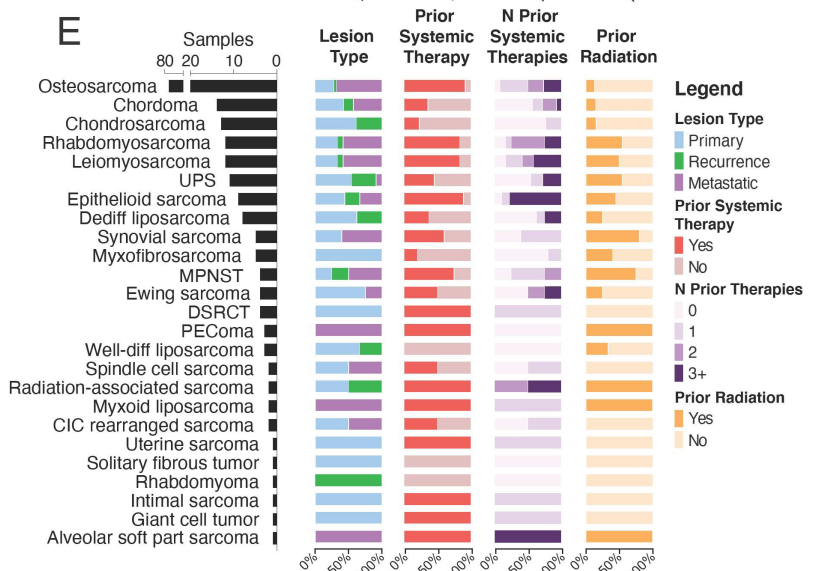
Figure 3.1: Overview of the patient-derived tumor organoid pipeline, patient demographics and sample characteristics. (A) Tissue is collected from biopsies or surgical resections of bone and soft tissue sarcomas. Organoids are generated by digesting the tissue and culturing the harvested cells in a 3D matrix. Organoids are molecularly and functionally profiled. **(B)** Demographics of pan-sarcoma study patients. Pediatric: 0-14 years old, AYA: 15-39 years old, adults: 40 years old and above. **(C)** Demographics divided by diagnosis. **(D)** Clinical characteristics of tumors from which tissue was collected. Prior systemic therapies include chemotherapy, targeted agents, and immunotherapy. **(E)** Tumor characteristics divided by disease subtype.

PDTOs can be routinely established and characterized for both soft tissue and bone sarcoma.

We processed the tissue according to our published protocols and described in the Methods section (**Figure 3.1A**)[78,95,99–101]. We built a custom relational model database to store and organize the high-throughput screening results along with the clinical attributes of the patients and specimens we procured (**Figure S3.1**). The analytical pipeline includes data from external databases such as PubChem[102] and WikiPathways[103] for data analysis purposes[95] (**Figure S3.1**).

We assessed the histopathology of both parent tumors and organoids (**Figure 3.2**). We observed diverse histopathological features across the sarcoma subtypes, such as small round blue cells in Ewing sarcoma, vacuolated cells with round nuclei in chordoma, and spindle cells in rhabdomyosarcoma, some types of osteosarcoma and malignant peripheral nerve sheath tumor (MPNST, **Figure 3.2**). Thin, hyperchromatic nuclei were visible in MPNST while heterogeneous nucleus sizes and structures were found in undifferentiated pleomorphic sarcoma (UPS). Across all subtypes, the organoids largely recapitulate all the salient features of the native tissue (**Figure 3.2**). For instance, both organoids generated from small cell osteosarcoma and Ewing Sarcoma show the characteristic small, round nuclei, with Ewing sarcoma organoids capturing the ambiguous cytoplasmic borders found in the native tissue. Consistent with our prior work[95],

chordoma organoids grew in clusters with extensive production of vacuoles as seen in the parental tumors.

Daily brightfield imaging provided the opportunity to monitor organoid morphology and to quantify growth[95] (**Figure 3.2**). We used a high-content imaging system to scan each plate once every 24 hours and monitor organoid behavior and then assessed growth by applying a U-net based machine learning-based segmentation approach that quantifies the cross-sectional area occupied by organoids[95,104] (**Figure 3.2**). We observed four distinct growth patterns. Organoids derived from UPS, LMS, and chordoma had minimal increases in normalized area after five days as the cells showed a tendency to change morphology and aggregate with neighboring cells with less pronounced proliferation. This is in line with what we have previously observed for chordoma organoids, with cell rearrangement and limited proliferation in PDTOs established from multiple patients[95]. Exponential growth was observed in myxofibrosarcoma, RMS, epithelioid sarcoma, and CIC-rearranged sarcoma PDTOs. Simultaneous aggregation and proliferation of the organoids leads to extensive networks of multicellular clusters with large cross-sectional areas (**Figure 3.2**). Ewing sarcoma organoids show a variation of the exponential growth profile as growth increases exponentially between days one and three and then plateaus in days four and five of culture. These organoids show the unique behavior of proliferating while also maintaining the characteristic round morphology observed clinically. Finally, we observed a set of PDTOs with near-linear growth dynamics. These included MPNST, well-differentiated liposarcoma, and small cell osteosarcoma (**Figure 3.2**).

Overall, our data suggests that PDTOs established from very different soft and bone sarcoma subtypes maintain the key histological characteristics of the tumor of origin while exhibiting unique morphological characteristics and growth dynamics. This suggests that PDTOs

maintain histology-specific and patient-specific tumor-specific within our standardized approach for organoid culture.
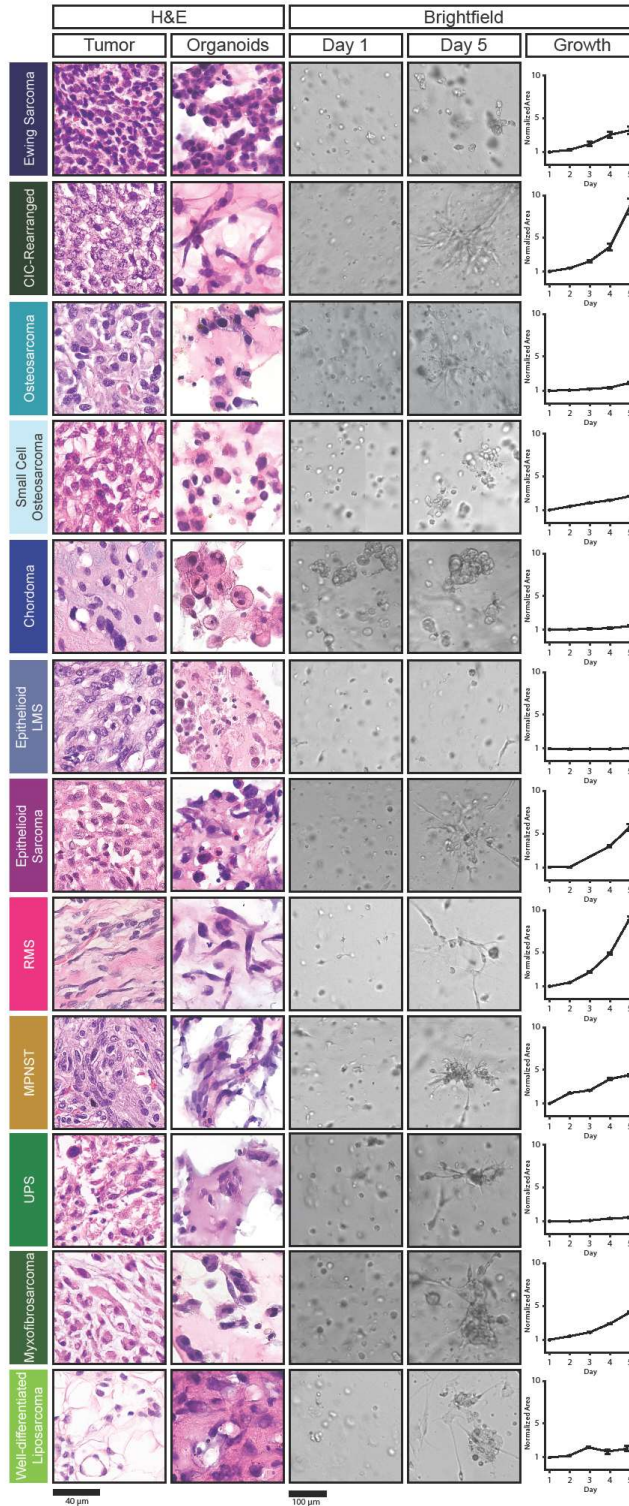
Figure 3.2: Sarcoma organoids grow in culture and recapitulate key morphological features of the parental tumors. Representative images of sarcomas and corresponding organoids stained with H&E (columns 1 and 2). Representative brightfield images of the same sarcoma cells in culture on Day 1 (column 3) and Day 5 (column 4). Growth was tracked over time by segmenting in-focus organoids in the brightfield images using a machine learning-based pipeline and by normalizing the cross-sectional area covered by organoids to that measured on the first day of culture. Scale bars: 40 µM for H&E images, 100 µM for brightfield pictures.

The landscape of drug sensitivity in sarcoma.

We performed high-throughput drug screenings on n=127 samples, encompassing 19 different sarcoma diagnoses. The drug library used includes up to 500 drugs in different stages of development such as FDA approved, in clinical trials or pre-clinical development[95,99,101]. For each sample, we personalized the panel of drugs to be screened on the basis of on *a priori* information and clinical data. We considered diagnosis, suspected or confirmed genetic alterations, anticipated clinical course of treatment, regimens in clinical trials for the indication and drugs of interest to the treating oncologist. Sarcoma PDTOs were tested for sensitivity against both monotherapy chemotherapeutic or targeted agents and clinically relevant combination therapies such as sorafenib and everolimus, gemcitabine and docetaxel, and methotrexate, doxorubicin, and cisplatin (MAP) (**Figure 3.3**). We used the Z' factor and robust Z' factor to assess the quality of drug screening results[105,106]. To reduce the likelihood of identifying false positive and negative results, we included plates with a Z' factor or robust Z' factor greater than 0.2 in downstream analyses (**Figure S3.3**). This filter includes 231 plates, corresponding to 75% of all screened samples.

To investigate the spectrum of organoid responses to treatment with a given drug, we normalized organoid viability for each sample to the mean viability of all samples treated with the drug of interest at the same concentration, in this case 1 µM (**Figure 3.3A**). This was done to

reduce the impact of broadly cytotoxic drugs and more easily identify the exceptional responders to each treatment[107]. As corroborated by previous studies[95,99], we identify unique sets of organoids sensitive to each therapy. This suggests that the functional response of organoids to treatment yields useful information for gaining additional insight into tumor-specific behaviors that cannot be found through histopathology and molecular analyses alone.

Everolimus is a commonly used mTOR inhibitor that has shown modest effect across a variety of bone and soft tissue sarcomas[108]. Our drug screening results indicate that the most sensitive organoids were derived from different metastatic lesions of an epithelioid sarcoma patient (SARC0075_4 and SARC0075_1). The organoids showed 51.4% and 51.5% viability relative to the mean response of 77 total samples screened. Despite the efficacy of the drug on these samples, organoids derived from other epithelioid sarcoma patients showed modest sensitivity (SARC0075_2 and SARC0128) or relative resistance to therapy (SARC0078_1 and SARC0005) (**Figure 3.3A**). Alternatively, organoids derived from chordoma and chondrosarcoma samples composed four of the five most resistant samples to treatment (Figure 3A). When comparing the drug screening results of everolimus to another mTOR inhibitor, rapamycin, we observe a similar, but distinct, set of specimens among the top responders. Organoids from SARC0129, SARC0137, SARC0017, SARC0024B, SARC0039, SARC0010_2 and SARC0135_2 appear in the top quartile of responders to both everolimus and rapamycin. However, organoids derived from SARC0133 and SARC0014 show remarkable sensitivity to rapamycin, and rank among the most resistant samples treated with everolimus. High-throughput drug screening on organoids has the unique ability to identify unexpected patterns in response to treatment with similar mechanisms of action across subtypes, in addition to individually identifying samples that exhibit heightened sensitivity or resistance to a therapeutical agent.

Analyzing the relative viability of samples also allows us to detect exceptional responders to specific drugs. For example, SARC0021, a synovial sarcoma, was found to be the most sensitive to trametinib, a MEK inhibitor[109], with a normalized viability of 55%. This sample is not broadly susceptible to all treatments though, as it appears among the most resistant samples to pazopanib, palbociclib, rapamycin, and everolimus. A similar observation can be made for the top responder to palbociclib, SARC0086_3. Organoids derived from this PEComa sample showed superior sensitivity to palbociclib, despite showing moderate responses against trametinib, panobinostat, and gemcitabine/docetaxel and strong resistance to pazopanib and combination therapy sorafenib and everolimus. The uniqueness of the samples with the greatest sensitivity to each drug as well as the varied behavior in response to alternative treatments gives us confidence that the tumor organoids are recapitulating patient- and tumor-specific features that may dictate clinical response to therapy.

Another apparent trend is the tendency of samples derived from similar histologic subtypes to cluster together. For example, pazopanib is most effective against osteosarcoma samples with 6 of the top 8 responders originating from osteosarcoma lesions. However, our platform allows us to look beyond subtype with a closer lens to the individual samples, where we see significant heterogeneity in the response of other osteosarcomas such as SARC0069_2 and SARC0036 that appear amongst the most resistant samples. Similarly, we observe 5 epithelioid sarcoma samples group among the responsive samples to palbociclib; however, we see organoids derived from SARC0128, another epithelioid sarcoma, show resistance to treatment. Organoid response to panobinostat is yet another example in which most osteosarcoma samples tend to be more responsive and chordoma samples tend to be more resistant. However, across all of these trends, we identify specific samples that do not follow the behavior of the subtype as a whole. The power to identify these individuals is the goal of comparing organoid response across all sarcoma subtypes.

While collecting data on the unique organoid response to single agent treatments is useful, we can also screen combination therapies that are used clinically as a combinational regimen. As in the drug screening results for single agents, we identified samples that were uniquely sensitive to combination therapies such as the CIC-rearranged tumor, SARC0095, to gemcitabine and docetaxel and osteosarcoma organoids derived from SARC0028_O to sorafenib and everolimus. We found that samples SARC0085_6 and SARC0085_7 that were collected from different anatomical regions of the patient during the same procedure had highly similar response to gemcitabine and docetaxel. Though these separate lesions showed similar response, this is not always the case. Organoids derived from multiple lesions (SARC0075_1, 2, and 4) show polarized responses to sorafenib and everolimus with SARC0075_1 showing excellent sensitivity and the remaining samples having average response to treatment (**Figure 3.3**). Though anecdotal, this evidence suggests that tumor organoids derived from different lesions of the same patient may be able to capture the spatial and temporal heterogeneity in a patient's disease.

To validate our results from single concentration screenings, we screened multiple concentrations of each drug when possible. The standard doses for our experiments were 0.1, 1, and 10 μM with drugs such as cisplatin and carboplatin screened at 25, 50, and 100 μM due to their reduced potency in our organoid models. Tumor specific behavior becomes apparent when plotting dose-response curves of organoids derived from similar tumors of origin (**Figure 3.3B**). Organoids derived from osteosarcoma specimens SARC0103 and SARC0135_2 showed greater sensitivity to receptor tyrosine kinase (RTK) inhibitor, pazopanib, across all tested treatment doses. We observed a similar trend in rhabdomyosarcoma organoids with SARC0133 showing greater sensitivity to treatment across all tested concentrations. We observed less variability in the response of organoids derived from resected primary osteosarcoma tumors as the dose-response curves show a greater degree of overlap. Despite the overlap, we see distinct

separation of SARC0131 and SARC0135_2 from the other samples with viabilities of 57.5% and 50.9% at 1 µM, respectively.

Sarcoma PDTOs demonstrate subtype-specific responses to treatment.

Though we observed enormous heterogeneity in the response of organoids to treatment when comparing to other individual samples across subtypes, we also observed disease-subtype specific trends in response to some therapies. We ranked each sample by its relative viability and compared the mean rank of samples of each diagnosis against all other samples to further investigate this phenomenon (**Figure 3.3C**). For ceralasertib, topotecan, cabozantanib, and everolimus, we found osteosarcoma organoids to be significantly more sensitive than the other pan-sarcoma samples (p-values of 0.0021, 0.028, 0.027, and 0.0085, Wilcoxon Rank Sum Test). In accordance with their well-documented resistance to treatment[110,111], chordomas were significantly less sensitive than the pan-sarcoma population to everolimus (p = 0.015). However, we identified two drugs for which chordoma organoids showed greater sensitivity than the broader population: ribosomal S6 kinase (RSK) inhibitor, BI-D1870 (p = 0.027), and AMP-activated protein kinase (AMPK) activator, A-769662 (p = 0.0021). Despite relatively small sample sizes, we also identified increased sensitivity of epithelioid sarcoma organoids to palbociclib (p = 0.033), chondrosarcoma organoids to FAK/Pyk2 inhibitor, TAE226 (p = 0.043), and PDK1 inhibitor, BX-912 (p = 0.038), rhabdomyosarcoma organoids to pazopanib (p = 0.049) and trametinib (p = 0.014), leiomyosarcoma organoids to dovitinib (p = 0.0099), and UPS organoids to IGF-1R inhibitor, BMS-754807 (p = 0.044). Notably, we also found leiomyosarcoma organoids to be more resistant to topotecan than the pan-sarcoma population (p = 0.031) (**Figure 3.3C**).
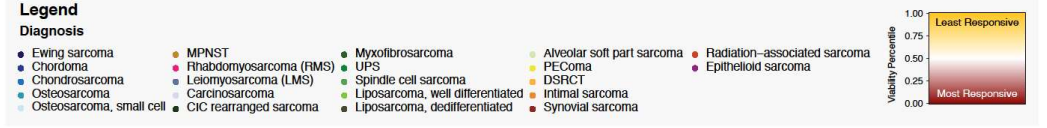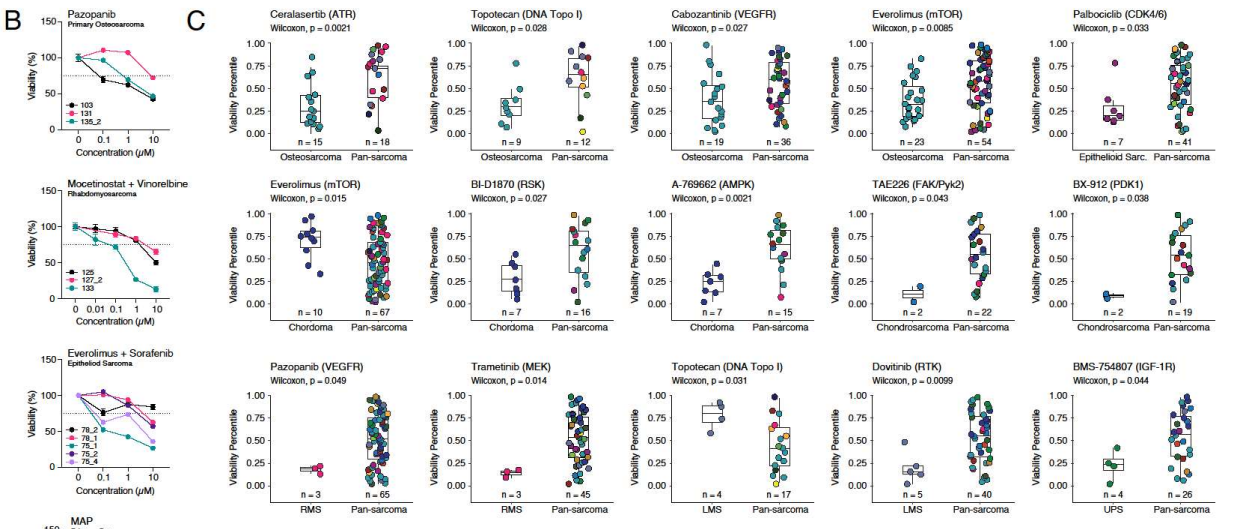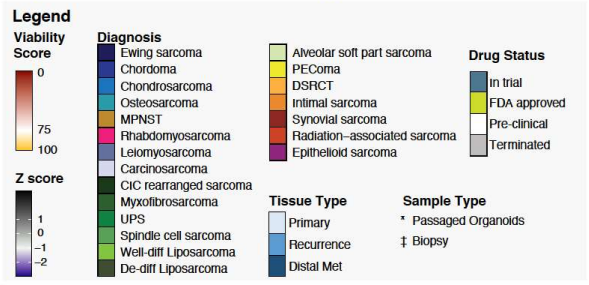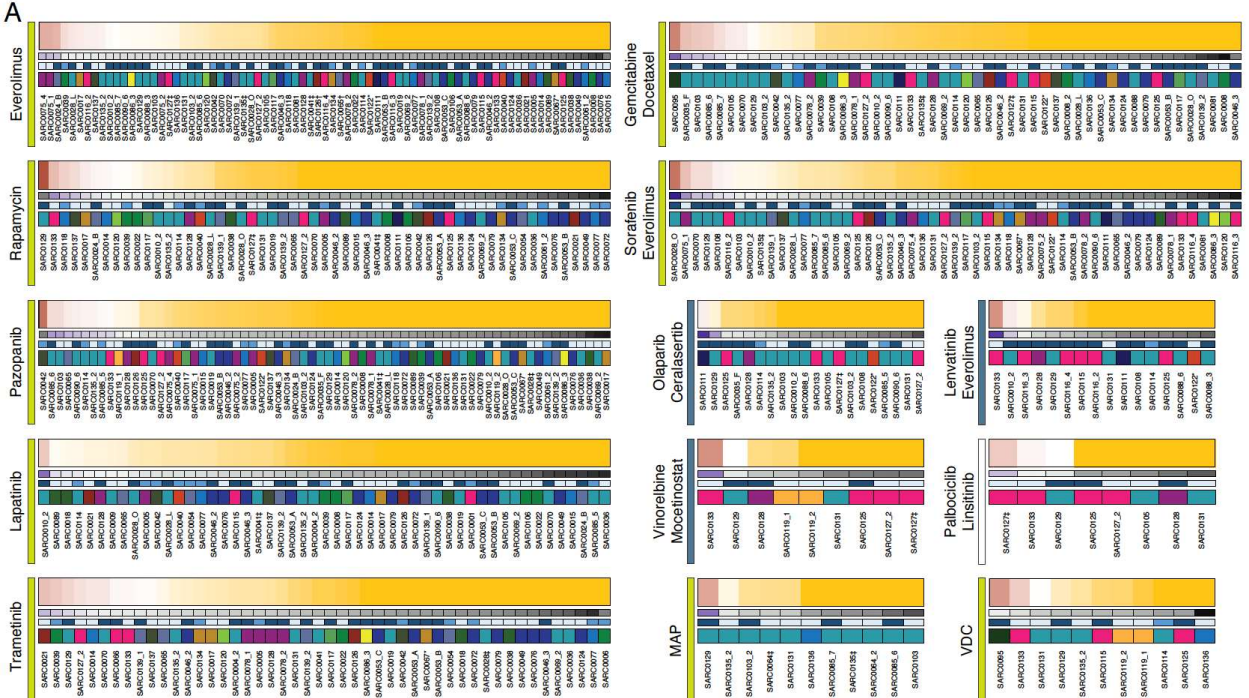
Figure 3.3: Sarcoma organoid sensitivity to treatment in high-throughput drug screening experiments shows a range of responses. (A) Heatmaps of organoid sensitivity to selected drugs of interest at 1 μM. The viability score represents each organoid model's viability normalized to the mean response to treatment across all samples. Each column is a unique specimen, red indicates higher sensitivity to treatment than average. Colored bars underneath each heatmap represent the Z-score, lesion type, and diagnosis of each sample. **(B)** Dose-response curves of organoid viability when treated with selected therapeutic regimens. Percent viability is reported compared to vehicle-treated organoids for each individual sample. **(C)** Sensitivity rank plots comparing the response of organoids derived from the indicated diagnoses (left) against pan-sarcoma specimens (right). Samples are ranked from low residual viability percentile (most responsive samples) to highest residual viability percentile (least responsive samples). Primary drug targets are indicated next to each drug's name. The color of each point represents the diagnosis of the individual samples.

Clinical features associated with drug responses.

We integrated our drug screening results with the clinical features of each tumor and compared organoid sensitivity against factors such as patient age at diagnosis, lesion type, treatment history, and disease progression (**Figure 3.4**). We found patient age to be significantly related to organoid response to treatment for n = 19 drugs. Sarcoma organoids derived from adult patients showed greater resistance to cediranib, everolimus, and masitinib, whereas ruxolitinib and panobinostat appear to be most effective on organoids derived from adolescent and young adults (AYA) patients. One important consideration is that the differences in response between age groups may be driven by the prevalence of a histological subtype. In the case of cediranib, 8 of 13 samples in the pediatric and AYA populations were osteosarcomas whereas there were no cases of osteosarcoma among adult patients in our analysis. Samples treated with everolimus had a similar pattern in which rhabdomyosarcomas and osteosarcomas made up 12 of 13 pediatric cases, 19 of 35 AYA cases, and 0 of 29 adult cases. When looking at the lesion type of the parent tumor, sarcoma organoids that were sourced from metastatic lesions showed a greater response to cediranib than organoids from primary or recurrent tumors (p = 0.025 and p = 0.019,

26

respectively). We observed the same pattern for the deubiquitinase (DUB) inhibitor, degrasyn, in which all five metastatic samples screened ranked in the lower 25th percentile of organoid viability. For the IGF-1R inhibitor, GSK1904529A, we observed a unique trend in that organoids derived from recurrent tumors showed greater sensitivity than those from primary samples (p = 0.028) (**Figure 3.4**).

We also investigated the effects of each specimen's prior treatment history on organoid response. Of the 501 total monotherapies screened, 23 drugs yielded statistically significant reductions in organoid viability for tumors that had been exposed to prior systemic therapies of any kind compared to tumors that were not treated systemically. Crizotinib, dasatinib, everolimus, lenvatinib, and pazopanib (p = 0.013, 0.034, 0.017, 0.013, 0.025, respectively) were all more effective on organoids derived from tumors that were pre-treated systemically compared against systemic-treatment naïve samples. We further tested the relationship between the number of prior systemic therapies and the organoid response to treatment (**Figure 3.4**). A total of 16 treatments yielded significant differences between the number of prior systemic treatments, categorized as zero, one or two, and three or more treatment lines. We observed in the case of pazopanib and danusertib that organoids derived from patients exposed to three or more lines of systemic therapy were more sensitive than systemic-treatment naïve tumors (p = 0.0054, and 0.011, respectively). Linsitinib, and lenvatinib demonstrated significant reduction in viability in samples that were treated with one or two lines of systemic therapy compared with samples that were never treated systemically (p = 0.031, 0.029, respectively). In the case of these drugs, we observed no statistically significant differences in organoid viability between samples that were treated with three or more lines of therapy and samples with a history of just one or two lines of treatment (**Figure 3.4**). Beyond systemic treatment, we investigated the correlation between organoid viability and prior exposure to radiotherapy. Similar to our other findings regarding systemic treatment history, we identified 16 drugs that were more effective against organoids from

previously radiated tumors out of a total of 17 that were deemed significant. Fimepinostat, nilotinib, and vinorelbine (p = 0.036, 0.035, and 0.012, respectively) all led to statistically significant reductions in viability among organoids from patients clinically treated with radiation. AZ 960, a JAK2 inhibitor, was the only drug to yield the opposite relationship in which radiation-naïve samples were significantly more sensitive to therapy (p = 0.012) (**Figure 3.4**).

Lastly, we compared organoid viability with respect to changes in a patient's disease status at time of follow-up. A change in status was characterized as either tumor recurrence following resection or the identification of metastatic lesions from previously primary or localized recurrent tumors. A total of 24 drugs showed significant differences in organoid response across change in status. Organoids derived from patients who later developed progressive disease were significantly more resistant to treatment with dasatinib (p = 0.016), rapamycin (p = 0.01), trametinib (p = 0.028), and vistusertib (p = 0.034). The one exception to this trend was the lignin, honokiol. Organoids derived from patients with progressive disease tended to be more responsive to treatment (p = 0.033) (**Figure 3.4**). Additional drugs we screened and were associated with significant differences between organoid viability and the clinical attributes discussed above can be found in **Figure S3.4-S3.9**.

Figure 3.4: Organoid sensitivity correlates with clinical attributes. Sensitivity rank plots comparing the sensitivity of organoids derived from specimens with varying clinical features including patient age at diagnosis, lesion type, number of prior systemic therapies, prior systemic or radiotherapy, and change in disease status. All samples screened with a drug are ranked from lowest viability (low viability percentile) to highest viability (high viability percentile) and plotted according to the rank. Primary drug targets are shown next to each drug name. The color of each point represents the diagnosis of the individual samples screened with the drug of interest. Statistical significance is tested by performing a Kruskal-Wallis test with post-hoc Wilcoxon Rank Sum Test for pairwise comparisons with Bonferroni correction for comparisons across three classifications. For comparisons across two categories, a Wilcoxon Rank Sum Test was performed.

Target analysis of drug responses highlights vulnerable biological pathways in sarcoma.

Using the drug sensitivity profile of each sample, we identified the molecular pathways that contributed the most to organoid sensitivity (**Figure 3.5**). We first mapped each drug we screened to their gene targets and genetic pathways from the WikiPathways database[103]. We then calculated a score for all pathways to quantify the extent to which drugs targeting the pathway led to reductions in organoid viability. We then ranked each scored pathway for each sample from most impactful (**Figure 3.5, red**) to least impactful (**Figure 3.5, blue**) and clustered the pathways and samples by their similarity.

We first observed that samples derived from the same patient tended to cluster together. Multiple samples from SARC0103, SARC0078, SARC0075, SARC0139, and SARC0053 clustered tightly suggesting that tumors of the same origin tend to show similarities even if the tissue was collected over different anatomical regions or surgical procedures. Beyond the similarities identified in samples from the same patient, we also found groups of samples that shared vulnerable pathways. We found a cluster of 21 samples with significant sensitivity in the proteasome degradation and parkin-ubiquitin proteasomal system pathways, primarily due to their

strong response to the proteasome inhibitors, bortezomib and carfilzomib. This same group of samples showed sensitivity to a lesser extent in pathways associated with the suppression of HMGB1-mediated inflammation, canonical NF-κβ, and altered glycosylation of MUC1. Interestingly, the samples of this cluster were not derived from a single histological subtype and included 12 osteosarcoma, 3 epithelioid sarcoma, 2 rhabdomyosarcoma, 1 synovial sarcoma, 1 spindle cell sarcoma, 1 MPNST, and 1 dedifferentiated liposarcoma. Another group of mixed histological subtypes had increased sensitivity to oxylipin metabolism pathways with some samples also showing susceptibility in insulin signaling pathways. Organoids derived from a chordoma patient (SARC0053) clustered with another chordoma patient (SARC0049) due to strong sensitivity to treatments targeting genes in the serotonin receptor 2 and STAT3 signaling pathways as well as genes associated with TCA cycle nutrient use. We observed that these same pathways are vulnerable for a second group of samples encompassing subtypes of both bone and soft tissue sarcomas (SARC0038 to SARC0024_B, **Figure 3.5**). Another group of samples comprised of chordoma, DSRCT, leiomyosarcoma showed increased susceptibility in blood vessel-related pathways such as angiogenesis and Robo4 and VEGF signaling (SARC0119_2 to SARC0046_3, **Figure 3.5**). We identified five samples (SARC0018, myxofibrosarcoma; SARC0114, osteosarcoma; SARC0022, UPS; SARC0111, Ewing sarcoma; SARC0035_F, osteosarcoma) that showed elevated response to drugs targeting pathways associated with neural crest differentiation, histone modification, and SKIL protein partners. Another group of specimens composed of osteosarcoma, UPS, Ewing sarcoma, rhabdomyosarcoma, chondrosarcoma, leiomyosarcoma, and radiation-associate sarcoma (SARC0114 to SARC0139_1, **Figure 3.5**) demonstrated vulnerability in pathways associated with dietary restriction and aging and histone acetylation. A subset of these samples (SARC0115 to SARC0139_1, **Figure 3.5**) also showed sensitivity to drugs targeting inflammation-related pathways. These inflammation pathways were ranked high across a broader set of 17 samples

originated from a variety of histological subtypes. Overall, the pathway analysis shows that organoids capture features unique to each individual tumor and suggests that the response of each tumor transcends the histological subtype that currently dictates its treatment.

Figure 3.5: Drug screening reveals vulnerable molecular pathways. Heatmap showing the molecular pathways most sensitive to drug targeting for each screened sample. Similar pathways are clustered together using the Jaccard distance and samples are clustered together by their Euclidian distance. Pathways are ranked independently for each sample based upon the results of drug screening experiments. Pathways targeted by the most effective drugs are ranked highest (red). Opaque squares indicate pathways in which more than 50% of the constituent genes were targeted in the drug panel. Only pathways ranked in the top 50 for 20 or more samples are plotted. White squares indicate that the pathway was not targeted by any drugs in the screening experiments.

Clinical availability of organoid-indicated drugs: a roadmap to actionability.

We considered the normalized viability of the sarcoma organoids across all subtypes to generate a list of the most effective drugs for each sample. For the drugs that were ranked as most effective and as organoid-indicated treatments, we annotated the FDA status, and their guideline for use in each sarcoma subtype from the NCCN[1,2] guidelines, if listed (**Figure 3.6**). For more details on how we ranked the drugs please refer to the methods.

Our analysis shows that only 38.3% of organoid-indicated treatments are FDA-approved (**Figure 3.6B**). Moreover, a miniscule 4.5% of these drugs are currently FDA-approved for the histological subtype identified as sensitive in organoid drug screens. Beyond drugs with existing FDA approval, just under one-third of the organoid-identified drugs are currently in clinical trials. Given the rarity of sarcomas as a whole and the scarcity of specific subtypes, only 0.8% of the drugs are in trial for the organoid-directed indication while 24.1% are in trial for other indications. Finally, 36.8% of the drug screening-identified compounds are unavailable clinically as they are in pre-clinical development or have been terminated, suggesting that full implementation of precision medicine practices in the clinic may require giving physicians greater access to investigational compounds through mechanisms such as n=1 clinical trials.

We also investigated the current clinical use of the compounds for each histologic subtype by referencing the NCCN Guidelines for patients with bone[1] and soft tissue[2] sarcoma. The

34

inclusion of a therapeutic regimen in these broadly used clinical guidelines requires substantial evidence that the drug is both safe and effective for each sarcoma subtype. Due to the limitations on clinical trials imposed by small patient populations and highly heterogeneous disease, the vast majority (93%) of promising drugs as identified through our drug screening experiments are not incorporated in the current guidelines. Only 3% of the organoid-indicated drugs are listed as preferred regimens by the NCCN for their corresponding histological subtype. These include etoposide, cisplatin, sorafenib, and regorafenib for osteosarcoma, cyclophosphamide for rhabdomyosarcoma, and doxorubicin for osteosarcoma and Ewing sarcoma (**Figure 3.6A**). An additional 4% of drugs are considered recommended for their respective diagnosis including cabozantinib, gemcitabine, docetaxel, and everolimus for osteosarcoma, doxorubicin and vinorelbine for rhabdomyosarcoma. The remaining 93% of drugs are beyond the recommendations of the NCCN Guidelines further supporting the notion that the implementation of functional precision medicine may require moving beyond the current clinical standards for drug selection in order to match each patient to the optimal therapeutic regimens.

We then focused on investigating the efficacy of clinically utilized regimens in the NCCN[1] guidelines on osteosarcoma organoids (**Figure 3.6C, Figure S3.10, Table 3.1**). We categorized the drugs as listed in the guidelines to first and second line, and preferred, recommended, and useful in certain circumstances regimens. The first line combination regimen of methotrexate, doxorubicin, and cisplatin, known as MAP, was not among the most effective organoid treatments in any of the osteosarcoma samples. Among the second line preferred regimens, combination of gemcitabine and docetaxel exhibited the most effective response across about 15% (3/20) of the osteosarcoma organoids. Various second line treatments showed limited effective responses among the osteosarcoma samples, this includes etoposide (1/18), regorafenib (1/26), cabozantinib (1/23), docetaxel (1/21), methotrexate (1/15), gemcitabine (1/21), and everolimus (1/28). We also found that some regimens exhibited no effective response in any of the

osteosarcoma organoids, such as the combination regimens, cisplatin and doxorubicin, cyclophosphamide and topotecan or etoposide. Similar analysis for drugs that are not currently FDA approved and for the combinational regimens we screened can be found in **Figure S3.11**.
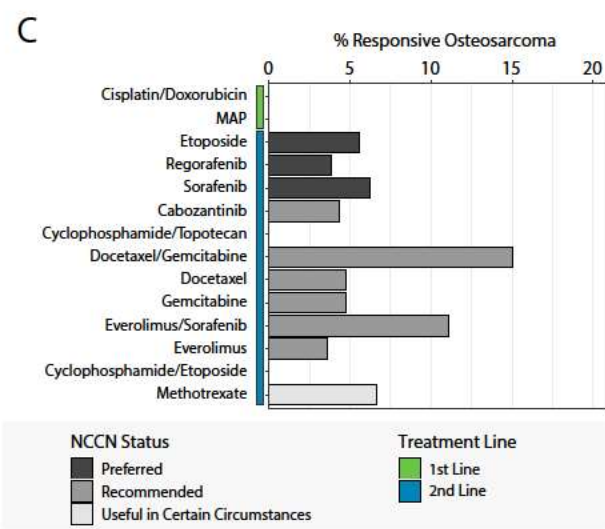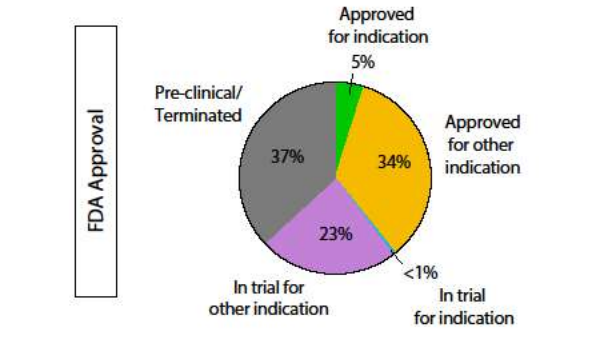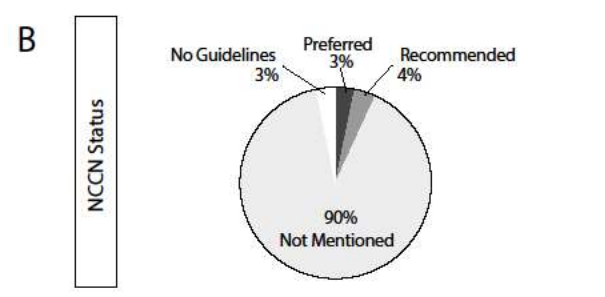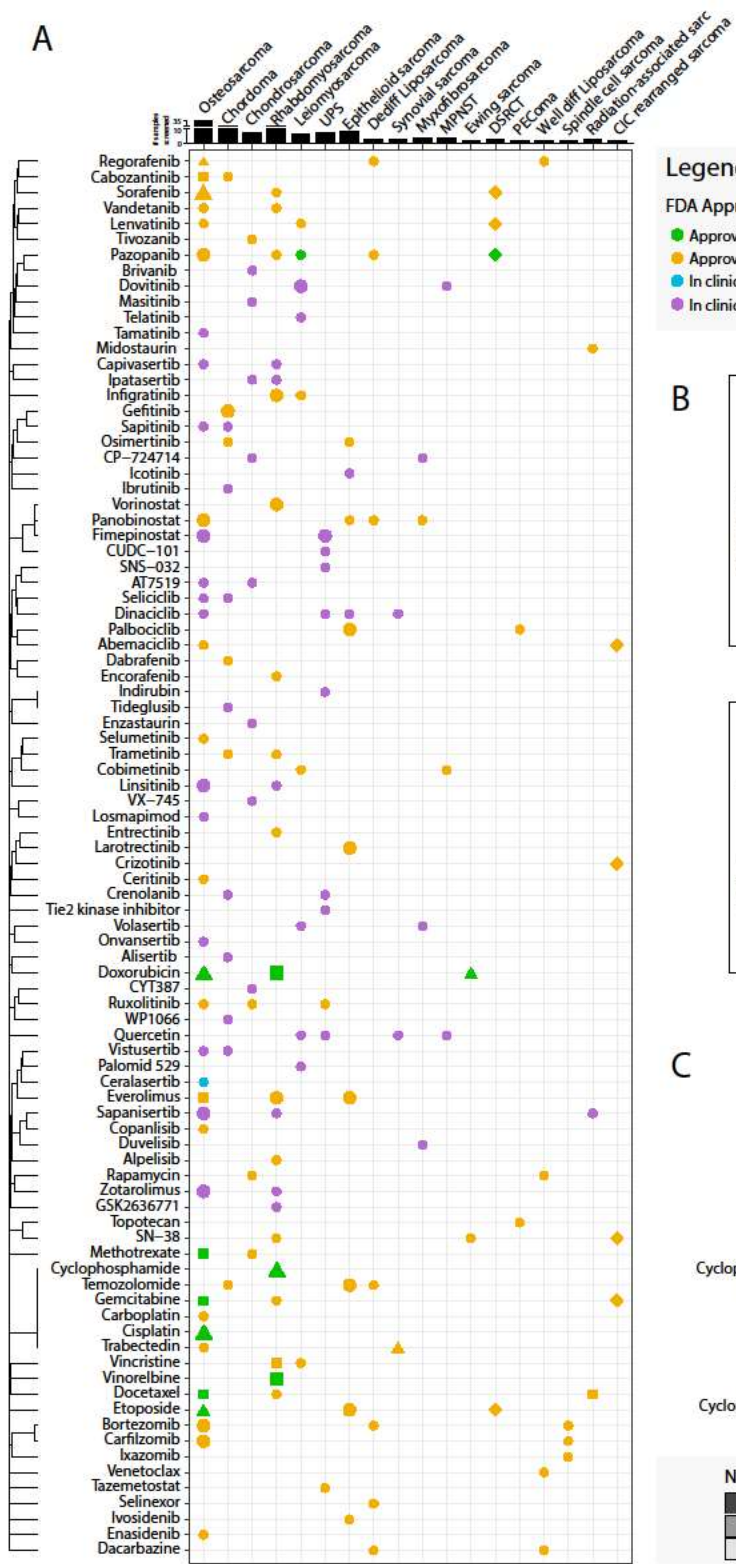
Figure 3.6: Drug availability and NCCN Guidelines status by histological subtype. We selected drug-diagnosis pairs of interest by cross-referencing the five most effective drugs for each sample with the 25% most responsive samples for each drug. **(A)** The current FDA approval status and NCCN Guidelines recommendation are shown for each unique drug-diagnosis combination. Green points mark drugs that are indicated for treating a specific histological subtype by the FDA. Yellow marks drugs approved for other indications including sarcoma and other cancer types. Blue marks indicate drugs currently in trial for the specified indication. Purple marks show drugs in trial for other indications. The shape of the point indicates the current NCCN Guidelines for each drug. Triangles indicate drugs that are indicated as a preferred regimen. Squares signify drugs that are recommended for the subtype of interest and circles indicate that the drug is not currently discussed in the NCCN guidelines[1,2]. Diamond shape signifies that the histologic subtype has no guidelines, such as DSRCT and CIC rearranged sarcoma. The size of the marker indicates whether a single sample or multiple samples of a given histologic subtype was found to be among the five most effective for a drug. Drugs are clustered by similarity in gene targets using Jaccard distance. The number of samples screened for each histologic subtype is shown above. **(B)** Pie charts on the bottom summarize the overall percentage of drugs that fall into each category for FDA approval and NCCN recommendation. **(C)** Percentage of responsive osteosarcoma organoids to NCCN recommended treatment regimens.

Functional screenings provide orthogonal and complementary information to genomic sequencing.

On several occasions, the organoid screening results led to rapid identification of targetable genomic mutations. We collected resected tumor tissue from a patient with metastatic spindle cell sarcoma and performed drug screening on the organoids (SARC0117) (**Figure 3.7**). Within one week of surgery, we identified that the sample was highly sensitive to alpelisib, a PI3K inhibitor. Upon follow up months later, we found that the tumor had been sequenced with a targeted panel (Tempus) and an H1074L mutation was found in PIK3CA. This mutation has been frequently associated with sensitivity to alpelisib in the literature[112–114]. We validated this finding by performing targeted sequencing on the sample we procured and found that it too harbored the PIK3CA mutation. Another patient in our study diagnosed with an MPNST was also found to harbor the same PIK3CA mutation (SARC0134) based on clinical molecular testing of the

resected primary tumor. When we procured tissue from a recurrent lesion of the same patient, we screened the organoids for sensitivity to alpelisib. We found the organoids to be insensitive to alpelisib and hypothesized that the original PIK3CA mutation was not present in the recurrent lesion. We confirmed our suspicions by performing targeted sequencing on tissue from the recurrent lesion and did not find any aberrations in PIK3CA. While the functional screening results do align with genomic characteristics in some cases, this is not universally true. We performed targeted sequencing on SARC0069_2, the most sensitive sample to alpelisib, and did not find mutations in the PIK3CA gene (**Figure 3.7**). These cases emphasize the potential for functional organoid screening to rapidly provide information regarding drug sensitivity that cannot be predicted by current genomic biomarkers alone.

An additional benefit of functional screening is the ability to screen different drugs with similar targets. We screened eight drugs targeting the mTOR/AKT/PI3K pathway on SARC0117, a sample harboring a PI3K mutation (**Figure 3.7**). SARC0117 ranked among the top three most sensitive samples to apitolisib, alpelisib, copanlisib, BGT226, and vistusertib demonstrating its strong response across the entire class of mTOR/PI3K inhibitors (**Figure 3.7C, Figure S3.12**). However, we do not always observe this broad response across a drug class. SARC0133 showed the greatest sensitivity to the FGFR targeting drug, infigratinib, relative to 11 other samples screened. Sequencing revealed that SARC0133 harbors an FGFR1 gain on chromosome 8 contributing to its exceptional response to treatment. When we screened another FGFR-targeting agent, dovitinib, on the same sample, we found that the organoids did not show any sensitivity to treatment (**Figure S3.12**). These examples highlight the important ability of functional screening to differentiate effective agents from ineffective drugs within the same class.

Our screening platform can also be leveraged for diagnostic purposes. For instance, we received tumor tissue from a patient with clinical characteristics consistent with infantile fibrosarcoma

(SARC0127). One of the hallmarks of infantile fibrosarcoma is the presence of NTRK fusions[115,116]. We established organoids from tissue obtained from a biopsy of the treatment-naïve tumor and tested it for sensitivity to the FDA-approved NTRK inhibitor, larotrectinib. The results show how SARC0127 was resistant to larotrectinib. Given the clear relationship between NTRK alterations and larotrectinib sensitivity both in vitro and in patients[117], we suspected that the tumor was not an infantile fibrosarcoma. Following further pathology review, the tumor was classified as consistent with high grade sarcoma. Subsequent fluorescence *in situ* hybridization (FISH) results for ETV6 rearrangement returned negative after 5 days. Following the tumor resection 18 days after the biopsy, the pathologist definitively diagnosed the tumor as a high-grade spindle cell/sclerosing rhabdomyosarcoma. Organoids established from the resection (SARC0127_2) showed a similar pattern of drug sensitivity and resistance, including comparable response to Larotrectinib (**Figure 3.7**). We validated the findings by performing FISH for NTRK 1, 2, and 3 fusions and confirmed that no abnormalities were present. Our platform provided diagnostic clues within a week from the biopsy procedure, confirming the ability to rapidly yield information on the characteristics of each tumor.

Regimen	N responsive samples	N samples screened	Responsive Samples (%)	NCCN Status
Cisplatin/Doxorubicin	0	4	0	Preferred
MAP	0	11	0	Preferred
Etoposide	1	18	6	Preferred
Regorafenib	1	26	4	Preferred
Sorafenib	2	32	6	Preferred
Cabozantinib	1	23	4	Recommended
Cyclophosphamide/Topotecan	0	8	0	Recommended
Docetaxel/Gemcitabine	3	20	15	Recommended
Docetaxel	1	21	5	Recommended
Gemcitabine	1	21	5	Recommended
Everolimus/Sorafenib	2	18	11	Recommended
Everolimus	1	28	4	Recommended
Cyclophosphamide/Etoposide	0	1	0	Useful in certain circumstances
Methotrexate	1	15	7	Useful in certain circumstances

Table 3.1: Response of osteosarcoma specimens to NCCN Guideline treatments. The responsive samples meet the following criteria: the regimen was among the top 5 most effective regimens for a given sample and the sample was among the 25% most responsive samples to the listed regimen.

Evidence of correlation between PDTO and patient responses for matched treatment regimens.

Two samples, SARC0064‡ and SARC0135‡, were biopsies collected from treatment naïve patients. Both patients received neo-adjuvant MAP clinically between the time of biopsy and tumor resection. Upon resection, tumor tissue from SARC0064‡ was found to be 95% necrotic while tumor tissue from SARC0135‡ was only 60% necrotic. Though SARC0064‡ was not the most responsive sample screened, its normalized viability of 57% was less than SARC0135‡ (73%) (**Figure 3.7E**). In this instance, the relative sensitivity of the organoids matches the clinical observations of necrosis percentage for these two patients.

The primary goal of developing personalized tumor organoid models is to leverage them to predict response to treatment. We screened four cases (SARC0088, SARC0103_2, SARC0105, SARC0125) in which the organoids were treated with the same regimen the patient received immediately after sample procurement. Though the sample size is limited (n =4) we see a negative trend (95% confidence interval of slope between -0.048 and 0.000, R^2 = 0.902, p = 0.051) between normalized organoid viability and time to next systemic therapy (TTNT), which can be used as a metric for clinical response (**Figure 3.7F**).
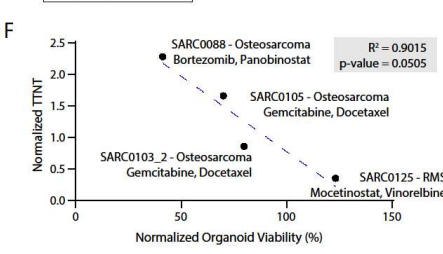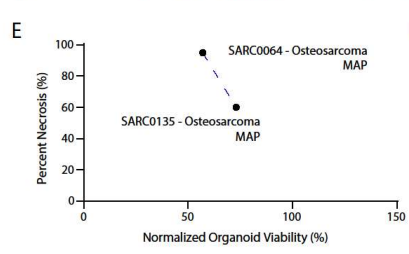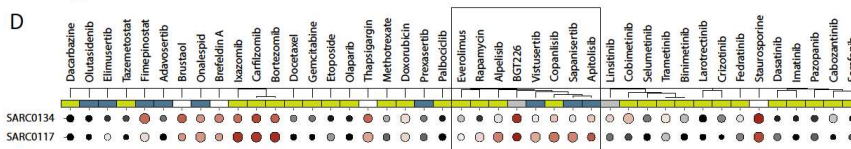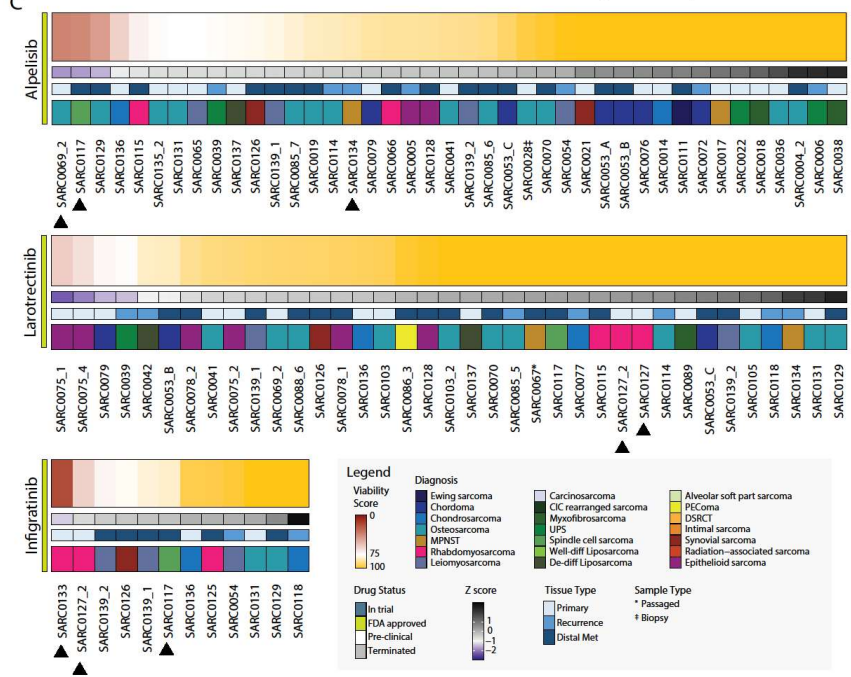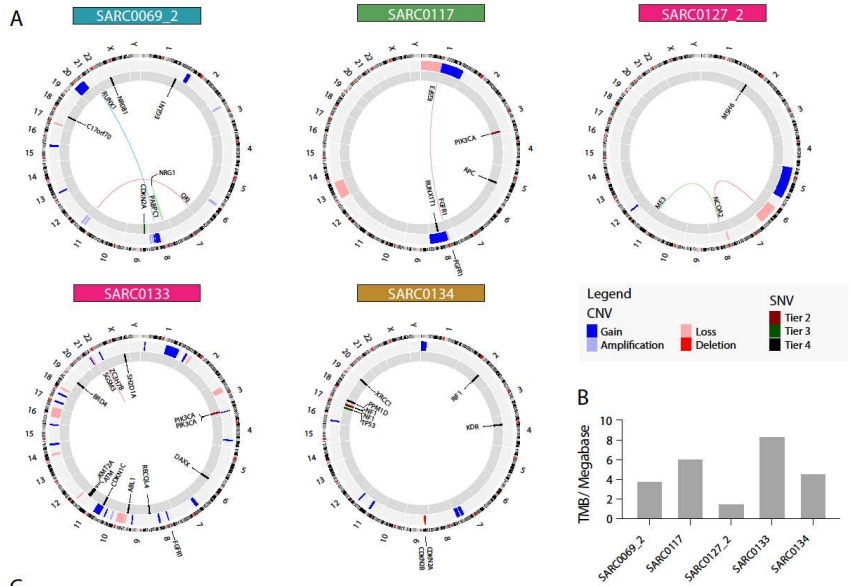
Figure 3.7: Organoids provide genomic and diagnostic information. (A) Summary of the genetic features of selected specimens. Sequencing was performed using OncoPanel and plotting was performed using R. **(B)** Tumor mutational burden (TMB) for selected specimens. **(C)** Organoid viability heatmaps of alpelisib, larotrectinib, and infigratinib. Black arrows indicate samples of interest. **(D)** Comparison of organoid sensitivity profiles for SARC0117 and SARC0134. The black box outlines a region of similar drugs that have variable efficacy across the two samples. **(E)** Correlation between normalized organoid viability and percent necrosis determined by a pathologist following tumor resection for two osteosarcoma biopsies. **(F)** Normalized time to next systemic therapy (TTNT) compared to tumor organoid viability for therapeutic regimens screened on organoids and administered to the patient immediately following sample procurement. TTNT of the matching therapeutic regimen is normalized to the TTNT of the regimen used immediately preceding specimen collection. TTNT greater than 1 indicates that the treatment of interest yielded longer TTNT compared to the previously administered treatment. Sample diagnosis and therapeutic regimen are annotated for each point.

Discussion

We implemented a systems approach to determine the landscape of drug sensitivity and resistance in sarcoma, leveraging tumor organoids derived from tumor biopsies and resections across 25 diagnoses. Our study includes patients across many stages of disease with diverse treatment histories. We demonstrate the feasibility of implementing functional precision medicine at scale by developing systematic protocols for identifying candidate patients, preserving tissue following resection, transporting samples between the procedure and laboratory sites, and generating organoids for high-throughput screening. This process requires support from physicians and nurses interacting with patients, pathologists and core facility staff assessing and providing excess tissue, and researchers carrying out the drug screening protocols. Sarcomas make up less than 1% of cancer diagnoses annually[81], and are notorious for their heterogeneity which makes them difficult to study in timely and well-powered clinical trials[7]. Our work supports the ability to perform these studies in the context of rare cancers.

We generated organoids from 25 distinct histological subtypes of bone and soft tissue sarcoma illustrating that our methodology is agnostic to diagnosis. Organoids generated with our protocol

accurately recapitulate the histological features of the tumor of origin and show unique growth patterns independent of histological subtype. Histological analysis of the organoids shows distinct growth patterns across diagnostic subtypes and between patients within the same subtype. We observed further diversity in brightfield image analysis of sarcoma organoids including differences in organoid morphology, aggregation patterns, and growth dynamics (**Figure 2**). The implementation of a neural network to analyze brightfield imaging data allows us to non-invasively identify unique behaviors of tumor organoids and provides additional value in assessing the response of organoids to treatment. The use of machine learning with organoids facilitates the implementation of new analytical methods such as single organoid tracking to increase the resolution of the functional assay[118].

One of the major challenges associated with performing functional drug screens on patient-derived material is the procurement of representative tumor tissue. Due to the low volume of tissue collected during biopsy procedures, a relatively small amount of tissue remains after the majority is allocated to pathology for standard diagnostic protocols. Because of this, drug screens on biopsied tissue were restricted in the number of drugs and drug concentrations that could be tested despite the feasibility of establishing organoids from biopsy samples. This is unfortunate, as biopsies are the ideal samples for organoid drug screening as they are typically treatment naïve and are most feasible to directly correlate with patient response due to the availability of subsequent imaging and necrotic assessment data. For example, we screened the MAP regimen on organoids derived from two treatment-naïve osteosarcoma biopsies (SARC0064 and SARC0135). Both patients were treated with neo-adjuvant MAP prior to tumor resection. We found that the percentage of necrotic cells in the resected tissue (as assessed by the pathologist) correlated with the biopsy organoid viability. Percent necrosis is an important prognostic factor in osteosarcoma patients with neo-adjuvant treatment[119], and this data suggests organoid drug screening may also be used as a biomarker of response to therapy.

44

The power of sarcoma organoid models that recapitulate the physiology and features of the parent tumor, is demonstrated by the various downstream applications on organoids to gather insightful information on the biology, genomic and molecular profiles, and functional screening profiles on various rare sarcoma subtypes. By applying automated pipelines, we can perform large scale high throughput screening on sarcoma organoids to screen over 500 drugs and build an expanding database of drug sensitivity profiles for rare sarcomas (**Figure 3**). Collecting drug sensitivity data across patients with multiple subtypes of sarcoma allows for the identification of unique patterns of response both within and across subtypes through normalizing drug response across all samples tested. Sarcoma organoids capture the same heterogeneity observed in clinical trials of sarcoma patients[120] (**Figure 3**). The ability to screen many drugs at many stages of development, such as FDA approved, in clinical trials or pre-clinical stages that target different pathways, coupled with the short timeline of our pipeline allows oncologists to obtain actionable information within a week of biopsy or surgery. The quantitative assessments of response within a specific sub-type may be useful in guiding future drug development and clinical trials for these rare tumors (**Figure 3C**). Furthermore, by harnessing the growing database of sensitivity profiles of sarcoma organoids, drugs with different mechanisms of action can be compared to identify the pathways most impacted on an individual sample basis (**Figure 5**). The ability to compare responses to drugs within the same class of targets provides us with an additional tool to overcome the heterogeneity of sarcomas, as we have observed that genomic aberrations or perturbances in certain pathways in a sample can be targeted more effectively by certain drugs in a class. This is highlighted by infigratinib, a selective FGFR1-3 inhibitor[109], and dovitinib, which also targets FGFR[109]. We observed selective organoid response in sample SARC0133 which harbored an FGFR1 amplification to infigratinib (**Figure 7**), but not to dovitinib (**Figure S12**).

By leveraging data from high-throughput sarcoma organoid screening and our expanding sarcoma biobank, we can perform statistical tests to investigate the relation between subtypes

with increased organoid sensitivity to drugs and relevant clinical attributes such as age, lesion type, treatment history, and progression of disease in follow up (**Figure 4**). The identification of clinical attributes associated with significant resistance or sensitivity to certain drugs, can potentially help identify biomarkers in bone and soft tissue sarcomas to treatment response, as sarcomas currently lack reliable biomarkers[121].

The power of any precision medicine method lies within its ability to provide actionable information leading to the selection of the optimal therapeutic regimen for each patient. The major caveat to this approach is that physicians must have access to the drugs recommended by the precision medicine platform. Furthermore, the rarity of cases presents a challenge in conducting clinical trials. One goal of our study is to demonstrate the feasibility of using organoids to provide recommendations for treatment, so we assessed the availability of the drugs indicated by organoid screening. While approximately two-thirds of drugs were currently being tested in clinical trials or already FDA approved, fewer than 5% are currently approved for the histological subtype identified. Furthermore, only 8% of drugs were listed in the NCCN Guidelines as preferred or recommended therapies. Our analysis foreshadows a coming challenge towards adopting functional precision medicine in the clinical setting. For precision medicine to have its maximum impact, barriers to physician selection and administration of treatment must be modified to account for precision medicine assays.

Thus far, we have observed correlations between the genetic features of tumors and the organoid response to treatment. However, the primary goal remains the correlation of organoid response to treatment with long-term patient outcomes. Beyond the scope of a clinical trial with regular follow-up and standardized measurements of progress through imaging and functional assessments, these relationships are difficult to discern. We are currently evaluating patients for which we have screening results for the therapy used immediately after tissue procurement and are collecting information on disease progression and treatment history to assess the utility of the

organoid screening results. Our hypothesis is that organoids sensitive to the administered treatment will lead to longer response durations relative to prior therapies. Given the complex treatment history of many of the patients included in our study, there are significant confounding factors such as prior radiotherapy and the independent response of different metastases that may obscure a potential relationship. As we continue to track the progress of patients throughout the course of their treatment, we gain further evidence to test the relationship between organoid screening results and patient outcomes. In conclusion, the tumor-specific drug sensitivity profiles of the organoids established in our study demonstrate that functional precision medicine approaches can provide clinically relevant data to support the selection of treatment for sarcomas. For patients battling rare tumors, approaches like ours provide new information with the potential to identify effective treatments, avoid ineffective therapies, and improve patient outcomes overall.

Methods

Patient Sample Collection

The protocol for collecting and processing tumor tissue has been previously described[9,18]. In summary, fresh tumor specimens are obtained from consenting patients (UCLA IRB #10-001857, 19-002214). Solid tumors are minced and digested with collagenase IV (200 U/mL) to yield a suspension of single cells/small clusters. The cells are then transferred to a new tube, followed by red blood cell lysis with Ammonium Chloride Solution (Stem Cell Technology). Cells are then strained using a 100µm filter before counting and viability assessment using a Cellometer Auto 2000 (Nexcelom).

Organoid Generation

Primary cells are resuspended in a 3:4 solution of Mammocult medium (Stem Cell Technology) and Matrigel (Corning)[78,95,99]. The mixture is kept on ice throughout the organoid seeding process to prevent premature crosslinking. We seed the organoids for drug screening by

distributing 10µL of solution around the perimeter of the bottom of each well of a 96-well plate. We incubate the material for 30 minutes at 37°C to solidify the gel before adding 100µL of Mammocult medium to each well. Organoids cultured for histological and molecular analyses are seeded in 24-well plates. We seed 100,000 cells in 70µL of the Mammocult-Matrigel solution around the perimeter of each well of a 24-well plate. Each well plate is imaged using a high-content microscope (Celigo, Nexcelom) every 24 hours.

Drug Screening

After allowing the organoids to grow and develop for 3 days, we perform drug treatments using a panel of targeted agents and chemotherapies to assess sensitivity following our published protocols[9,18]. First, we remove the medium from each well using an automated fluid handler (Microlab NIMBUS, Hamilton or epMotion 96, Eppendorf) and replace it with pre-warmed Mammocult containing the desired drug concentration and 1% DMSO. Each plate contains its own positive and negative controls for normalization. The positive control is 10 µM staurosporine and the negative control is 1% DMSO. Organoids are incubated at 37°C and 5% CO_2 throughout drug treatment. After 24 hours, we exchange the medium with fresh, drug-loaded medium. After 2 days of treatment total, organoid viability is assessed with an ATP assay (CellTiter-Glo, Promega). The organoids are released from the matrix with dispase followed by addition of the CellTiter-Glo reagent. After 30 minutes, luminescence is measured using a SpectraMax iD3 plate reader (Molecular Devices).

Database

We maintain a PostgreSQL relational database that stores coded non-identifiable patient and sample information of our biobank. We implemented several external databases to our database such as gene pathway data from WikiPathways[103], and mechanistic targets of our drug library from PubChem[102] and literature (**Figure S3.1**). After organoid plates undergo drug screening, we use a Python-based, custom XML parser to upload the luminescence data to the

database. This data is then connected to a sample collection that contains additional information about the patient and sample procurement using Django, a Python-based web framework. The drug treatment used for each well is also manually uploaded to the database. All downstream analysis is performed using R (v4.2) and begins by querying the database.

Drug Screening Analysis

We screened each drug with either n = 1 or 2 at a concentration of 1 μM, with the exceptions of platinum agents, cisplatin and carboplatin, which we screened at 25 and/or 50 μM.

Plate-level statistics including the Z'-factor[122], and robust Z'-factor[106], are calculated for each plate of organoids and are used as inclusion metrics for subsequent analysis. The thresholds for inclusion in this study are the following: Z'-factor > 0.2 or robust Z'-factor > 0.2. These criteria were selected to exclude plates that have an insufficient statistical effect size which are prone to false positives and negatives in high-throughput assays. We used the luminescence values of staurosporine screened at 10 μM as a positive control and substituted with 1 μM when not available. For plates that were screened with only one well of staurosporine 1 μM, the values were pooled across the plates as a positive control for the experiment.

For plates that were included in the analysis, the luminescence measurements from the ATP assay are normalized to the mean luminescence of the negative control (1% DMSO) wells to calculate percent viability. For each drug treatment, the viability of each sample is normalized to the mean response of all samples treated with the drug of interest. Response rank percentile is calculated by dividing the rank of each sample and dividing it by the total number of samples screened with each drug.

Histopathology

Histopathology analysis is performed on the tissue of origin and the organoids derived from the collected specimens. Sections of the tissue of origin are obtained through the

49

Translational Pathology Core Laboratory (TPCL) at UCLA. The sections received are 5µm slices of formalin-fixed, paraffin-embedded (FFPE) tissue mounted on glass slides.

Organoids are prepared for histopathology after 5 days of culture. Each well is washed with 1 mL of phosphate buffered saline (PBS) prior to fixation with 500 µL of 10% buffered formalin (VWR, 89379-094). After at least 24 hours of fixation, the organoids are removed from the 24-well plate and transferred to a conical tube. They are washed with PBS prior to the addition of 5 µL of Histogel (Thermo Fisher Scientific, HG-40000-012) to suspend the organoids. The Histogel is then transferred to a cassette and sent to TPCL for paraffin embedding. We section organoid blocks at 8µm and mount them on Superfrost Plus Microscope Slides (12-550-15, Fisher Scientific).

Hematoxylin and eosin staining was performed on the parent tumor and the resulting organoids derived from tissue collection. Our slides were stained by TPCL in accordance with their standard protocol. All images were acquired using the Revolve Upright and Inverted Microscope System (Echo Laboratories).

Growth Quantification with Image Analysis

We image the organoids daily using a high-content microscope that scans two focal planes per well. The resulting whole-well images are exported in TIF format at a resolution of 1 µm/pixel. We then implement our previously developed methodology to segment and quantify regions of the image containing organoids[95]. We use a convolutional neural network with a U-Net architecture[104] to segment the regions of the images containing organoids. This model is based on a ResNet-34 model[123] trained on 223 manually-labelled images spanning an array of tumors of origin to capture the diverse organoid morphologies observed in this study. In the manually-labelled dataset, only in-focus organoids are marked for inclusion in the area calculation; this is done to minimize measuring the same organoid across both focal planes. The original weights were derived from a model pretrained on the ImageNet dataset[124] and the final model was trained

over 80 epochs using a cross-entropy loss function. The trained model was then used to segment each image by splitting the image into 512x512 pixel sections, applying the model to each section, and reassembling the sections to recreate the whole segmented image (16,896x16896 pixels).

We then implement OpenCV to calculate the total area of the organoids in each focal plane. This area is then averaged across both focal planes and growth is measured by normalizing to the area covered by organoids on the first day of imaging of the same well. The resulting data was then plotted using GraphPad Prism as normalized area over time.

Targeted Sequencing

Select samples were sent to the Center for Advanced Molecular Diagnostics (CAMD) at Brigham and Women's Hospital for analysis using the OncoPanel v3[125]. Sequencing was performed on pre-sectioned 10 slides from non-decalcified FFPE tissue blocks. Slides are then shipped to CAMD for sequencing and analysis. We plotted the results in a circos plot using R.

Fluorescence In Situ Hybridization (FISH)

We identified NTRK 1, 2, or 3 fusions by performing Fluorescence In Situ Hybridization (FISH). Pre-sectioned slides from non-decalcified FFPE tissue blocks from select samples were sent to NeoGenomics for performing their NTRK 1, 2, 3 FISH Panel (88374x3).

Pathway Analysis

Protein targets for each drug in our library were annotated and obtained from PubChem[102] and literature. We selected only targets that are within 10-fold of the second-lowest reported value for Kd (dissociation constant) or IC50 (median inhibitory concentration) among the targets. To perform the pathway analysis, we mapped each drug and their protein target with values of 0 and 1, with 1 indicating that a drug targets a protein, and 0 indicating the lack of protein among the drug targets. We filled the values in a matrix composed of n_{drugs} x $m_{protein}$.

51

To adjust for the degree of impact of protein targets on the viability of samples, we multiplied each row in the matrix by a weight proportional to the mean viability of the organoids treated by each drug [1 − (mean viability/100)]. We then multiplied this matrix by a vector of 1s to obtain a row-wise summation of the protein target viability values. To adjust for protein targets that are targeted by multiple drugs in our library compared to targets associated with drugs that are less represented in our panels, we normalized the row vector by dividing each element by the sum of non-zero column entries in the $n_{drugs} \times m_{protein}$ matrix.

We then mapped this list of proteins to the canonical pathways defined by the WikiPathways Database [version 20220710][103]. We excluded pathways that are not biologically pertinent to cancer, such pathways related to microorganisms and pathogens, as well as the newly added coronavirus disease (COVID)–related pathways.

We populated a new matrix comprised of $n_{pathway} \times m_{protein}$, with 1s indicating the presence of a protein in a particular pathway or 0s indicating its absence. We then normalized the rows in the pathway matrix to account for the differences in the number of proteins included in each pathway. To obtain the relative effect that targeting a specific pathway has on the viability of sarcoma organoids, we multiplied the $n_{pathway} \times m_{protein}$ mapping matrix by the normalized $n_{drugs} \times m_{protein}$ vector. The resulting vector represents the relative impact that targeting a given pathway has on the viability of the organoids. We then ranked the scored pathways for each sample to compare the impact of each pathway on a viability of a sample between organoids of different sarcoma subtypes.

Assessment of Drug Availability

Based on our drug screening data, we created a list of the five most effective therapeutic agents for each sample screened. We then created a second list of the top 25% most responsive samples to each drug. We considered only sample-drug pairs that appeared in both lists for further

analysis and mapped each sample to its diagnostic subtype. For each drug-diagnosis pair, we manually annotated the inclusion of each therapy in the NCCN Guidelines[1,2] as well as the current FDA approval status for each drug with respect to the histological subtype.

Supplemental Information
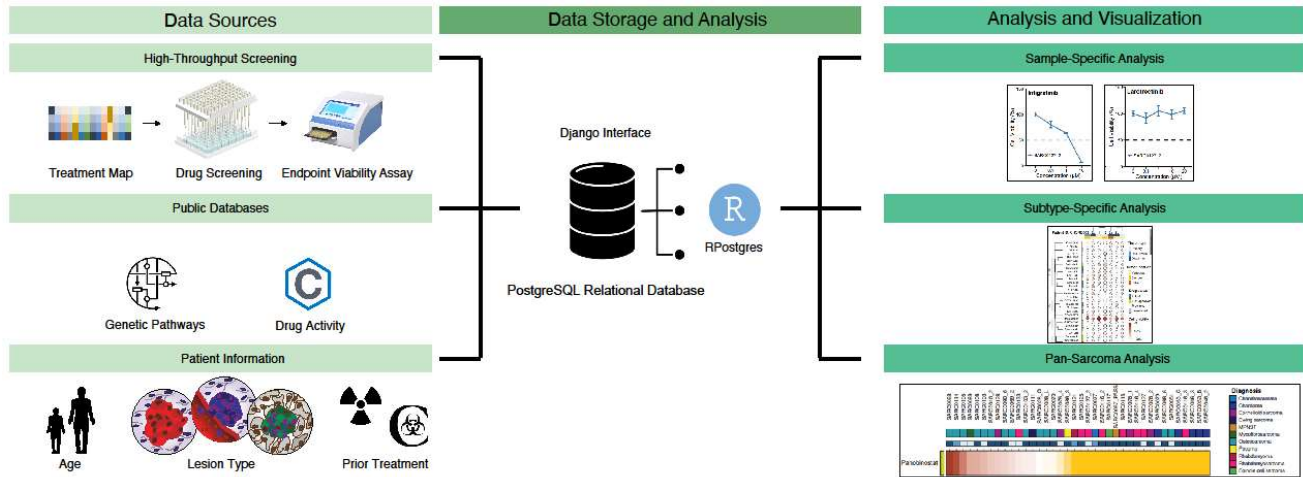
Figure S3.1: Analytical pipeline and sources of data for the relational database used for storing and analyzing drug screening data.
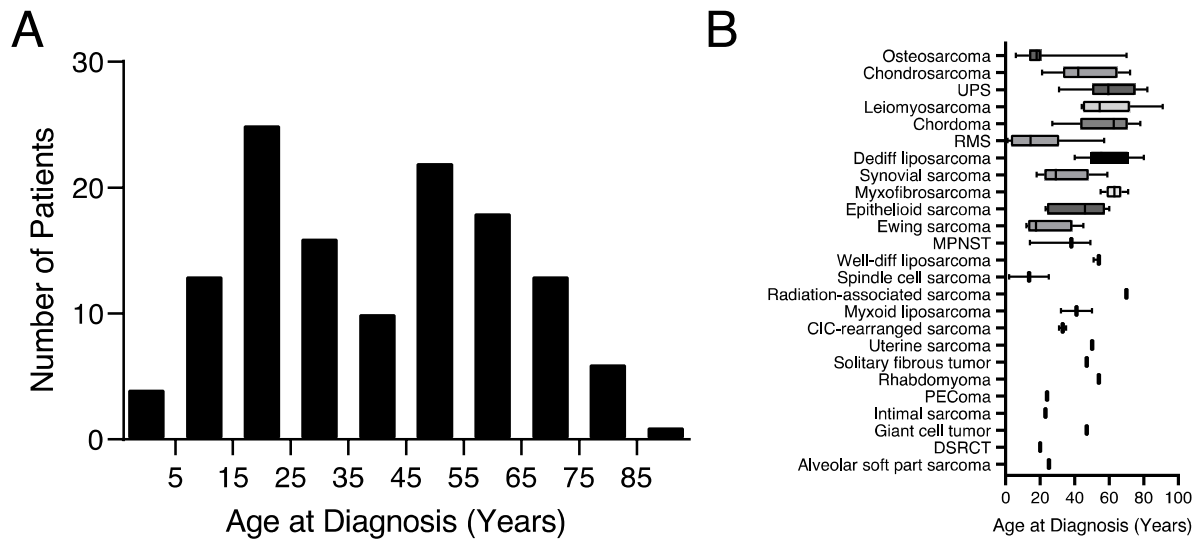
Figure S3.2: Age distribution by subtype.
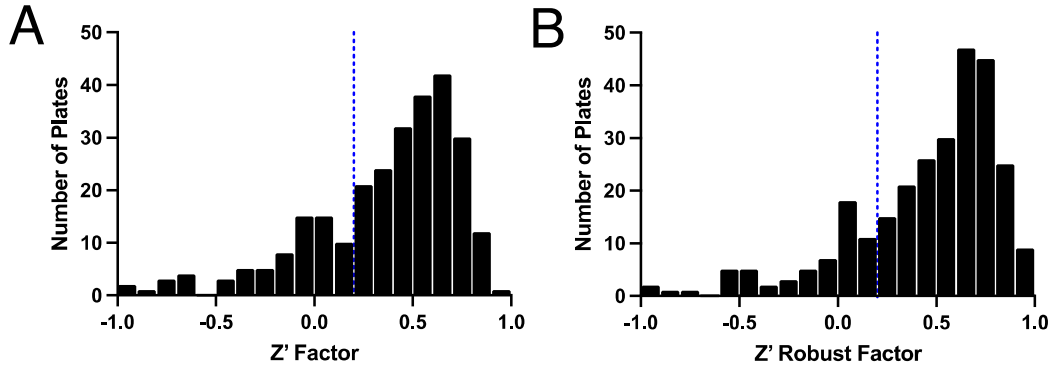
Figure S3.3: Distribution of Z' factor and robust Z' factor of the screened sarcoma plates. Dotted vertical line indicates cutoff of 0.2 for both Z' factor and robust Z' factor.

Figure S3.4: Additional drugs with correlation between organoid sensitivity and patient age at diagnosis. All samples screened with a drug are ranked from lowest viability (low viability percentile) to highest viability (high viability percentile) and plotted according to the rank. The color of each point represents the diagnosis of the individual samples screened with the drug of interest. Statistical significance is tested by performing a Kruskal-Wallis test with post-hoc Wilcoxon Rank Sum Test for pairwise comparisons with Bonferroni correction.

Figure S3.5: Additional drugs with correlation between organoid sensitivity and lesion type. All samples screened with a drug are ranked from lowest viability (low viability percentile) to highest viability (high viability percentile) and plotted according to the rank. The color of each point represents the diagnosis of the individual samples screened with the drug of interest. Statistical significance is tested by performing a Kruskal-Wallis test with post-hoc Wilcoxon Rank Sum Test for pairwise comparisons with Bonferroni correction.

Figure S3.6: Additional drugs associated with correlation between organoid sensitivity and number of prior systemic therapies. All samples screened with a drug are ranked from lowest viability (low viability percentile) to highest viability (high viability percentile) and plotted according to the rank. The color of each point represents the diagnosis of the individual samples screened with the drug of interest. Statistical significance is tested by performing a Kruskal-Wallis test with post-hoc Wilcoxon Rank Sum Test for pairwise comparisons with Bonferroni correction.
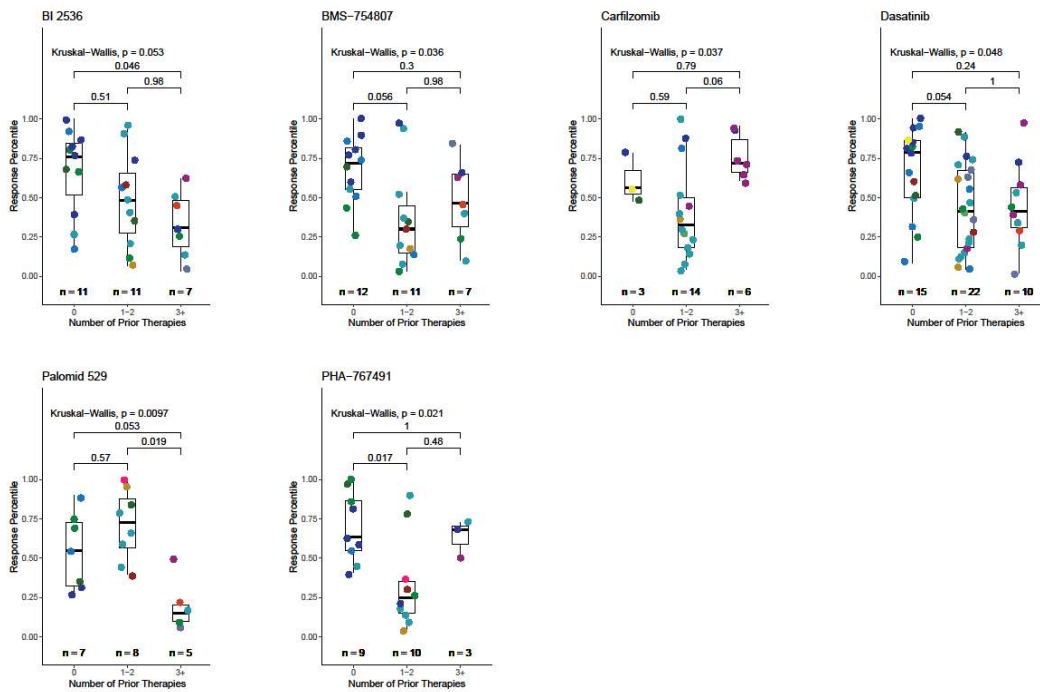
Legend

Diagnosis

- Ewing sarcoma
- Chordoma
- Chondrosarcoma
- Osteosarcoma
- Osteosarcoma, small cell
- MPNST
- Rhabdomyosarcoma (RMS)
- Leiomyosarcoma (LMS)
- Carcinosarcoma
- CIC rearranged sarcoma
- Myxofibrosarcoma
- UPS
- Spindle cell sarcoma
- Liposarcoma, well differentiated
- Liposarcoma, dedifferentiated
- Alveolar soft part sarcoma
- PEComa
- DSRCT
- Intimal sarcoma
- Synovial sarcoma
- Radiation–associated sarcoma
- Epithelioid sarcoma
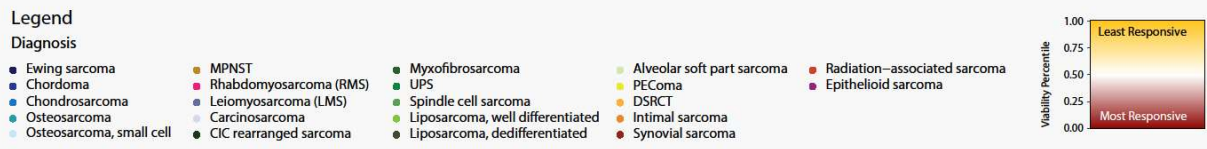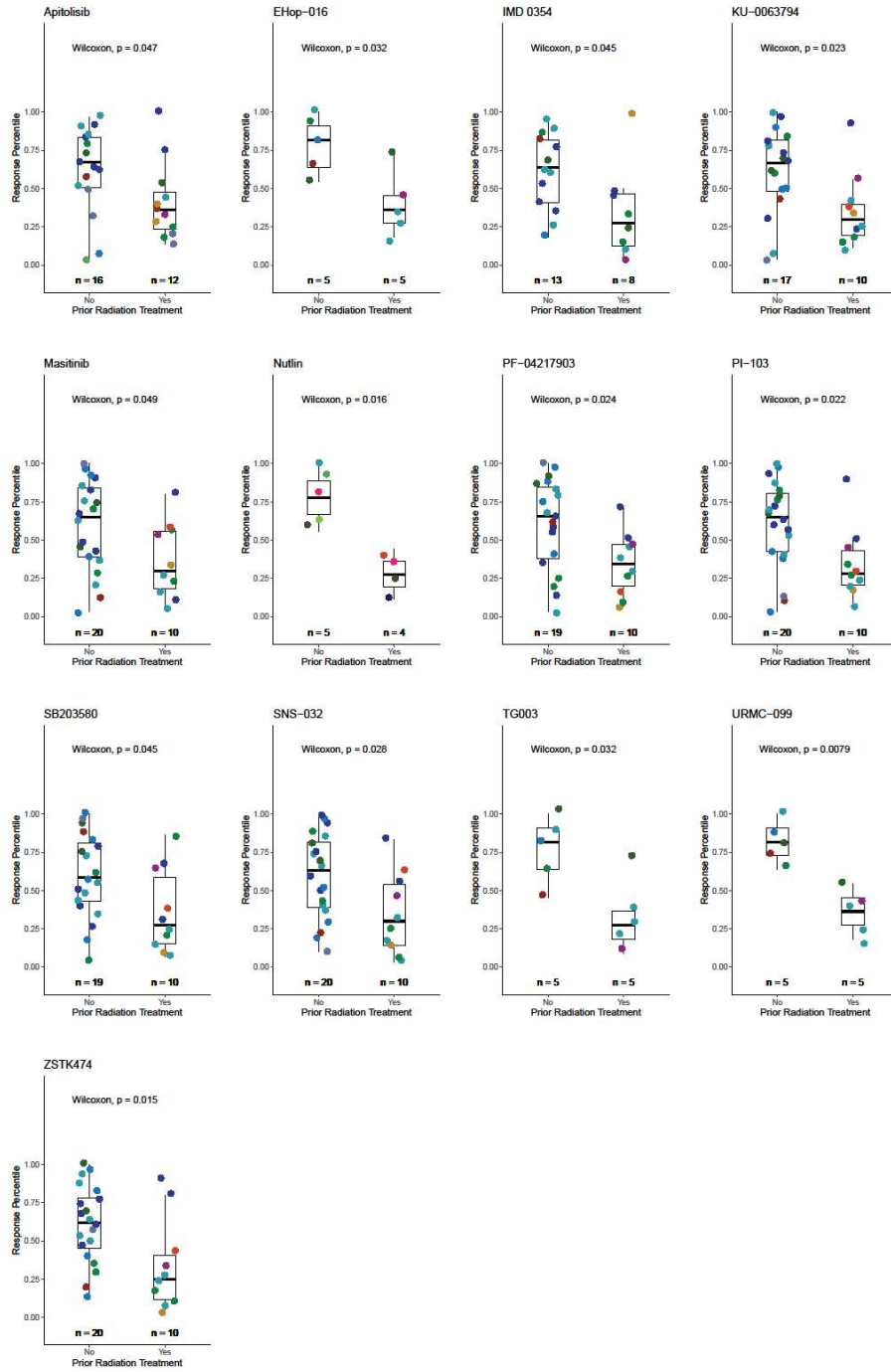
Figure S3.7: Additional drugs with correlation between organoid sensitivity and prior radiation therapy. All samples screened with a drug are ranked from lowest viability (low viability percentile) to highest viability (high viability percentile) and plotted according to the rank. Primary drug targets are shown next to each drug name. The color of each point represents the diagnosis of the individual samples screened with the drug of interest. Statistical significance is tested by performing Wilcoxon Rank Sum Test.

Figure S3.8: Additional drugs with correlation between organoid sensitivity and prior systemic therapy. All samples screened with a drug are ranked from lowest viability (low viability percentile) to highest viability (high viability percentile) and plotted according to the rank. Primary drug targets are shown next to each drug name. The color of each point represents the diagnosis of the individual samples screened with the drug of interest. Statistical significance is tested by performing Wilcoxon Rank Sum Test.
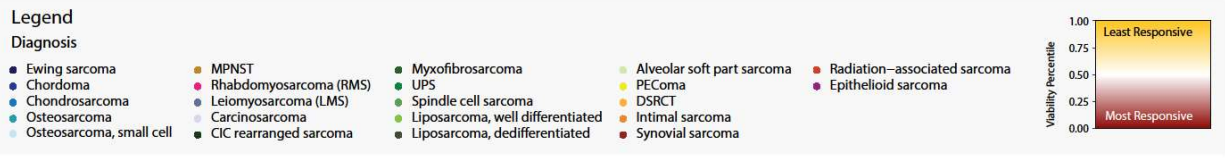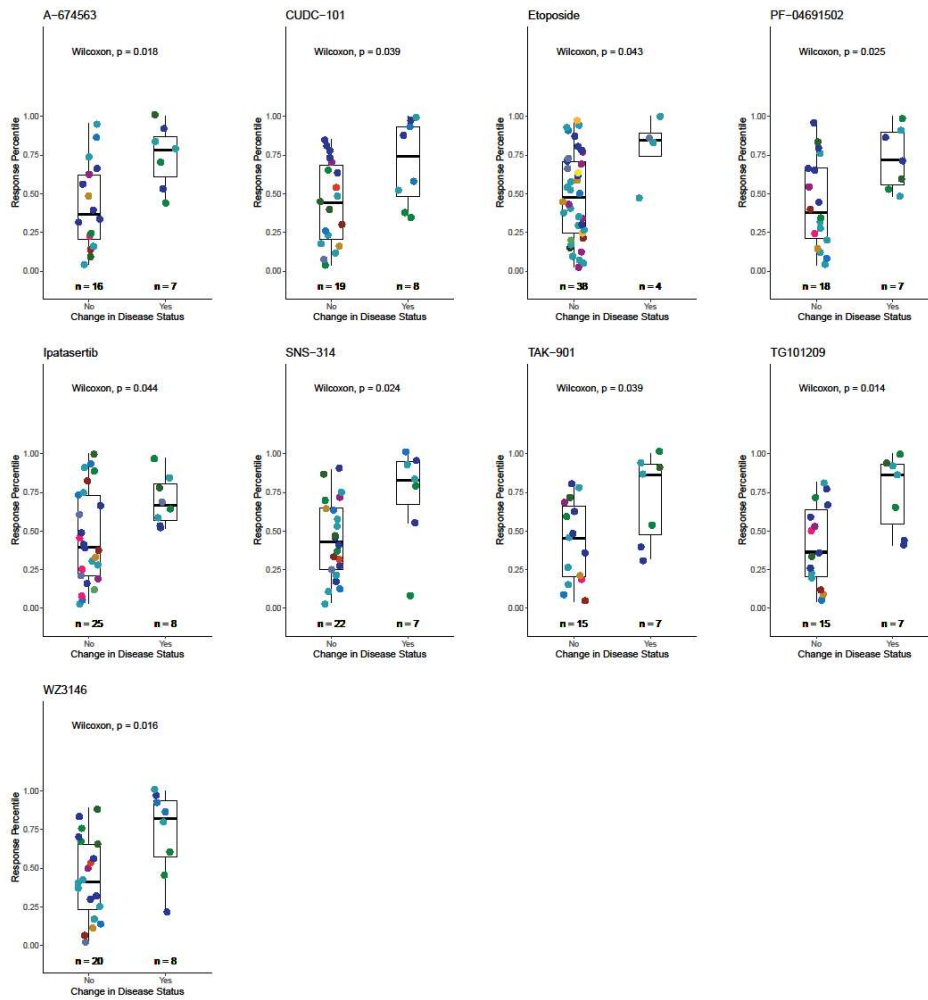
**Figure S3.9: Additional drugs with correlation between organoid sensitivity and change in disease status.** All samples screened with a drug are ranked from lowest viability (low viability percentile) to highest viability (high viability percentile) and plotted according to the rank. Primary drug targets are shown next to each drug name. The color of each point represents the diagnosis of the individual samples screened with the drug of interest. Statistical significance is tested by performing Wilcoxon Rank Sum Test.
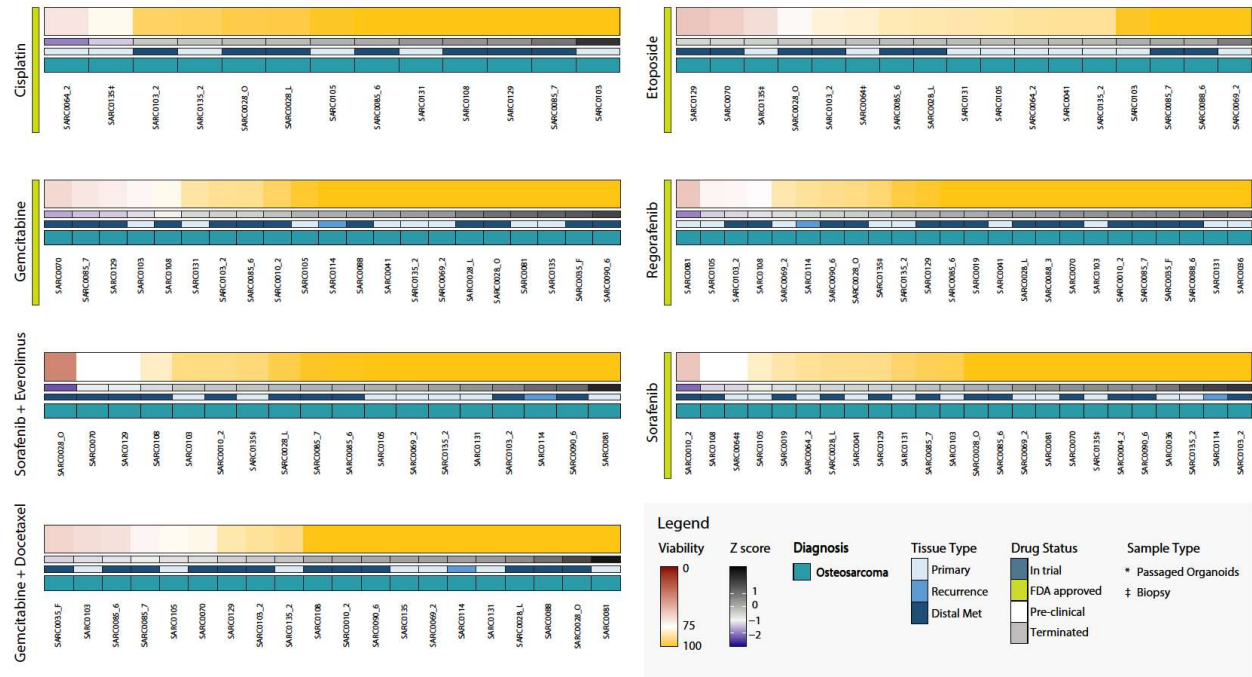
Figure S3.10: Osteosarcoma organoid sensitivity to treatment of NCCN recommended regimens. Heatmaps of organoid sensitivity to selected drugs from the NCCN recommendations were screened at 1 μM. Organoid viability for each sample is normalized to the mean organoid response to treatment with the selected drug across samples. Each column is a unique specimen, darker shades of red indicate greater sensitivity to treatment. Colored bars underneath each heatmap indicate the Z-score, lesion type, and diagnosis of each sample.

63
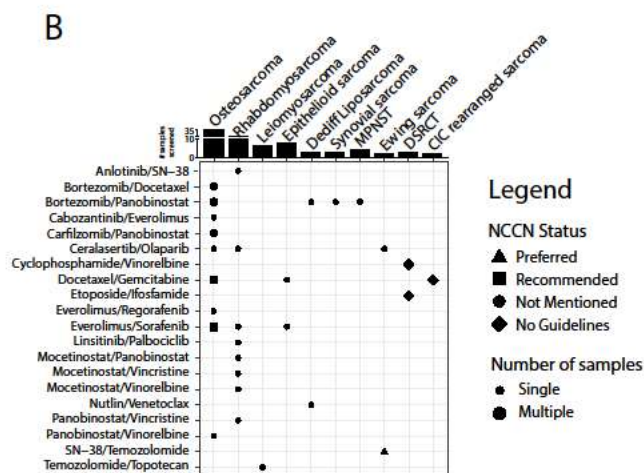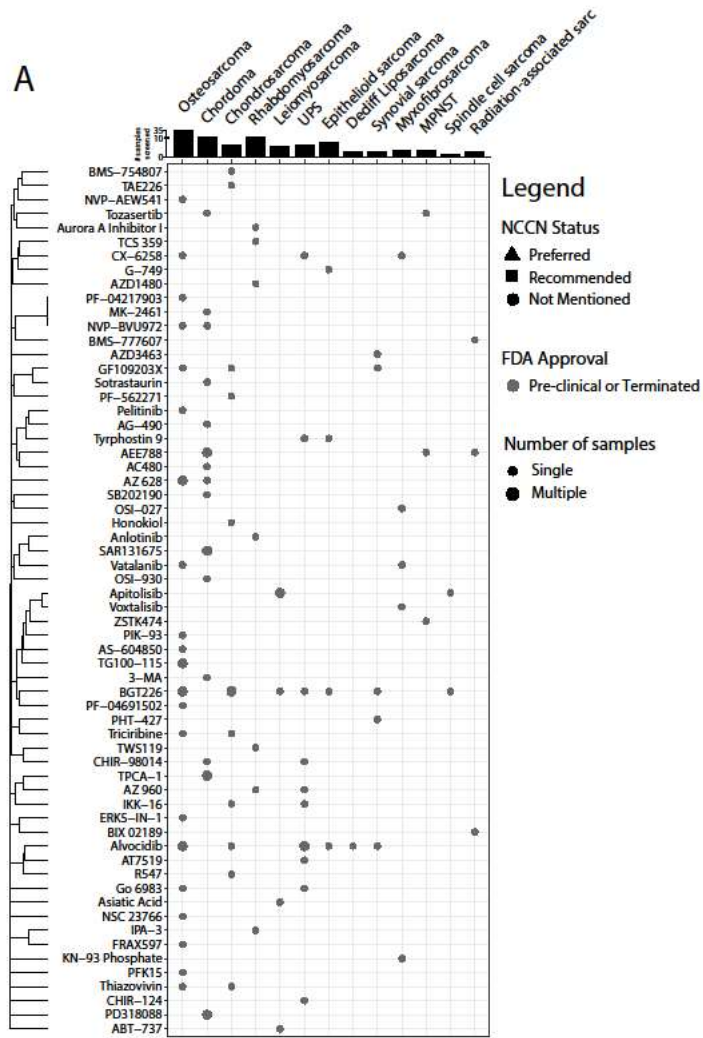
Figure S3.11: Drug availability and NCCN Guidelines status by histological subtype. We selected drug-diagnosis pairs of interest by cross-referencing the five most effective drugs for each sample with the 25% most responsive samples for each drug. **(A)** Single agent drugs that are not FDA approved are shown for each unique drug-diagnosis combination. The shape of the point indicates the current NCCN Guidelines for each drug. Triangles indicate drugs that are indicated as a preferred regimen. Squares signify drugs that are recommended for the subtype of interest and circles indicate that the drug is not currently discussed in the NCCN guidelines[1,2]. Diamond shape signifies that the histologic subtype has no guidelines, such as DSRCT and CIC rearranged sarcoma. The size of the marker indicates whether a single sample or multiple samples of a given histologic subtype was found to be among the five most effective for a drug. Drugs are clustered by similarity in gene targets using Jaccard distance. The number of samples screened for each histologic subtype is shown above. **(B)** Similar analysis is performed for combinational regimens and their NCCN recommendations across sarcoma histological subtype.
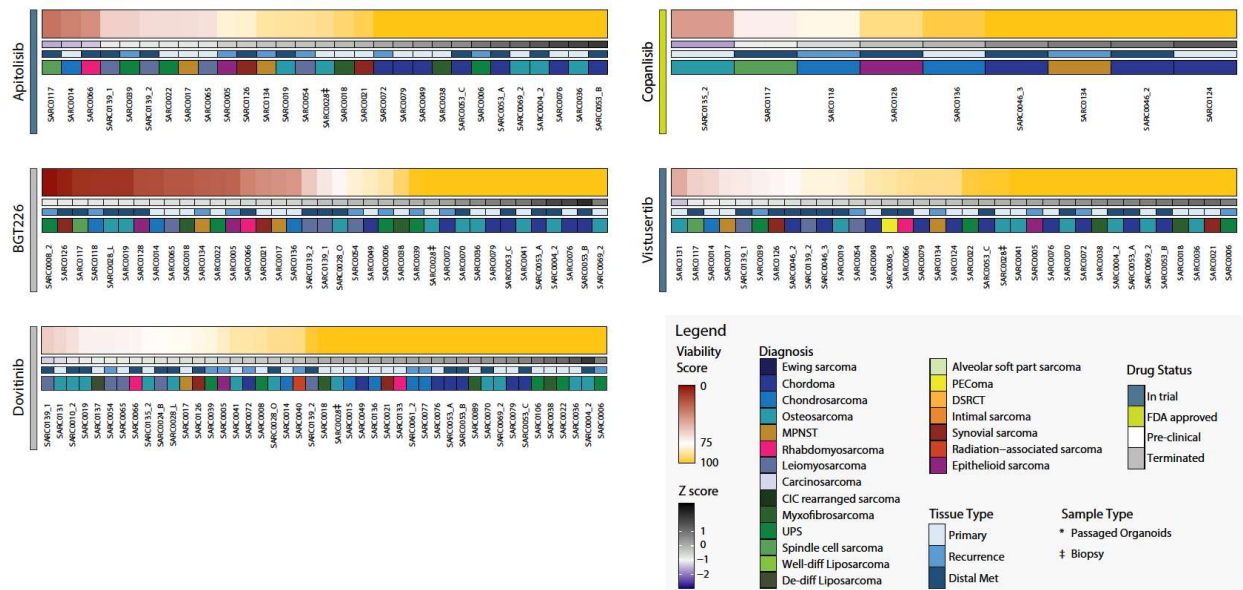
Figure S3.12: Organoid sensitivity to treatment of mTOR/PI3K targeting drugs, dovitinib, apitolisib, copanlisib, BGT226, and vistusertib. Heatmaps of organoid sensitivity to selected drugs from the NCCN recommendations were screened at 1 μM. Organoid viability for each sample is normalized to the mean organoid response to treatment with the selected drug across samples. Each column is a unique specimen, darker shades of red indicate greater sensitivity to treatment. Colored bars underneath each heatmap indicate the Z-score, lesion type, and diagnosis of each sample.

Acknowledgements

Chapter 4: Bioprinted organoids for high-content analysis with interferometry

As established in Chapter 3, high-throughput drug screening using tumor organoids is a viable approach to investigate tumor biology and identify therapeutic leads. However, organoid models suffer from difficulty in scale up and analysis. For example, manually seeded organoids coupled to destructive endpoint assays allow for the characterization of response to treatment, but do not capture the transitory changes and intra-sample heterogeneity underlying clinically observed resistance to therapy. We therefore developed a pipeline to generate bioprinted tumor organoids linked to label-free, real-time imaging *via* high-speed live cell interferometry (HSLCI) and machine learning-based quantitation of individual organoids. Bioprinting cells gives rise to 3D organoid structures that preserve tumor histology and gene expression. HSLCI imaging in tandem with machine learning-based image segmentation and organoid classification tools enables accurate, label-free parallel mass measurements for thousands of bioprinted organoids. We demonstrate that our method quantitatively identifies individual organoids as insensitive, transiently sensitive, or persistently sensitive to specific treatments. This opens new avenues for rapid, actionable therapeutic selection using automated tumor organoid screening.

Introduction

Functional precision oncology involves exposing tumor cells from individual patients to candidate therapeutic interventions *ex vivo*[33,35,126,127]. By monitoring response, treatment regimens with a higher probability of success can be prioritized[9,10,59,128,129].

These types of assays can provide useful sensitivity profiles even for tumors that lack currently actionable genomic alterations, and are thus incompatible with genomic-based precision medicine approaches[130], By directly measuring the effect of drugs on tissues or cells, functional assays can inform on the therapeutic resistance and sensitivity landscape of tumors without requiring full knowledge of the underlying molecular vulnerabilities *a priori*[31,32].

The broadly adopted model systems used in screening assays to identify possible leads all have limitations. Two-dimensional cell lines are relatively simple and inexpensive to culture but fail to represent the architecture, behavior and drug response of native tissue[131,132]. Mouse models have additional complexity but carry inherent, species-specific variations that limit their translation to human patients[133]. Patient-derived xenograft (PDX) models aim to better recapitulate human cancers yet are constrained by the large cost and time associated with their use, making large drug screening studies practically challenging[134]. Three-dimensional (3D) tumor organoids are promising models for precision medicine that can be established rapidly and effectively from a variety of cell types and tissue sources, and accurately mimic a patient's response to therapy[9,10,32,59,127,129,135]. They are physiologically-relevant, personalized cancer models well-suited for drug development and clinical applications[36,136]. The key outstanding limitations to the broad adoption of organoid-based screenings remain the time-intensive and operator-to-operator susceptibility of the cell seeding steps as well as destructive, population-level approaches required for subsequent organoid analysis[137].

To overcome these limitations, we developed an organoid screening pipeline that combines automated cell seeding *via* bioprinting with high-speed live cell interferometry

(HSLCI) and machine learning-based image segmentation and classification and for non-invasive, label-free, real-time organoid imaging. The new pipeline is based on our previously developed screening approach that takes advantage of patient-derived tumor organoids seeded in a mini-ring format to automate high-throughput drug testing, with results available within one week from surgery[9,10,138]. We automate cell seeding by including bioprinting, a technique for precise, reproducible deposition of cells in bioinks onto solid supports, to seed the organoids[139]. Bioprinting has rapidly gained traction in cancer biology as embedded cells can interact with physiological microenvironment components in the bioink to create physiologically-representative tumor models[137,139–143].

We then implement HSLCI to rapidly monitor changes in dry biomass and biomass distribution of single organoids over time. HSLCI, a type of quantitative phase imaging (QPI)[144–149], measures the phase shift of light transmitted through the sample using a wavefront sensing camera[147,150]. Due to the defined linear relationship between the refractive index and mass density of biomolecules in solution, which is invariant with respect to changes in cellular content[151–155], measured phase shifts can be integrated across the area of an image and multiplied by a conversion factor to obtain the dry biomass of imaged cells[150]. Biomass is an important metric of organoid fitness as its dynamics are the direct result of biosynthetic and degradative processes within cells[150]. In previous work, QPI measurements of biomass changes allowed resolution of drug-resistant and drug-sensitive cells in 2D cell culture models within hours of treatment[144–146,148,149,156,157]. HSLCI-measured response profiles have also been shown to match drug sensitivity from patient-derived xenograft (PDX) mouse models of breast cancer[145]. However, HSLCI has been applied exclusively to screening cancer lines grown in 2D or

single-cell suspensions of excised PDX tumors thus far[144–149]. We demonstrate here that bioprinted organoids deposited in uniform, flat layers of extracellular matrix allow label-free, real-time, non-destructive quantification of growth patterns and drug responses at single-organoid resolution.

Results

Bioprinting enables seeding cells in Matrigel in suitable geometries for quantitative imaging applications.

To address current limitations[9,10,138] and facilitate non-invasive, label-free, real time imaging of 3D organoids by HSLCI, we created an automated cell printing protocol using an extrusion bioprinter. As a base, we used an organoid platform that seeds cells in mini-rings of Matrigel around the rim of 96-well plates, with the empty center allowing the use of automated liquid handlers, facilitating media exchanges and addition of perturbagens[9,10,138]. We retained the empty center architecture but altered the geometry to bioprint mini-squares of cells in Matrigel (**Figure 4.1A**). Positioning the sides of the square in the HSLCI imaging path allows sampling of a larger area and limits imaging artifacts caused by uneven illumination at well edges[147] (**Figure 4.1A**). Our bioprinting protocol entails suspending cells in a bioink consisting of a 3:4 ratio of medium to Matrigel. This material is then transferred to a print cartridge, incubated at 17°C for 30 minutes, and bioprinted into each well at a pressure between 12 and 15 kPa, resulting in ~200 μm prints on standard glass-bottom plates (**Figure 4.1B**).

We next coupled these bioprinted organoids to an HSLCI platform. HSLCI uses a wavefront sensing camera and a dynamic focus stabilization system to perform

continuous, high-throughput, label-free, quantitative phase imaging of biological samples, tracking their biomass changes over time[144,145]. However, efficient high-throughput QPI of 3D organoids using HSLCI is hindered by geometry considerations; when an object of interest is out of focus, measured phase shifts cannot be assumed to maintain a direct relationship with mass density[147]. Thus, we attempted to generate thinner layers of Matrigel to yield a relatively greater number of organoids in focus that can be quantitatively assessed at any given time. To generate thinner ($<$100 μm) constructs amenable to efficient, label-free HSLCI imaging, we increased the hydrophilicity of the surface of 96-well glass-bottom plates by oxygen plasma treatment[158]. We developed 3D masks composed of BioMed Amber Resin (FormLabs) to selectively functionalize the region of interest (**Figure S4.1**). Bioprinting post-plasma treatment generated uniform mini-squares with organoids closely aligned on a single focal plane at ~70 μm thickness (**Figure 4.1B**). These thin, printed mini-squares are amenable to massively parallel QPI by HSLCI as we aligned the legs of the bioprinted mini-square construct with the HSLCI imaging path (**Figure 4.1C**).

Lastly, we verified that the printing parameters used did not altered cell viability by directly comparing MCF-7 cells manually seeded according to our established protocol[9,10,138] to cells printed through a 25G needle (260 μm inner diameter) using extrusion pressures ranging from 10 to 25 kPa. We did not observe any reduction in cell viability as measured by ATP release assay (**Figure 4.1D**). These results are consistent with the existing literature as reductions in cell viability are often associated with higher print pressures (50-300 kPa)[159,160]. Taken together, this describes a method for bioprinting layers suitable for high-throughput HSLCI imaging without impacting cell

viability, while supporting automated liquid-handling for high-throughput applications[9,10,138,161,162].
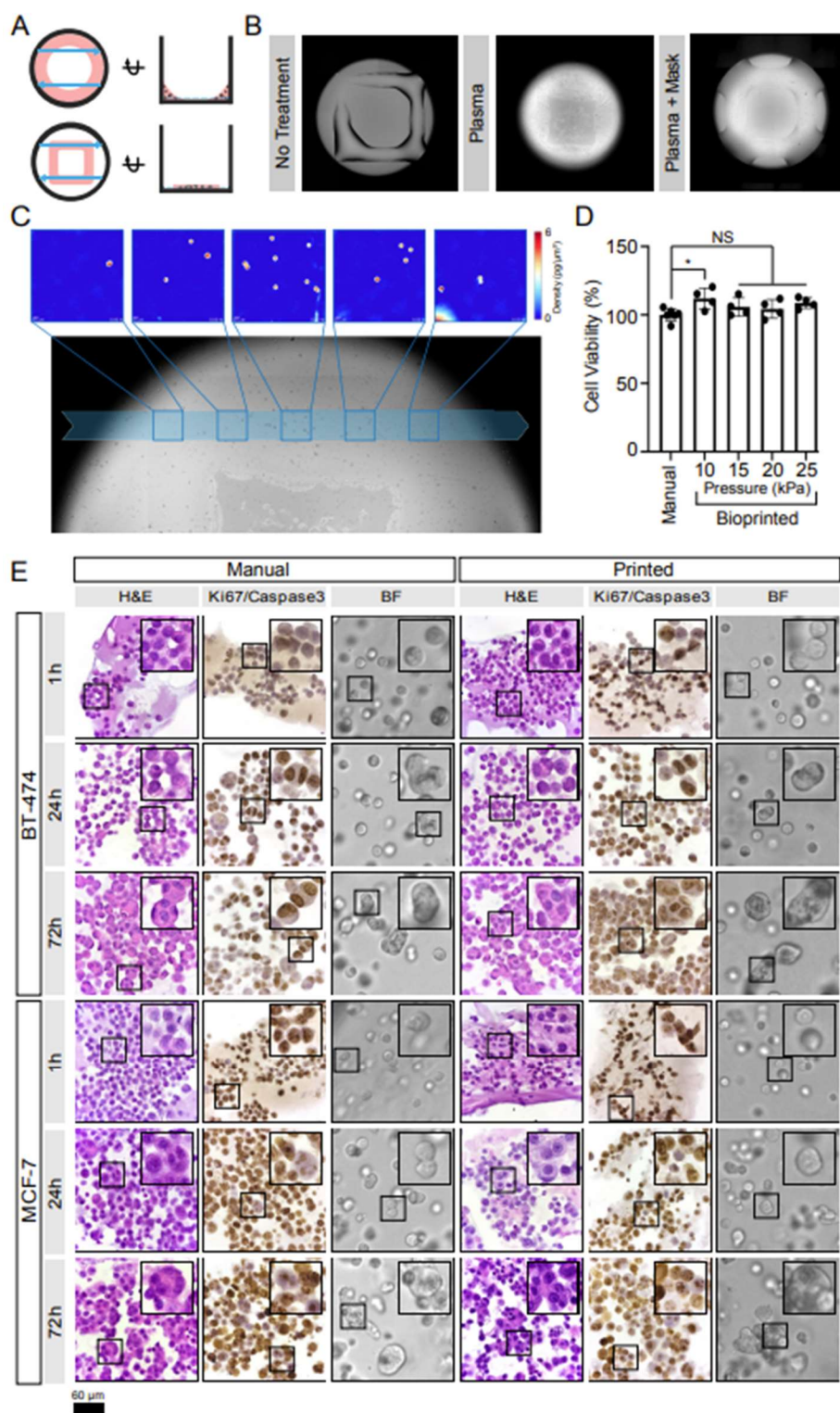
Figure 4.1: Bioprinting enables seeding of Matrigel-encapsulated organoids optimized for efficient HSLCI. (A) Schematic of wells with mini-rings (top) and mini-squares (bottom) relative to HSLCI imaging path (blue arrows). The top views (left) demonstrate that transitioning from rings to squares increases the area of material in the HSLCI imaging path. The side views (right) show that organoids in the square geometry align to a single focal plane better than organoids in a ring. **(B)** Plasma treatment of the well plate prior to printing optimizes hydrogel construct geometry. Bioprinting Matrigel onto untreated glass (left) generates thick (~200 μm) constructs that decreases the efficiency of organoid tracking by increasing the number of organoids out of the focal plane. Whole well plasma treatment (middle) increases the hydrophilicity of all well surfaces causing the Matrigel to spread thin (~50 μm) over the surface; however, the increased hydrophilicity also draws bioink up the walls of the well. Plasma treatment with a well mask facilitates the selective treatment of a desired region of the well (right). This leads to optimal constructs with a uniform thickness of approximately 75 μm across the imaging path. **(C)** Individual organoids can be tracked over time across imaging modalities. Five representative HSLCI images are traced to the imaging path across a brightfield image. **(D)** Cell viability of printed *versus* manually seeded MCF-7 cells in a Matrigel-based bioink. A one-way ANOVA was performed (p = 0.0605) with *post-hoc* Bonferroni's multiple comparisons test used to compare all bioprinted conditions against the manually seeded control. Adjusted p-values were 0.0253, 0.6087, >0.9999, 0.1499 for print pressures 10, 15, 20, 25 kPa, respectively. **(E)** H&E staining shows the development of multicellular organoids over time regardless of seeding method. The prevalence and size of multinuclear organoids increase with culture time. Ki-67/Caspase-3 staining demonstrates that most cells remain in a proliferative state throughout culture time. While apoptotic cells were observed in organoids cultured for 72 hours, the majority of cells show strong Ki-67 positivity. All images are 40X magnification and insets are 80X magnification. Ki-67 is stained brown, and caspase-3 is stained pink.

Bioprinted tumor organoids maintain histological features of manually seeded organoids.

To verify that bioprinting did not perturb tumor biology, we directly compared the histology and immunohistochemical profiles of bioprinted and hand-seeded organoids from two breast cancer cell lines, BT-474 and MCF-7. These lines were selected for their differing molecular features such as their human epidermal growth factor receptor 2 (HER2) and estrogen receptor (ER) status[163]. We seeded cells as maxi-rings (1×10^5

cells/ring) to obtain sufficient material for downstream characterization. Cells were either manually seeded into 24 well plates[9,10,138] or bioprinted into 8-well plates at an extrusion pressure of 15 kPa. The bioprinted cells and resulting organoid structures were morphologically indistinguishable from manually seeded ones in brightfield images and hematoxylin and eosin (H&E)-stained sections taken 1, 24 and 72 hours after seeding (**Figure 4.1E**). Both bioprinted and manually seeded samples grew in size over time and bioprinting did not alter proliferation (Ki-67 staining) or apoptosis (cleaved caspase-3; **Figure 4.1E**). Hormone receptor status was unaltered, as shown by IHC for HER2 (**Figure S4.3**) and ER (**Figure S4.4**), and in agreement with literature reports for both cell types[164–167]. Thus, bioprinting did not influence organoid histology.

Bioprinted and manually seeded organoids are molecularly indistinguishable.

While bioprinted organoids are histologically indistinguishable from manually-seeded ones, this does not preclude molecular changes caused by the printing process. We therefore performed a detailed analysis of the transcriptomes of manually seeded and bioprinted cells 1-, 24- and 72-hours post-seeding. We assessed the distributions of 27,077 transcripts and clustered these into deciles based on their median abundance and found no significant differences between seeding approaches (**Figure 4.2A**). The overall transcriptomes of manually seeded and bioprinted organoids were extremely well-correlated (**Figure 4.2B**), with no individual transcripts differing significantly in abundance in either cell line even at very permissive statistical thresholds (0/27,077 genes, q <0.1, Mann-Whitney U-test, **Figure 4.2C**).

We next examined pre-mRNA alternative splicing events since these can induce functional changes even in the absence of variations in mRNA levels[168–170]. The density of exon-inclusion and exon-skipping isoforms was unchanged, with no individual fusion isoforms associated with the organoid printing method in either cell line (0/8,561, q <0.1, Mann-Whitney U-test; **Figure 4.2D**). Similarly, the number of fusion transcripts were not associated with seeding method (p = 0.17, Mann-Whitney U-test), although large numbers of fusions were detected in only one or two samples, reflecting the wide-spread *trans* splicing and genomic instability of immortalized cell lines[171] (**Figure S4.5A**). Finally, there were no significant differences in the number or nature of RNA editing sites between printed and manually developed organoids (p = 0.48, Mann-Whitney U-test; **Figure S4.5B**). These findings demonstrate that our bioprinting protocol does not significantly impact the molecular characteristics of tumor organoids.
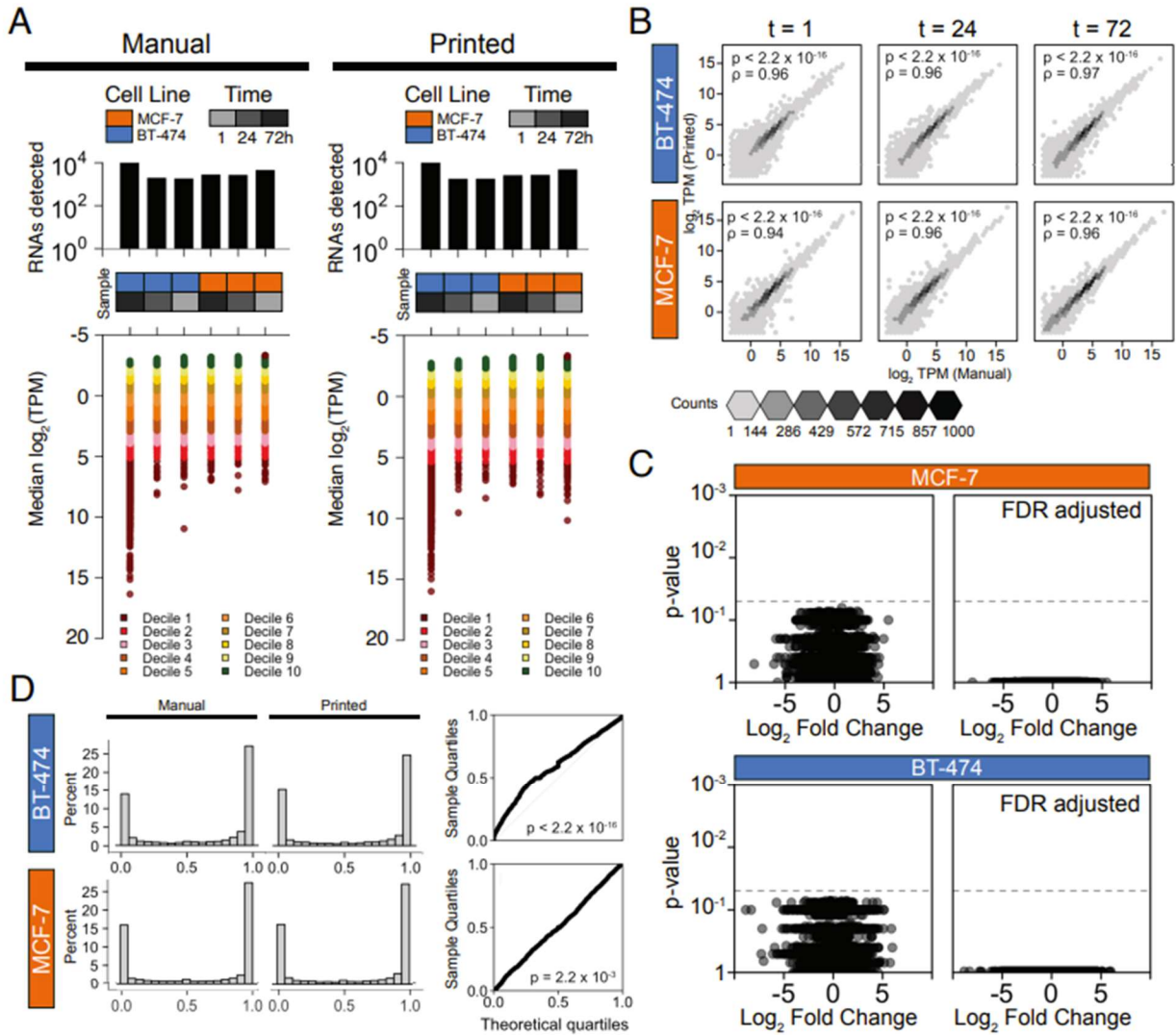
Figure 4.2: Bioprinting does not significantly alter organoid transcriptomes. (A) Distributions of total number of transcripts detected (above) and transcript abundances (below) measured as transcripts per million (TPM) organized into groups of deciles based on median abundance. **(B)** RNA abundances ($\log_2$ TPM) of manually seeded and bioprinted organoids at three different time points (t = 1, 24, and 72 hours). Spearman's ρ was assessed for each association. We found strong associations between RNA abundances derived from printed and manually seeded organoids for both cell lines. **(C)** Volcano plots of Mann-Whitney U-test results for MCF-7 and BT-474 organoids with unadjusted p-values (left) and false discovery rate (FDR) adjusted p-values (right) comparing the RNA abundances of transcripts between manually seeded and printed tumor organoids. Fold change of RNA transcripts were assessed and $\log_2$ transformed. No transcripts were preferentially expressed based upon seeding method for organoids of either cell line (n = 0 out of 27,077 genes, q-value <0.1, Mann-Whitney U-test). **(D)** Median percent spliced in (PSI) of exon skipping isoforms were similarly distributed among BT-474 (top) and MCF-7 (bottom) derived organoids. Distribution of isoforms is consistent between manually seeded (left) and bioprinted (right) organoids. PSI of 1 indicates that the isoform is exclusively an exon inclusion isoform, while a PSI of 0 indicates that the isoform is exclusively an exon skipping isoform.

Machine learning-based image segmentation and organoid classification enables single-organoid analysis.

Our complete pipeline includes cell bioprinting (day 0), organoid establishment (day 0-3), full media replacement (day 3, **Figure 4.3A**) followed by transfer to the HSLCI incubator. Within 6 hours of media exchange, the plates are continuously imaged through 72 hours post-treatment. At the end of the imaging period, we perform an endpoint ATP assay to assess cell viability (**Figure 4.3A**). Interferograms collected by HSLCI are first converted to phase shift images using the SID4 software development kit (GPU version, v741)[147]. These images are then analyzed using two types of machine-learning algorithms.

To reliably identify unique organoids within each imaging frame despite the presence of background noise, debris, and out-of-focus organoids, we performed image

segmentation using a U-Net architecture[104] with a ResNet-34[10,123] as the backbone. U-Net, a type of convolutional neural network (CNN), consists of an encoder that extracts rich feature maps from an input image and a decoder that expands the resolution of the feature maps back to the image's original size. The long skip connections between the encoder and decoder propagate pixel-level contextual information into the segmented masks. The resulting segmentation images are very detailed even when provided small training datasets. The training dataset consisted of manually labeled organoids in 100 randomly selected imaging frames. This model created binary masks indicating whether each pixel of the image belonged to an organoid or the background with a mean Jaccard Index of 0.897 ± 0.109 at the 95% confidence level (**Figure S4.6**). The CNN reliably created masks omitting phase artifacts resulting from aberrant background or out-of-focus organoids (**Figure S4.6**).

Next, we determined the mass of each organoid in segmented masks by integrating the phase shift over the organoid area and multiplying by the experimentally determined specific refractive increment[146,151,153,154,172]. Organoids in subsequent frames were assembled into time coherent tracks using TrackMate[173,174] and filtered using an XGBoost classifier[175] we developed to exclude organoids moving in and out of focus, frequently overlapping and/or separating from neighboring organoids, or incorporating debris. We validated the model via cross-validation with 3-fold resampling of the sample population. The 3-fold resampling cross-validation score of the classifier was 91% with 93.5% accuracy. We also observed trends in the features used to classify each track, with excluded tracks typically have an increased number of missing frames as well as smaller interquartile ranges, and smaller initial and final sizes (**Figure S4.7**).
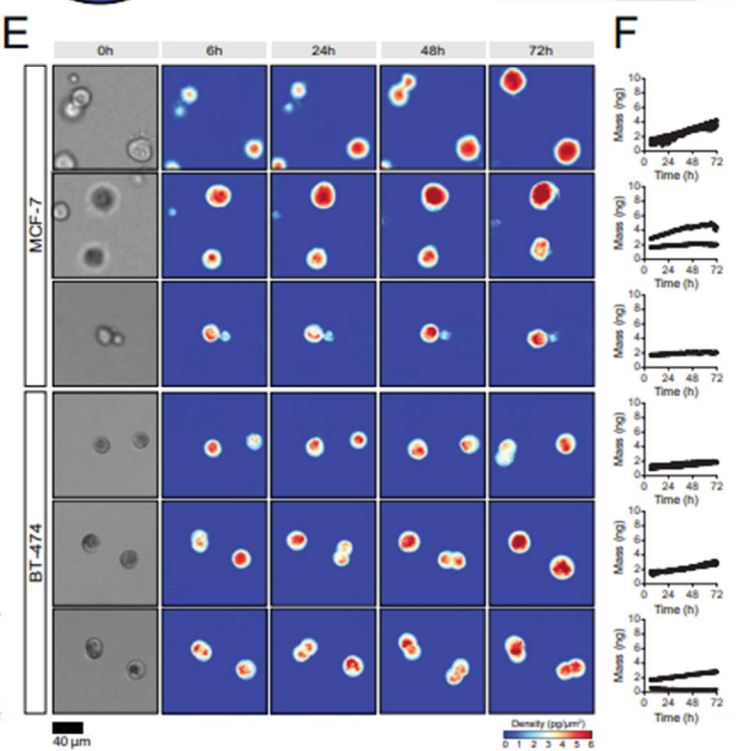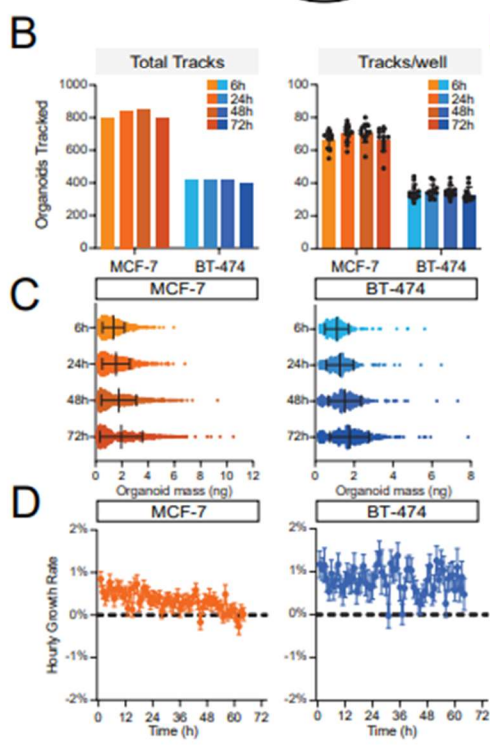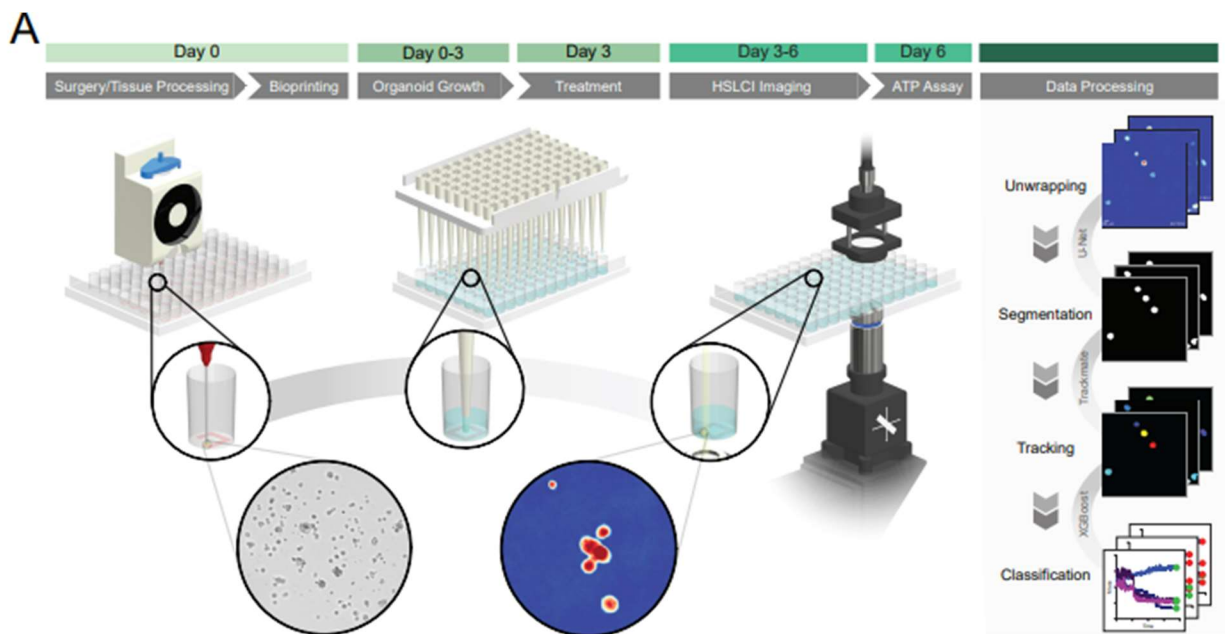
Figure 4.3: Bioprinting enables single-organoid tracking with high-speed live cell interferometry. (A) Extrusion-based bioprinting is used to deposit single-layer Matrigel constructs into a 96-well plate. Organoid growth can be monitored through brightfield imaging. After treatment, the well plate is transferred to the high-speed live cell interferometer for phase imaging. Coherent light illuminates the bioprinted construct and a phase image is obtained. Organoids are tracked up to three days using the HSLCI and changes in organoid mass are measured to observe response to treatment. **(B)** Total number of organoid tracks (left) and mean number of tracks per well (right) at each time point. The total number of organoid tracks across interpretable, replicate wells was 67 for MCF-7 organoids (n = 8), and 101 for BT-474 organoids (n = 12). **(C)** Mass distribution of tracked organoids 6 and 48 hours after treatment. Black bars represent the mean with error bars representing the standard deviation. **(D)** Hourly growth rate (percent mass change) of tracked MCF-7 (left) and BT-474 (right) organoids cultured in 1% DMSO. **(E)** Representative images of MCF-7 and BT-474 organoids tracked with HSLCI. Brightfield images of organoids taken immediately before treatment are shown on the left. (F) Calculated mass of each representative organoid over time.

Trends in mass accumulation of bioprinted organoids can be quantified by HSLCI with single-organoid resolution.

HSLCI-based imaging allowed continuous tracking of n=921 MCF-7 organoids in 12 replicate wells (median: 78.5 organoids/well) and n=438 BT-474 organoids in 12 replicate wells (median: 36 organoids/well, **Figure 4.3B**). Due to organoids moving in and out of the field-of-view, the number of organoids tracked at each time point varied slightly. Overall, we tracked an average of 821 ± 28 MCF-7 organoids and 412 ± 9 BT-474 organoids at any given time throughout imaging (**Figure 4.3B**).

Unlike chemical endpoint assays or other live imaging modalities, HSLCI-based imaging facilitates parallel mass measurements of individual organoids. The initial average organoid mass was larger for MCF-7 (1.36 ± 0.84 ng) than BT-474 organoids (1.12 ± 0.61 ng, **Figure 4.3C**). The difference persisted throughout the entire imaging duration (**Table S4.1**). BT-474 cells grew at a rate of 0.80 ± 6.07% per hour while MCF-7

organoids demonstrated slower average hourly growth rates (0.33 ± 4.94% per hour, **Figure 4.3D**). The growth rate of the 3D BT-474 organoids is slightly slower than that observed after 6 hours in 2D culture (approximately 1.3%), while the MCF-7 organoids showed a much lower growth rate than previously reported 2D cultures (approximately 1.7%)[156]. We also observed positive associations between initial organoid mass and growth rate in both cell lines; however, the association between these factors is stronger for MCF-7 organoids (**Figure S4.8**). The varying degrees of association provide evidence of cell-line specific growth characteristics that cannot be measured using any other analytical method.

Drug responses of organoids can be quantified by HSCLI.

We then tested the utility of our platform in detecting drug responses in high-throughput 3D screenings (**Figure 4.3A**). As proof-of-principle we tested staurosporine, a non-selective protein kinase inhibitor with broad cytotoxicity[176], neratinib, an irreversible tyrosine kinase inhibitor targeting EGFR and HER2[177], and lapatinib, a reversible tyrosine kinase inhibitor also targeting EGFR and HER2[178]. Staurosporine and neratinib were tested at 0.1, 1, and 10 µM, while lapatinib was screened at 0.1, 1, 10, and 50 µM (**Figure 4.4 and S4.9**). These concentration ranges include and extend beyond the maximum plasma concentration reported for both lapatinib (4.2 µM)[179] and neratinib (0.15 µM)[180].

Representative HSLCI images demonstrate a range of responses to treatment (**Figure 4.4A**). The average masses at the start of the imaging window (6 hours post-treatment) did not significantly differ from the vehicle control (**Figure 4.4B, Table S4.1**). After 24, 48, and 72 hours, we observed significant differences in a number of treated

samples (**Table S4.1**). After 24 hours, control MCF-7 organoids averaged 1.56 ± 1.05 ng, while those treated with 1 µM and 10 µM staurosporine showed significant reductions in average masses to 1.18 ± 0.77 ng (p = 1.93 x 10^{-9}, Mann-Whitney U-test) and 1.11 ± 0.69 ng (p = 1.49 x 10^{-13}, Mann-Whitney U-test), respectively. BT-474 organoids showed a similar pattern after 24 hours with control organoids averaging masses of 1.27 ± 0.69 ng while staurosporine-treated organoids averaged 0.76 ± 0.39 ng (1 µM, p = 2.27 x 10^{-32}, Mann-Whitney U-test) and 0.79 ± 0.44 ng (10 µM, p = 1.59 x 10^{-28}, Mann-Whitney U-test). The normalized growth curves (**Figure S4.10**) rapidly show response to treatment with 1 µM staurosporine.

Responses to lapatinib and neratinib reflected cell-specific trends. BT-474 organoids quickly showed sensitivity to both neratinib and lapatinib, while MCF-7 organoids only exhibited sensitivity to 10 µM lapatinib and neratinib (**Figures 4.4B and 4.5A, Tables S4.1 and S4.2**). After 24 hours, the mean mass of the BT-474 organoids treated with 0.1 µM neratinib decreased to 0.97 ± 0.44 ng from 1.27 ± 0.69 ng (p = 4.86 x 10^{-6}, Mann-Whitney U-test) and organoids treated with 1 µM lapatinib decreased to 1.00 ± 0.49 (p=3.37 x 10^{-5}, Mann-Whitney U-test).
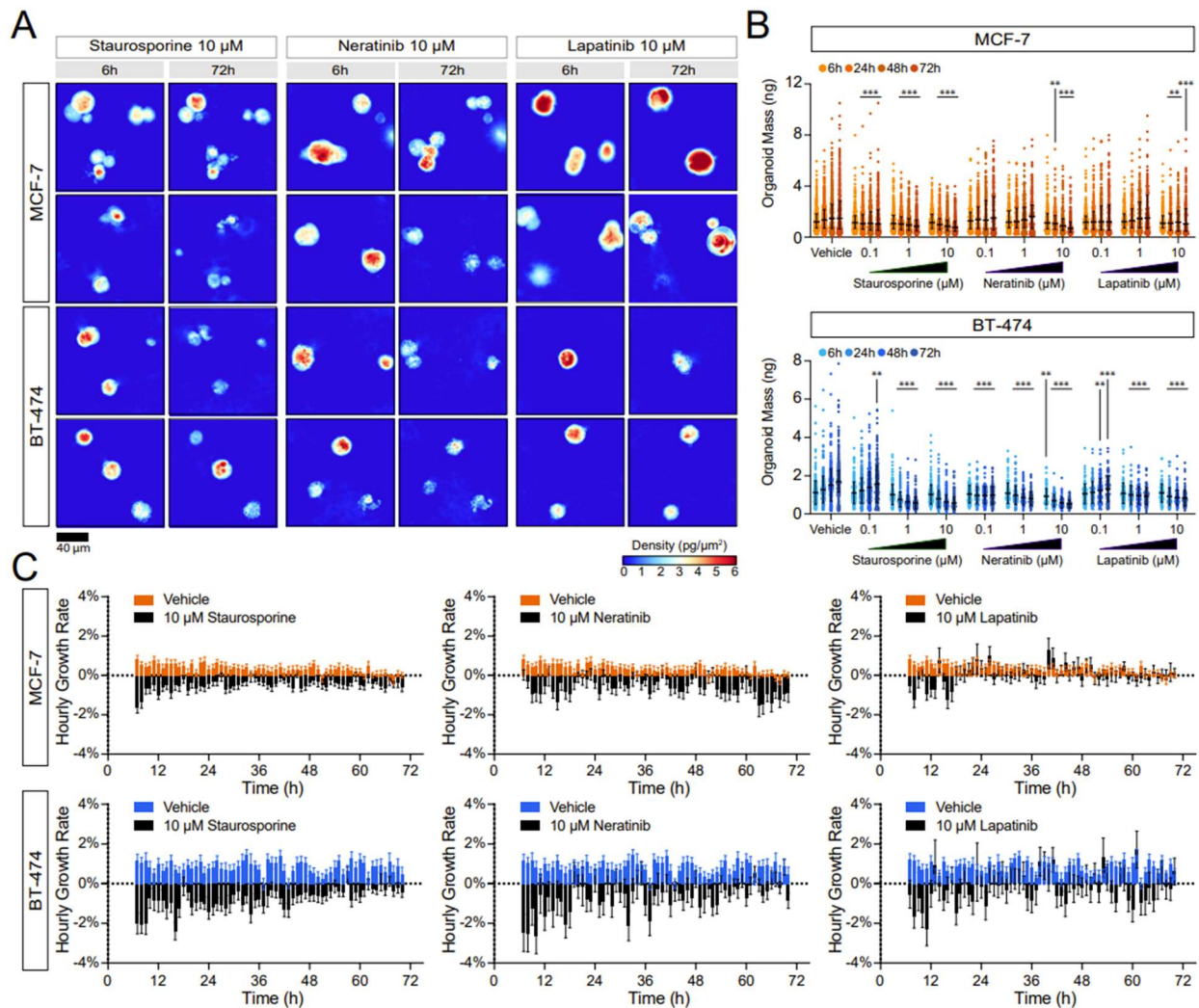
Figure 4.4: HSLCI enables high-throughput, longitudinal drug response profiling of 3D organoid models of cancer. (A) Representative images of organoids treated with 10 µM staurosporine, 10 µM neratinib, and 10 µM lapatinib. **(B)** Mass of tracked MCF-7 and BT-474 organoids by treatment. Each bar represents the mass distribution at 6-, 24-, 28-, and 72-hours post-treatment (left to right). Black horizontal bars represent the median with error bars representing the interquartile range of the distribution. **(C)** Hourly growth rate comparisons (percent mass change) between organoids treated with 10 µM staurosporine and vehicle, 10 µM neratinib and vehicle, and 10 µM lapatinib and vehicle. $p<0.05$ is denoted by *, $p<0.01$ is denoted by **, and $p<0.001$ is denoted by ***.

Intra-sample heterogeneity of organoid drug responses.

Our combination of HSLCI with ML-based organoid tracking provides per-organoid mass tracking, allowing quantitation of intra-sample heterogeneity (**Figure 4.3E-F, Supplementary Videos 4.1 & 4.2**). We assessed the ratio of organoids that gained, lost, and maintained mass over 12, 24, 48, and 72 hours for both control and treated samples (**Figure 4.5A, Table S4.2**). In the absence of drug treatment, 11.9% of BT-474 organoids lost more than 10% of their initial mass and 80.9% gained more than 10% of their initial mass over 72 hours. In contrast, only 50.8% of MCF-7 organoids gained mass and 32.6% lost mass. This heterogeneity in organoid populations increases over time, with 23.2% of MCF-7 organoids gaining more than 10% mass within 12 hours. This proportion nearly doubles to 44.8% after 24 hours but remains consistent at 48.6% and 50.8% after 48 and 72 hours, respectively. This pattern differs from BT-474 organoids as the population of organoids that gained mass continually increases over the first 48 hours before plateauing between 48 and 72 hours. BT-474 organoids that gained >10% mass increased from 30.1% after 12 hours, to 62.4% after 24 hours, and 80.9% after 48 and 72 hours.

Upon treatment, we could observe both inter-sample (MCF-7 vs BT-474) as well as intra-sample heterogeneity. In the presence of the HER2-targeting lapatinib (10 µm), 37.7% of MCF-7 continued to grow and an additional 10.0% maintained their mass after 72 hours of treatment (**Figure 4.5A, Table S4.2**). When treated with 10 µM neratinib, only 4.5% of MCF-7 organoids gained mass, while 18.1% remained stable. In contrast, BT-474 organoids showed greater sensitivity to both drugs, with 11.4% growing and 73.7% losing mass with 10 µM lapatinib treatment (vs 11.9% for controls), and no organoids growing after 10 µM of neratinib for 72 hours (**Figure 4.5A, Table S4.2**). A subset of BT-474 organoids showed high sensitivity to 0.1 µM of both lapatinib and neratinib. In response to lapatinib, 12.8% of BT-474 organoids lost mass, while 17.9% maintained stable mass. When treated with neratinib, 49.1% lost mass and 22.4% had stable mass. Both responses contrasted with organoids treated with vehicle, of which 11.9% lost mass and 7.2% maintained mass. The heightened sensitivity of BT-474 cells to lapatinib and neratinib is expected given the higher expression of HER2 found in these cells[163] (**Figure S4.3**).

A fraction of organoids in all treatment-cell combinations were unresponsive to the drugs tested (**Figure 4.5A, Figure S4.10, Table S4.2**). These organoids grew at similar rates to vehicle-treated cells and comprised between 7.8 and 87.1% of all organoids depending on the cell line and drug. For example, 37.7% of MCF-7 organoids treated with 10 μM lapatinib grew after 72 hours, while an additional 10% maintained stable mass (**Table S4.2**). Similarly, when treated with 10 μM neratinib for 72 hours, nearly 8% of BT-474 organoids maintained their mass, and when exposed to 10 μM lapatinib for 72 hours, the proportion increases to over 25% (**Table S4.2**). Our findings are indicative of a resistant population of organoids that can be rapidly identified by HSLCI imaging. These persisters may provide a unique model for understanding *de novo* and acquired treatment resistance.

Lastly, to validate the responses measured by HSLCI, we performed an endpoint ATP-release assay on the same plates used for HSLCI imaging and assessed organoid viability at the end of the 72-hour treatment (**Figure 4.5B**). The ATP assay confirmed that both cell lines are highly sensitive to staurosporine with near-zero viability at the 1 and 10 μM concentrations. Additionally, BT-474 organoids show significant reductions in viability when treated with 0.1 μM lapatinib and 0.1 μM neratinib for 72 hours (**Table S4.3**). Overall, the results of the cell viability assay after 72 hours confirm the trends observed in as little as 6 hours by HSLCI but fail to capture intra-sample variability.
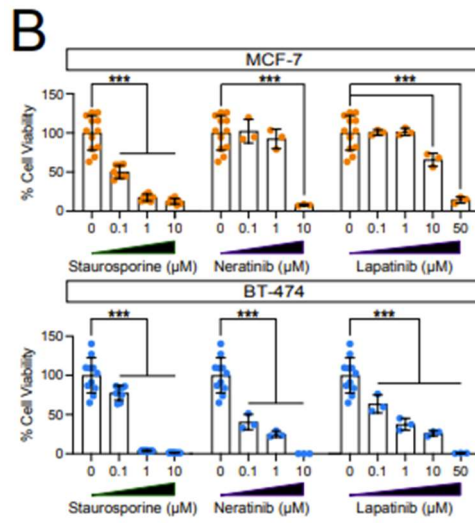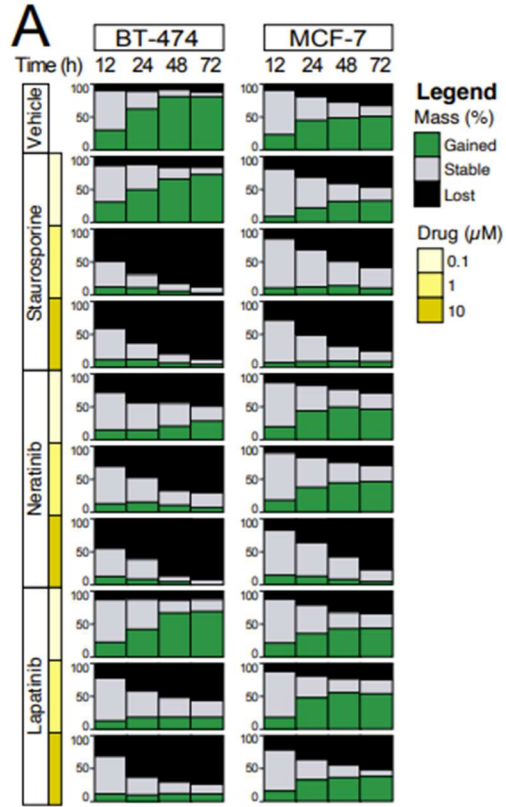
Figure 4.5: HSLCI enables identification of resistant and sensitive organoid subpopulations and discerns response to treatment earlier than a standard endpoint assay. (A) Plots showing the percentage of organoids in each condition that gain (green) or lose (black) more than 10% of their initial mass 12, 24, 48, 72 hours after treatment. **(B)** Percent cell viability of treated wells determined by an ATP-release assay. Statistical significance was assessed using an unpaired t-test with Welch's correction. $p < 0.05$ is denoted by *, $p < 0.01$ is denoted by **, and $p < 0.001$ is denoted by ***.

Discussion

Every newly diagnosed human cancer reflects a unique set of germline variation, somatic mutations, and microenvironmental influences[181]. Cancer therapy attempts to address this by personalizing treatment for individual patients[182,183]. The most common approach to date has been molecular precision medicine, which links therapeutic efficacy to molecular features of a tumor[16,33,184]. Functional precision medicine approaches, by contrast, bypass the need to learn drug-molecular associations by relating *ex vivo* response to clinical outcomes[6,59,185]. Key limitations towards the broad adoption of functional precision medicine have been the creation of physiological culture models, the development of high-throughput systems, and the difficulty in measuring organoid heterogeneity[126,186,187]. Here, we describe a new pipeline that overcomes these barriers by incorporating a robust 3D organoid bioprinting protocol and an imaging approach that facilitates single-organoid analysis of response to treatment.

We introduced bioprinting to enhance the throughput and consistency of our previously published organoid screening approaches[9,10,138]. We opted to print a Matrigel-based bioink due to its ability to preserve tumor characteristics *ex vivo*[9]; however, its weak mechanical integrity and its temperature-dependent viscosity and crosslinking behavior complicate its suitability for bioprinting[188]. To circumvent these limitations, we optimized a protocol that takes advantage of its temperature-dependent behavior to yield consistent mechanical properties for bioprinting. While the existing consensus is that consistent bioprinting with Matrigel is difficult to achieve, we show that simple, single-layer structures are attainable with strict temperature regulation. We further enhanced the quality of the Matrigel deposition by selectively modifying the print substrate with oxygen plasma treatment. The introduction of 3D plasma masks (**Figure S4.1**) facilitated the selective treatment of a square region in each well. The increased hydrophilicity of the substrate in

the exposed region guides the spreading of the material to ensure maximize consistency in deposition volume and construct thickness while preventing obstruction of the center of the well. Bioprinting allowed us to finely control the size and shape of the deposited gel constructs, facilitating the use of HSLCI for downstream analysis (**Figure 4.1**).

To our knowledge, this is the first reported use of live cell interferometry for label-free, time-resolved quantitative imaging of 3D organoid cultures. Previous studies have used interferometry to quantify the mass of individuals cells cultured on 2D substrates to study cell division[189], cytoskeletal remodeling[190], mechanical properties[191], and response to treatment[144–146]. Tomographic QPI has also been used to obtain high-resolution images of 3D objects such as cerebral organoids[192]. The primary challenge of adapting live cell interferometry for the mass quantitation of 3D organoids is maintaining the organoids in a single focal plane. The mass of organoids outside of the focal plane cannot be accurately calculated as phase information for out-of-focus planes is difficult to interpret[147]. We were able to circumvent this challenge by introducing bioprinting to generate uniform, thin constructs that maximize the number of organoids that could be tracked in parallel, and a machine-learning based organoid classifier to exclude out-of-focus and non-organoid objects from our analysis. By introducing region-specific reference images and machine-learning based methods for image segmentation and track filtering, we have been able to increase the number of organoids tracked approximately 15-fold from initial analyses where only approximately 1% of organoids analyzed were retained per well using standard approaches. Further improvements will include shortening the 6-hour delay between drug treatment and imaging start, which will allow us to capture highly sensitive organoids undergoing cell death within that timeframe. Lastly, due to the large amount of data generated using HSLCI (approximately 250 GB per plate/day), data analysis remains a time-limiting factor.

Despite the development of 3D cancer models with varying extents of complexity and scalability, functional screening assays have been hindered by their inability to consider the heterogeneity of tumor response. Genomic characterization of tumors has demonstrated that these malignancies are collections of evolutionarily-related subclones, rather than homogeneous populations[11,13,14,193]. This genetic diversity is one of the several factors that contributes to differential response to treatment. Endpoint assays,

such as live-dead staining or ATP-release quantification, characterize the average response to treatment. Though they may be useful for identifying drug sensitivity in majority cell populations, they fail to account for the response of resistant populations that may also be present. In the clinical setting, failure to treat the resistant populations may lead to initial response, followed by recurrence and long-term disease progression[194–196]. HSLCI allows us to non-invasively track various features of the bioprinted organoids over time, including size, motility, and mass density. Because of the ability to quantitatively measure mass changes in response to treatment, it is possible to identify and isolate responsive and resistant subpopulations of cells, which can in turn lead to better informed clinical decision making.

Methods

2D Cell Culture

MCF-7 and BT-474 breast adenocarcinoma cell lines were obtained from the American Type Culture Collection (ATCC). All cell lines were grown for a maximum of 10 passages in RPMI 1640 (Gibco 22400-089) supplemented with 10% fetal bovine serum (FBS, Gibco 16140-071) and 1% antibiotic-antimycotic (Gibco 15240-062). Both cell lines were periodically authenticated by short tandem repeat profiling using the GenePrint 10 kit (Laragen).

Manually Seeded 3D Organoids

Organoids were seeded manually according to our previously published protocols[9,10,138]. Briefly, single cells suspended in a 3:4 mixture of Mammocult (StemCell Technologies 05620) and Matrigel (Corning 354234) were deposited around the perimeter of the wells of either 24-well or 96-well plates. The cell suspension was kept on ice throughout the seeding process to prevent gelation of the Matrigel. To seed organoids in a 96-well plate (Corning 3603), a pipette was used to distribute 5 µL of cell suspension (5×10^5 cells/mL) along the bottom perimeter of each well. Once all mini-rings are generated, plates were incubated at 37°C and 5% CO_2 for 20 minutes to solidify the Matrigel, and 100 µL of pre-warmed Mammocult was added to the center of each well using an epMotion 96 liquid handler (Eppendorf). To generate larger rings (maxi-rings) in

24-well plates (Corning 3527), 70 µL of cell suspension (1.4×10^6 cells/mL) was deposited around the perimeter of each well. Following seeding, the plate was incubated at 37°C and 5% CO_2 for 45 minutes to solidify the Matrigel, and 1mL of pre-warmed Mammocult was added to the center of each well.

3D Printing Plasma Masks

Custom well masks were designed to meet the specifications of the well plates that were used in these experiments (**Figure S4.1**). The design was generated in Inventor 2020 (Autodesk) and printed using a Form3B (FormLabs) using the Biomed Amber resin (FormLabs). The design was exported as an STL file and imported into the PreForm (FormLabs) software to arrange the parts. After printing, parts were post-processed in two washes of isopropanol, air-dried for at least 30 minutes, and cured for an additional 30 minutes at 70°C in the Form Cure (FormLabs).

Bioprinted 3D Organoids

Cells were bioprinted using a CELLINK BioX with a Temperature-Controlled Printhead. Gcode files were written to print the desired single-layer geometry. MATLAB (MathWorks, Inc.) was used to integrate these standardized blocks into full Gcode files with the defined coordinates for each well. We used 8-well plates when printing the maxi-rings for IHC and RNA sequencing (RNAseq) as the depth of the well in a standard 24-well plate prohibited the use of 0.5" length needles. Four rings with a diameter of 14.5mm were printed for RNAseq ($\sim 2 \times 10^5$ cells total), while four sets of concentric 14.5mm, 12.5mm, and 10.5mm diameter rings were used for IHC analysis ($\sim 5 \times 10^5$ cells total). We printed mini-squares with side length 3.9mm for drug screening and HSLCI imaging. The mini-squares were inscribed within the circular well with sides parallel to the sides of the well plate. All bioprinting processes utilized the same material deposited for manually seeded organoids: a single-cell suspension in a 3:4 mixture of Mammocult and Matrigel on ice. After vortexing briefly, the mixture was transferred into a 3 mL syringe to remove air bubbles. The mixture was then transferred to a room temperature 3 mL bioprinter cartridge (CELLINK) by connecting the syringe and cartridge with a double-sided female

Luer lock adapter (CELLINK). The loaded cartridge was incubated in a rotating incubator (Enviro-Genie, Scientific Industries) for 30 minutes at the print temperature.

During the incubation period, the printer was sterilized with the built-in UV irradiation function, the printhead was set to the print temperature and the masked 96-well plates treated with oxygen plasma. Briefly, well masks were autoclaved prior to use, inserted into the well plate, and pressed in contact with the glass surface. Masked plates were treated with oxygen plasma in a PE-25 (Plasma Etch) for 30-90 seconds, 15 minutes prior to bioprinting. After plasma treatment, the well plate was placed in the bioprinter and Automatic Bed Levelling (ABL) was performed.

Once the incubation period ended, we attached a 0.5" 25-gauge needle and loaded the cartridge into the pre-cooled printhead. We primed the needle by extruding a small volume of material at 15 kPa prior to calibrating the printer. The material in the needle gelled during the printer calibration which takes approximately 2 minutes. After calibration, we performed a second extrusion using 40 kPa to clear the needle of the gelled material prior to starting the print, this step ensured that we achieved unobstructed material extrusion. To create constructs of the appropriate thicknesses, prints in 8-well plates were extruded at 15 kPa while prints in 96-well plates were extruded at 12-15 kPa. The bioprinter completes the deposition process for 96-well plates in approximately four minutes. After printing, the constructs were incubated at 37°C for at least 30 minutes to solidify the matrix and 100µL of Mammocult medium was then added.

Sample Preparation for RNA Sequencing

Organoids were released from the Matrigel in preparation for RNAseq. After aspirating the media from each ring, 1 mL of cold Dispase was added per ring. After a 20-minute incubation at 37°C, the cell suspension was collected and pelleted by centrifugation at 1500g for 5 minutes and washed with 45 mL of PBS before centrifuging again at 2000g for an additional 5 minutes. Once all liquid was aspirated, the tubes were rapidly frozen and stored at -80°C. Frozen cell pellets (~2×10^5 cells) were then transferred to the Technology Center for Genomics & Bioinformatics (TCGB) at UCLA for RNAseq. Sequencing was performed on a NovaSeq SP (Illumina) using the 2 x 150 bp paired-end protocol.

RNA Sequencing Data Processing and Analysis

FASTQ files were processed using UCLA-CDS pipelines to align, quantify and call RNA-sequencing reads. Pipeline-align-RNA v6.2.2 aligns paired-end, reverse stranded RNA-seq reads using STAR v2.7.6[197] and HISTA2 v2.2.1[198]. Genome reference file, CRCh38.p13, was used for aligners STAR and HISTA2. Annotations were performed using Gencode v34 reference GTF. FASTP v0.21.0[199] was included in the pipeline to trim reads for low-quality bases and remove adaptor sequences. Next, the pipeline marked duplicate reads using the GATK Spark tools[200] (MarkDuplicates Spark v4.1.4.1[200]) that allowed for parallel processing on multiple computing clusters. Lastly, the pipeline runs dupRader v1.24.0[201] to check the duplication rate.

We used pipeline-quantitate-RNA to quantify RNA at the gene and transcript isoform level. The pipeline used RSEM v1.3.3[202] to quantify RNA using GRCh38.p13 as the reference index file. RSEM quantifies aligned RNA-seq in BAM format. The output is a quantitated RNA at the RNA and transcript isoform level. Quality control procedures include running FastQC v0.11.9 on input FASTQ files to control for low quality reads that may lead to low quality mapping. Transcripts with low abundance in all samples (TPM < 0.1; transcripts per million) were excluded resulting in 27,077/67,060 transcripts included in the analysis.

Pipeline-quantitate-SpliceIsoforms was used to quantitate the relative usage of splice isoforms using aligned RNA-seq data. The pipeline validates inputs and used rMATS v4.1.0[203] on individual RNA-seq aligned data in BAM format. The output includes information on the alternative splicing event types. We excluded splice isoforms with missing data in five or more samples (8,561/17,449) due to low power.

Pipeline-call-RNAEditingSite uses REDItools2 v1.0.0[204] to call RNA editing events. Pipeline-call-FusionTranscripts calls gene fusion events using a combination of Arriba v2.1.0[205], STAR-Fusion v1.9.1[206] and fusioncatcher v1.33[207]. Arriba detects gene fusions from RNA-seq data using the STAR aligner. The STAR-Fusion caller is a component of the Trinity Cancer Transcriptome Analysis Toolkit (CTAT). Fusioncatcher calls somatic fusion genes in paired-end RNA-seq data files. RNA editing sites were filtered to include adenosine to inosine events with sufficient coverage (q30 >10) and frequencies above

0.9. Poly-A depleted RNA included annotated microRNAs (miRNA), while poly-A enriched RNA included coding mRNAs. Raw and processed data will be made available in GEO.

We used a Mann-Whitney U-test to perform non-parametric hypothesis statistical testing of RNA abundances, number of transcript fusions, and editing sites between bioprinted and manually seeded tumor organoids. We adjusted for multiple hypothesis testing using the false discovery rate (FDR) method, setting q < 0.1 as the criterion for strong associations. Statistical analyses and data visualization were performed in the R statistical environment (v4.0.2) using the BPG[208] (v6.0.1) package.

Immunohistochemistry

Immunohistochemical staining was performed on manually seeded and bioprinted organoids seeded in 24 or 8-well plates, respectively. A detailed procedure has been published[138]. Briefly, samples were prepared for histological analysis by carefully aspirating all media from the well without disrupting the construct and fixing in 10% buffered formalin (VWR 89370-094). The fixed organoids were harvested, transferred to a conical tube and pelleted by centrifugation at 2000xg for 5 minutes. HistoGel (Thermo Scientific HG-40000-012) was then added to the pellet. Once solidified, the cell pellet in HistoGel was placed in a histologic cassette and sent to the UCLA Translational Pathology Core Laboratory (TPCL) for dehydration and paraffin embedding.

Slides (8 µm thin sections) were baked for 20 minutes at 45 °C and de-paraffinized in xylene followed by washes in ethanol and deionized water. For H&E staining, a Hematoxylin and Eosin Stain Kit (Vector Labs H-3502) was used according to the manufacturer's protocol. For Ki-67/Caspase-3, HER2, and ER staining, Peroxidazed-1 (Biocare Medical PX968M) was applied for 5 minutes at room temperature to block endogenous peroxidases. Next, antigen retrieval was performed using Diva Decloaker (Biocare Medical DV2004LX) in a 2100 Retriever (Prestige Medical) heating at 110 °C for 15 minutes. Blocking was performed at room temperature for 5 minutes with Background Punisher (Biocare Medical BP947H), Primary Ki-67/Caspase-3 staining was performed overnight with pre-diluted Ki-67/Caspase-3 (Biocare Medical PPM240DSAA) solution at 4°C after an additional 2-minute Background Punisher treatment post-antigen retrieval, and secondary staining was performed with Mach 2 Double Stain 2 (Biocare) solution for

40 minutes at room temperature. Primary antibodies for HER2 (Novus Biologicals, CL0269) and ER (Abcam, E115) staining were diluted 1:100 in Da Vinci Green Diluent (Biocare Medical PD900L). The HER2 antibody was incubated overnight at 4°C while the ER antibody was incubated at room temperature for 30 minutes. Secondary staining was performed with Mach 3 Mouse Probe and Mach 3 Mouse HRP-Polymer for HER2 and Mach 3 Rabbit Probe and Mach 3 Rabbit HRP-Polymer for ER (10 minutes). Chromogen development was performed with Betazoid DAB (Biocare Medical, BDB2004) followed by counterstaining with 20% hematoxylin (Thermo Scientific #7221). Slides were dehydrated in ethanol and xylene and coverslipped with Permount (Fisher Scientific SP15-100). Imaging was performed with a Revolve microscope (Echo Laboratories). Whole image white balancing was performed in Adobe Photoshop.

Drug Screening

A detailed protocol for the drug screening has been published previously[9,138]. Briefly, the culture medium was fully removed three days after seeding and replaced with 100 µL of Mammocult medium containing the indicated drug treatments using a liquid handler (EpMotion® 96). After treatment, we transferred the plates to the HSLCI platform for imaging.

High-Speed Live Cell Interferometry

HSLCI has been described previously[144,145]. The HSLCI platform is a custom-built inverted optical microscope coupled to an off-axis quadriwave lateral shearing interferometry (QWLSI) camera (SID4BIO, Phasics, Inc.)[147]. This wavefront sensing camera incorporates a modified Hartmann mask that splits the incident wave front into four tilted replica wavefronts that interfere with one another. The resulting interferograms are recorded and used to recover phase gradients along two perpendicular directions, allowing for reconstruction of a phase shift map and subsequent calculation of dry mass of discrete objects within imaging fields of view (FOVs)[147,150]. Illumination is provided by a 660 nm fiber-coupled LED (Thorlabs). The HSLCI platform captures images from standard-footprint (128×85 mm) glass-bottom multiwell plates. Motorized stages (Thorlabs) control the XY-motion of a single glass-bottom plate above the microscope

objective, and in combination with a piezo-actuated dynamic focus stabilization system, enable continuous and repeated image collection over many FOVs within each row of wells. The HSLCI platform is installed inside of a standard cell culture incubator to enable long-term imaging of samples in physiology-approximating conditions (37°C, 5% CO2). All hardware and software components are available commercially.

For all growth kinetics and drug screening studies, organoids were imaged in 96-well glass-bottom plates (Cellvis P96-1.5H-N) using a 40× objective (Nikon, NA 0.75). Plates were prepared as described and wrapped with parafilm to limit evaporation during imaging. Organoids were imaged continuously from 6 hours to 72 hours following administration of drug treatments. During imaging, the sample plate was translated along each row of wells such that about 25 images per well were collected on each imaging loop, and that imaging FOVs overlapped with areas of wells in which bioprinted matrix and organoids were present. The typical imaging interval was 10 minutes between successive frames at the same FOV.

Machine Learning-Based Analysis of HSLCI Images

Images were acquired using the SID4Bio software (v2.4.2.93, Phasics). After image collection, interferograms captured by the QWLSI camera were converted to phase shift images using the SID4 software development kit for MATLAB (GPU version, v741, Phasics), in a process called phase unwrapping. For every frame at each FOV, phase shift maps were processed by converting to optical path difference[147], and then subtracting the fourth-order Zernike polynomial[209] fit to each frame using least-squares over a cartesian grid to remove refractive aberrations.

The processed images were then segmented into individual cells or organoids using a convolutional neural network (U-Net architecture[104] with a ResNet-34 encoder[10,123]). We initialized our model with weights derived from a model pretrained on the ImageNet dataset[124]. The training dataset consisted of a randomly selected set of 50 images from the BT-474 dataset, and 50 from the MCF-7 dataset encompassing images taken at all wells, intra-well imaging positions, and timepoints within each experiment. Each 514x514 pixel image was overlaid with a binary mask that marks each pixel as either part of an organoid or the background. Using the training dataset, the weights were

refined using a cross-entropy loss function over 80 epochs. We organized phase images and their corresponding masks into one stack per imaging FOV and sorted each layer by time of imaging. We used TrackMate (v7.6.1)[173,174] to track the organoids over time using a Sparse LAP Tracker with a maximum linking distance of 90 pixels and feature penalties of 4.0 for both the major ellipse axis and organoid area. These parameters were selected based on optimal performance on a set of 12 representative image stacks. We tolerated gaps of up to 30 frames to maximize track continuity between organoids. Tracks composed of fewer than 10 frames were excluded. Labeled image stacks were exported and mass was extracted from the segmented regions by integrating the phase shift over the area and multiplying by the refractive increment of 1.8×10^{-3} m^3/kg [146,151,153,154,172].

We developed an XGBoost-based classifier (v1.5.2.1, probability prediction type, log-loss evaluation metric)[175] to predict permissibility of organoid tracks using R package mlr3 (v0.13.2). For the supervised learning model, we labelled a subset of tracks for permissibility (n = 846) from four wells: 1) BT-474 well treated with vehicle, 2) BT-474 well treated with 10 µM staurosporine, 3) MCF-7 well treated with vehicle, and 4) MCF-7 well treated with 10 µM staurosporine and manually determined that n = 250/846 tracks were acceptable for downstream analysis. We extracted a set of time-series based features from the mass reconstruction data to use in our classifier model. The features were number of missing frames, initial size, interquartile range (IQR), IQR of the first 12 points, and IQR of the last 12 points. Initial size was calculated based on the median mass of the first two timepoints (**Figure S4.2**). Area under the curve (AUC) measurements were calculated using R package (bayestestR v0.11.5). Pair-wise correlation plots comparing the void and valid track features were generated using mlr3viz R package (v0.5.7). We used probability as the learner prediction type and log-loss ($\log_{10}$) as the evaluation metric. To validate the model, we performed k-fold cross-validation protocols with 3-fold resampling. The classifier predicted n = 8,590/29,137 to be permissible organoid tracks for downstream analysis with an accuracy of 93.5% and a cross-validation score of 91%.

ATP release assay

Manually seeded organoids were prepared in accordance with the protocol described above and published[9,10,138]. To assess the viability of bioprinted organoids, we

prepared the bioink and bioprinter as described. We extruded 100 μL of bioink into and Eppendorf tube for each print pressure (10, 15, 20, and 25 kPa). We seeded four 10 μL rings in a 96-well plate using the extruded bioink. For drug screenings, plates were retrieved from the HSLCI incubator and processed as briefly described. After a PBS wash, 50 μL of 5 mg/mL Dispase (Life Technologies 17105-041) solution was added to each well and incubated for 25 minutes. After shaking for 5 minutes on an orbital shaker at 800 RPM, we added 75 μL of CellTiter-Glo® Luminescent Cell Viability Reagent (Promega G968B) to each well and followed the manufacturer's instructions. Luminescence was measured using a SpectraMax iD3 (Molecular Devices) plate reader (parameters: read all wavelengths, signal integration of 500ms). The viability of each well was calculated by normalizing the luminescent signal to the average signal from the manually seeded control wells. An unpaired t-test with Welch's correction was performed in GraphPad Prism. P-values less than 0.05 were deemed significant.

A

B

C
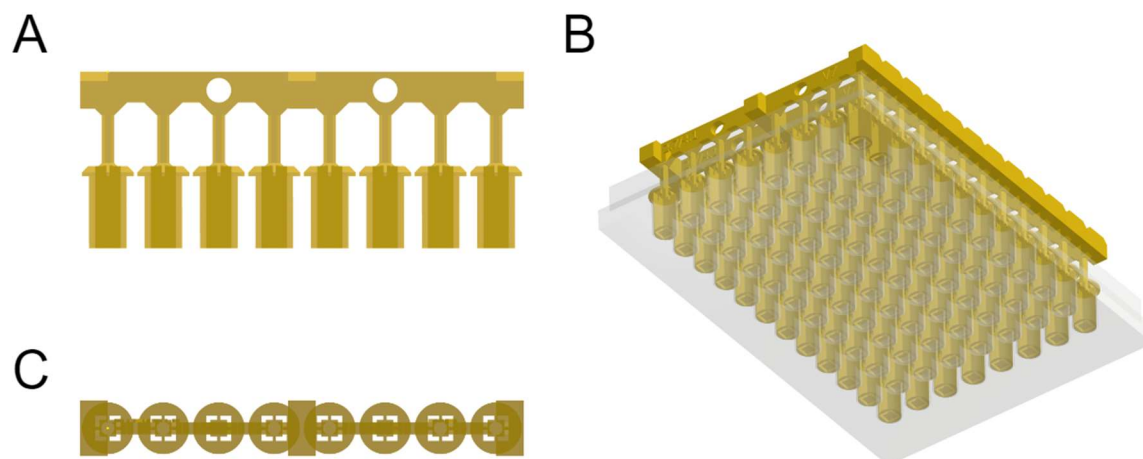
Figure S4.1: Schematics of well mask. (A) Side view. **(B)** Bottom view. **(C)** Plasma masks inserted into 96-well plate viewed from bottom.
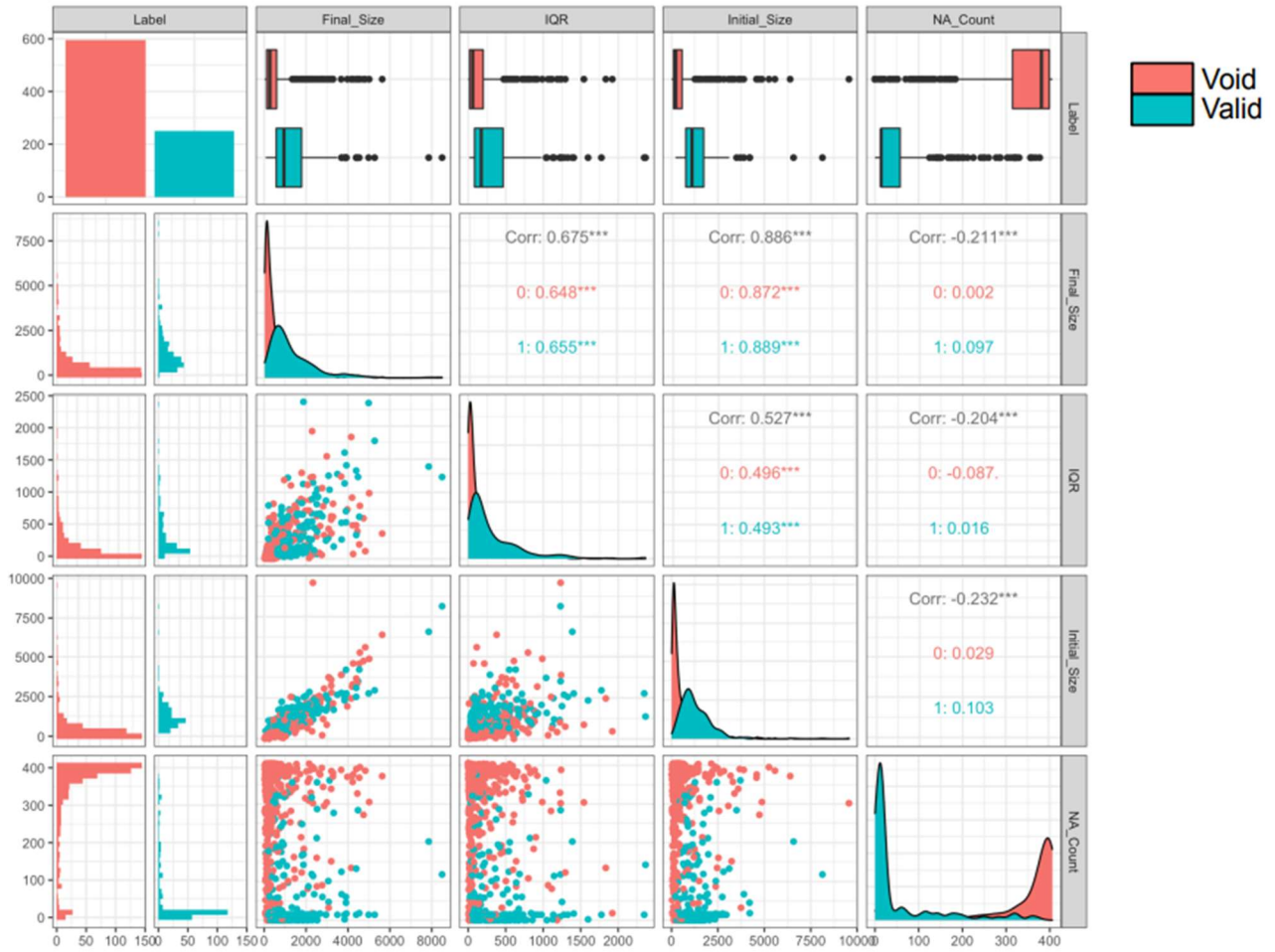
Figure S4.2: Pair-wise correlation matrix of classifier data. Extracted time-series analytical features of tumor growth patterns over recorded time. The number of missing frame (NA count), initial size, final size and interquartile range (IQR) was measured for each tracked tumor organoid. We labelled (n = 250 out of 846) tracked organoids as valid for downstream analysis. Pair-wise correlations are shown of the valid (label = 1) and void (label = 0) tracked organoids. Void tracks showed an increased number of missing frames and smaller IQR, initial and final size. Correlation of the classification data are shown within the paired subplots. Initial and final size were strongly correlated (R^2 = 0.89). An XGBoost classifier was used to train a model to classify organoids as valid or void. We validated the model via cross-validation with 3-fold resampling of the sample population. The cross-validation score of the classifier was 91% with 93.5% accuracy.
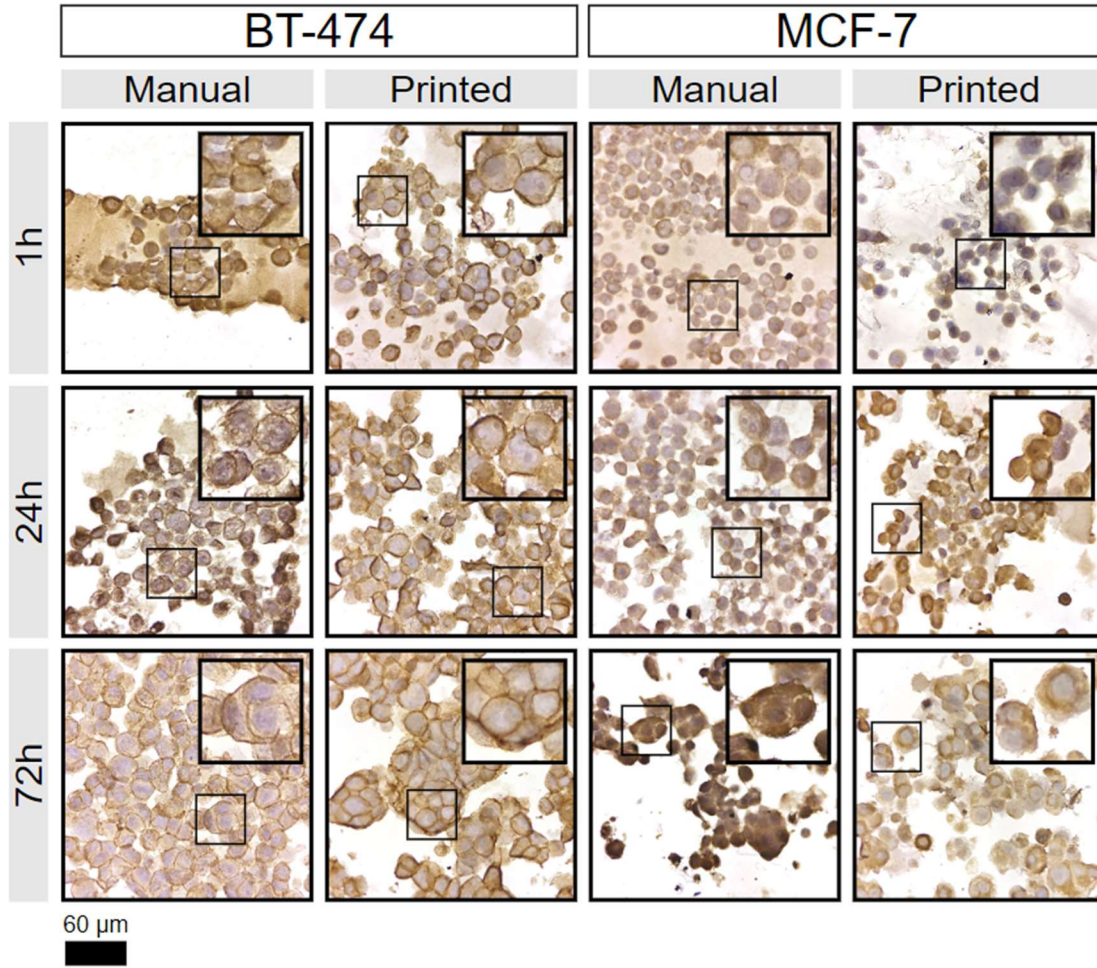
Figure S4.3: HER2 expression in BT-474 and MCF-7 organoids. Immunohistochemistry staining of 3D cultures for HER2. BT-474 cells have amplified HER2 expression[164,167] while MCF-7 cells express lower levels of HER2 and lack HER2 amplification[164–166].
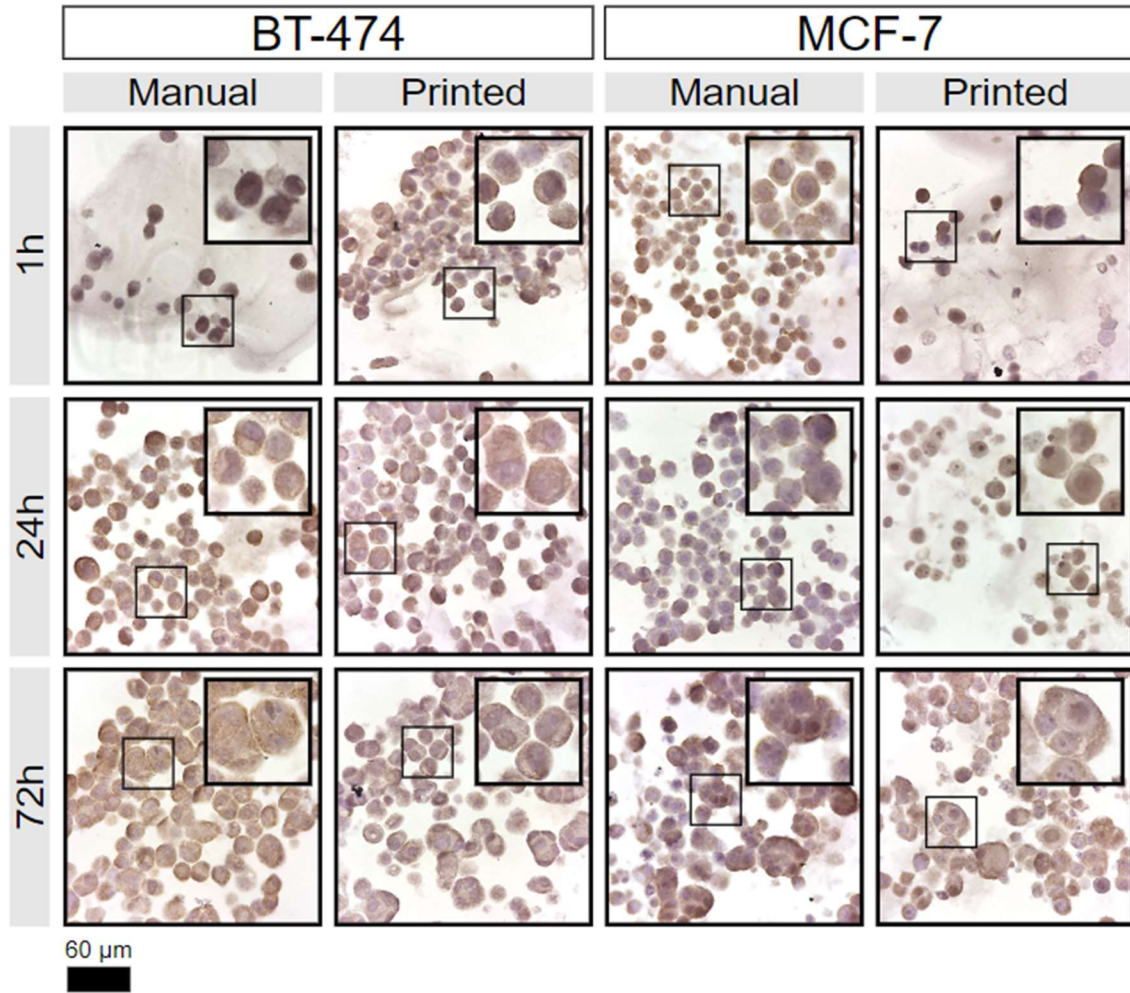
Figure S4.4: Estrogen Receptor Expression in BT-474 and MCF-7 organoids. Immunohistochemistry staining of 3D cultures for ER. Both BT-474 and MCF-7 cell lines are ER-positive[164–167].
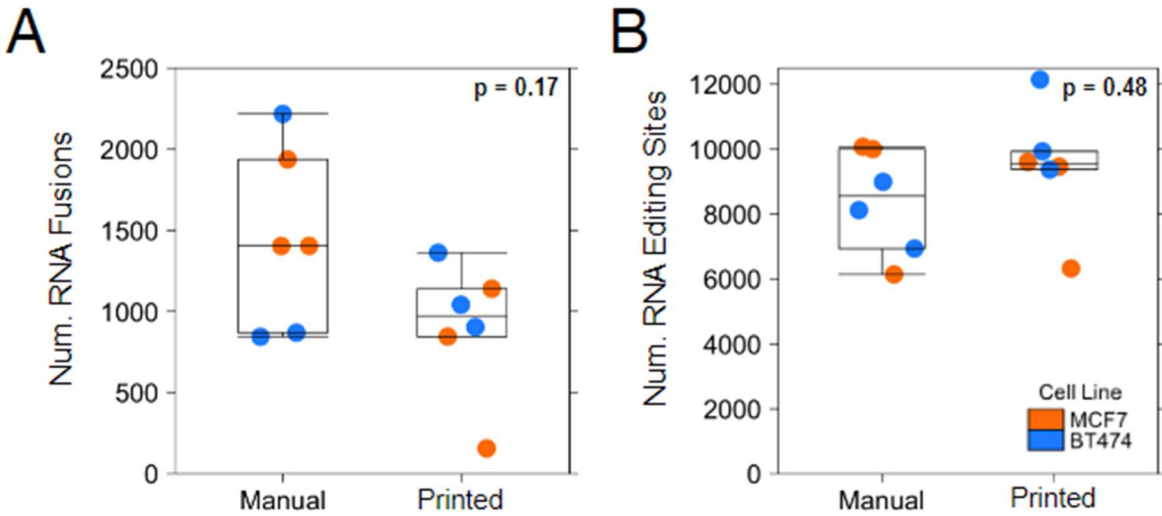
Figure S4.5: RNA Fusions and Editing Sites. (A) Number of RNA fusions detected by FusionCatcher by tumor organoid seeding method. The number of RNA fusions did not significantly differ between manually seeded and bioprinted organoids (p_{BT-474} = 0.179, p_{MCF-7} = 0.179). **(B)** The number of adenosine-to-inosine (A-to-I) RNA editing sites detected by REDItools were not associated with tumor organoid development method (p = 0.48, Mann-Whitney U-test). By cell line, the number of A-to-I RNA editing sites did not differ between printed and manually seeded organoids (p_{BT-474} = 0.1, p_{MCF-7} = 0.7).
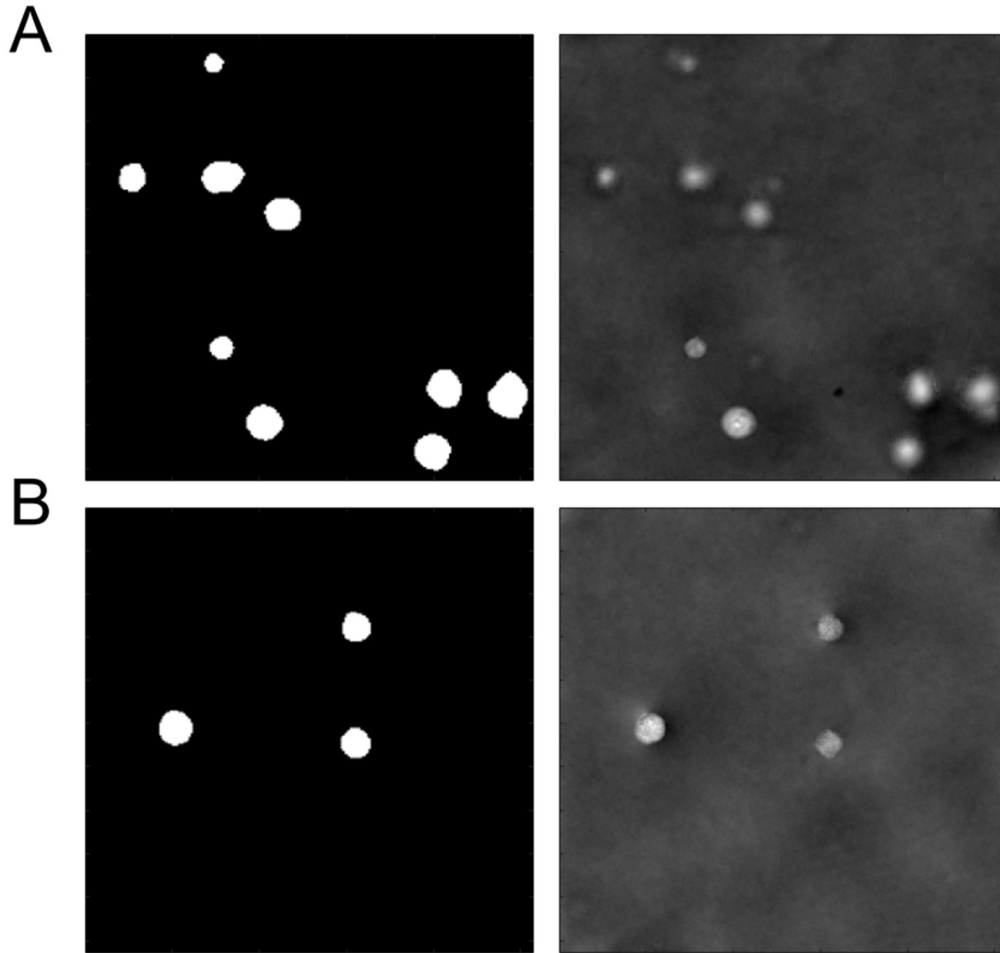
Figure S4.6: Image segmentation using a U-Net convolutional neural network. Representative masks (left) predicted by the U-Net-based segmentation algorithm for the background-corrected phase images (right).
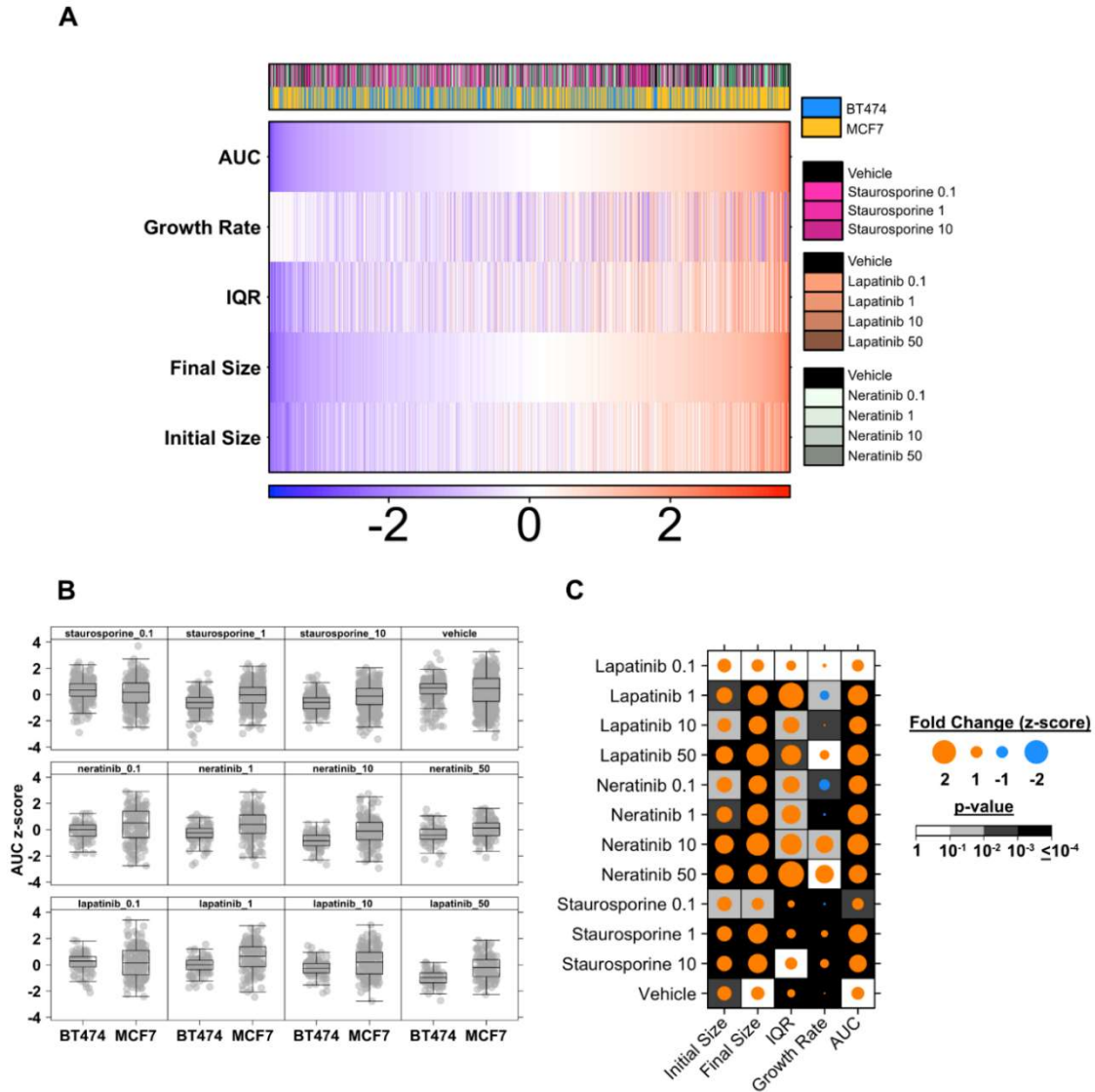
Figure S4.7: Growth patterns of MCF-7- and BT-474-derived tumor organoids among pharmacological treatments. We assessed the growth patterns of tumor organoids derived from MCF-7 and BT-474 breast cancer cell lines. Tumor organoids of both cell line types were grown in various pharmacological concentrations of lapatinib, neratinib and staurosporine ranging from 0.1 to 10 μM. **(A)** Growth patterns of tumor organoids are arranged by area under the curve (AUC) metric measured by the integration of a fitted time-series step function. Z-transformed measurements of organoid AUC, linear growth pattern (R^2 of a linear fit), initial size, final size and interquartile range (IQR) varied among sample population. **(B)** Overall growth patterns, measured as AUC, of MCF-7- and BT-474-derived organoids differed among each pharmacological treatment condition. **(C)** Fold change of growth patterns features were found to be significantly different among MCF-7 and BT-474 derived organoids in all three well treatment condition under various concentrations.
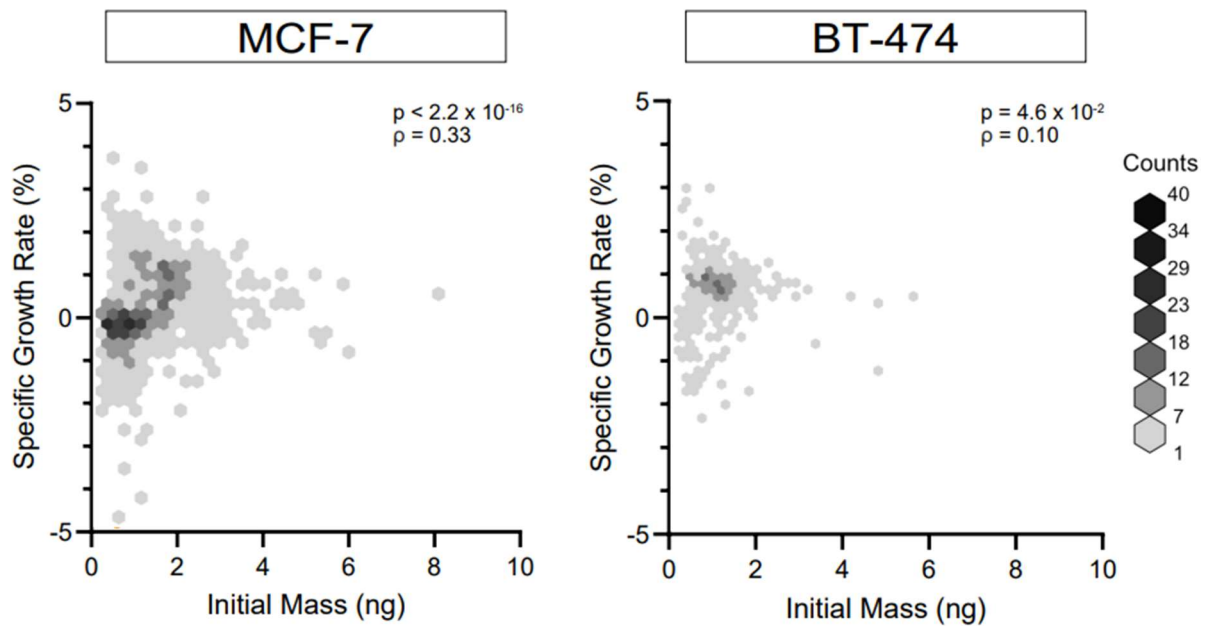
Figure S4.8: Specific growth rate correlates to initial organoid mass. Specific growth rate (growth in mass as a percentage of total mass) versus initial organoid mass was plotted for all organoids tracked. For both cell lines, we observe a positive relationship between initial organoid mass and specific growth rate. The association is stronger for MCF-7 organoids (Spearman's $\rho = 0.33$, $p < 2.2 \times 10^{-16}$) compared to BT-474 organoids ($\rho = 0.10$, $p = 4.6 \times 10^{-2}$).
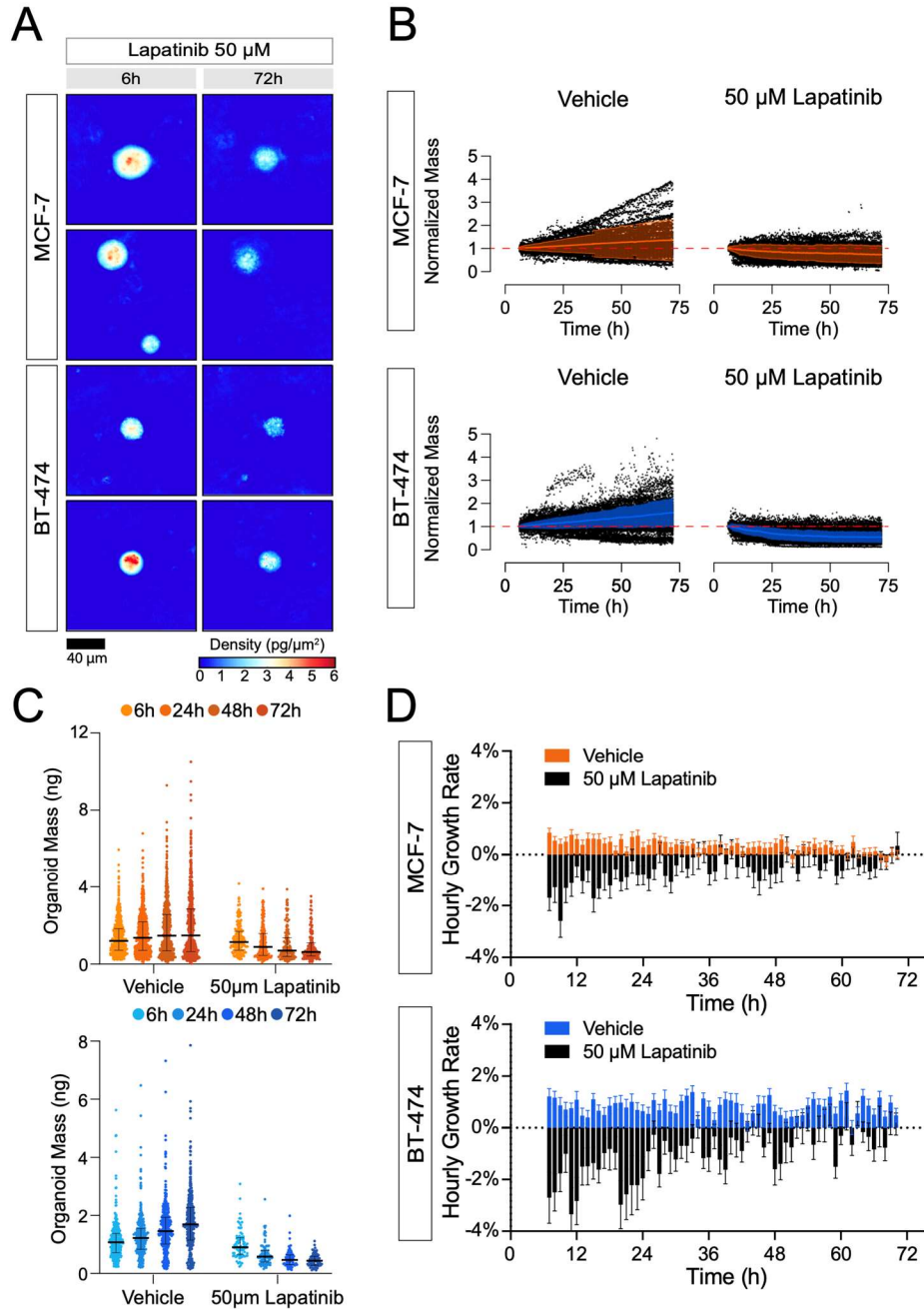
Figure S4.9: Response of bioprinted organoids to 50 μM lapatinib. (A) Representative images of organoids treated with 50 μM lapatinib. **(B)** 100 organoid tracks are shown on each plot. The mean normalized mass ± standard deviation is also shown in orange (MCF-7) and blue (BT-474). **(C)** Mass distribution of tracked MCF-7 and BT-474 organoids by treatment. Each column represents the mass distribution at 6-, 24-, 28-, and 72-hours post-treatment (left to right). Black horizontal bars represent the median with error bars representing the interquartile range of the distribution. **(D)** Hourly growth rate comparisons (percent mass change) between organoids treated with 50 μM lapatinib and vehicle.
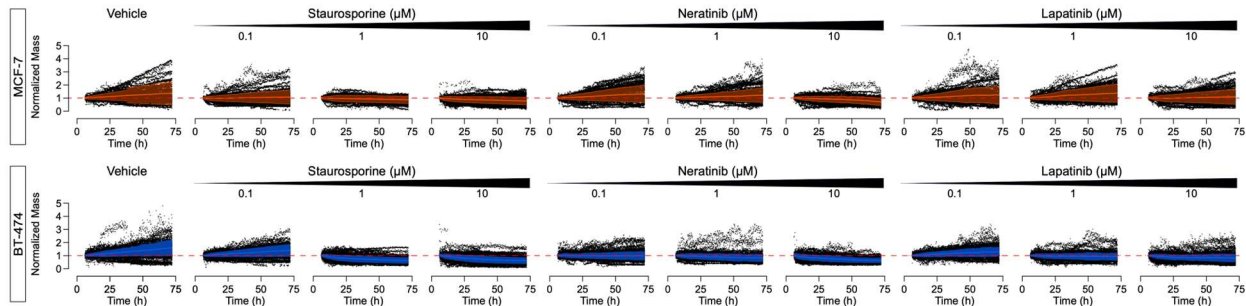
Figure S4.10: Representative normalized mass tracks by treatment condition. 100 organoid tracks for each treatment condition are shown on each plot. The mean normalized mass ± standard deviation is also shown in orange (MCF-7) and blue (BT-474).
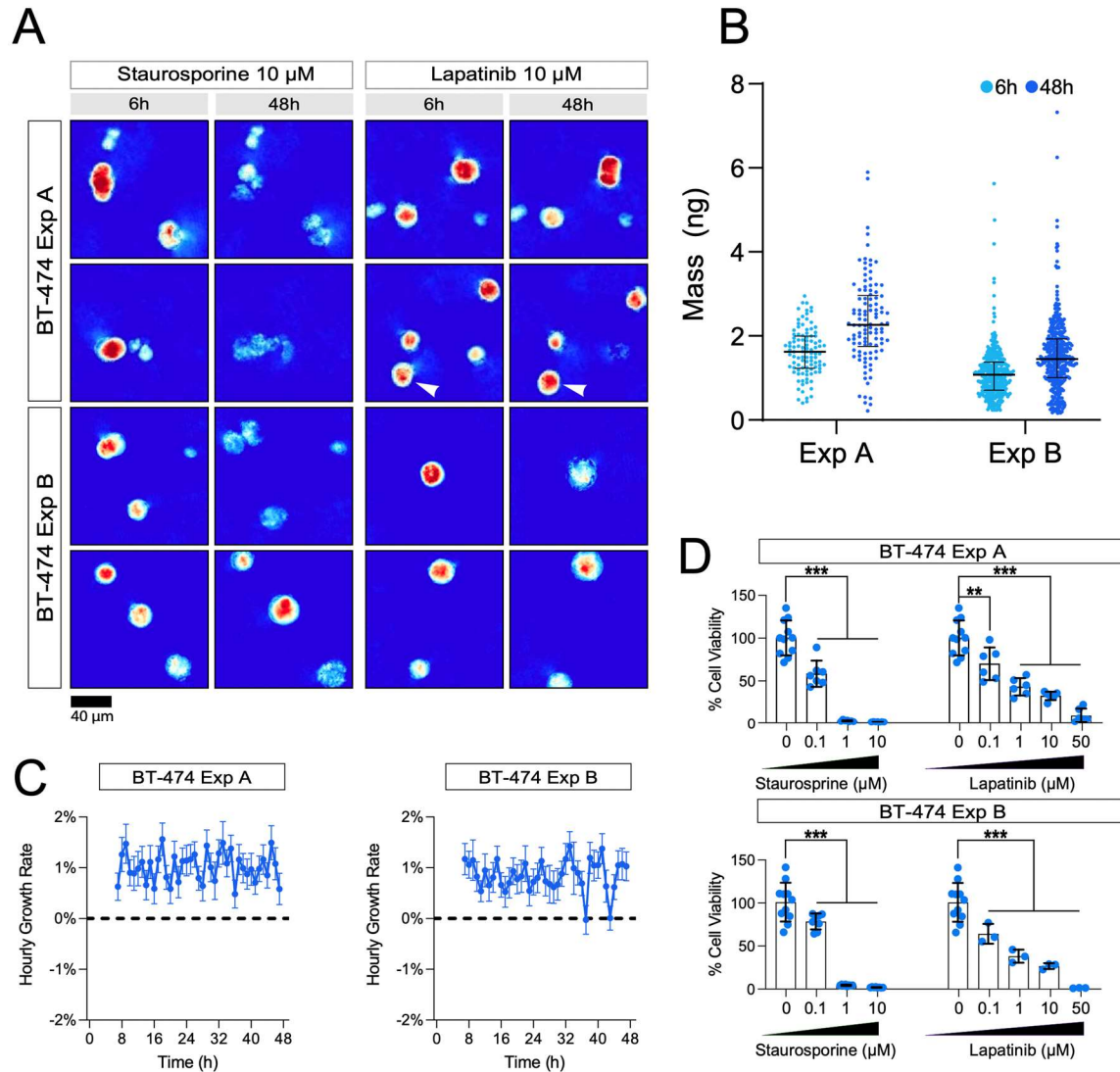
Figure S4.11: Comparison of BT-474 organoid datasets. Experiment A and B followed the same protocols with three exceptions. Experiment A was only imaged with the HSLCI for 48h hours after treatment, while Experiment B was imaged for 72 hours. Experiment A did not include neratinib in the drug screen. Experiment A was analyzed using our legacy pipeline as described in our original pre-print, while Experiment B was analyzed using the machine-learning based pipeline. **(A)** Representative images of organoids treated with 10 μM staurosporine and 10 μM lapatinib. **(B)** Mass distribution of tracked BT-474 organoids by treatment. The left column (pale blue) represents the mass distribution 6 hours post-treatment, while the right column (dark blue) represents the organoids 48 hours after treatment. Black horizontal bars represent the median with error bars representing the interquartile range of the distribution. **(C)** Hourly growth rate comparisons (percent mass change) between organoids treated with 50 μM lapatinib and vehicle. **(D)** Percent cell viability of treated wells determined by an ATP-release assay. $p<0.05$ is denoted by *, $p<0.01$ is denoted by **, and $p<0.001$ is denoted by ***.

Supplementary Results

<u>Mass reconstruction data extracted for classifier</u>

Mass reconstruction data of (n = 8,590) tumor organoid tracks derived from BT-474 and MCF-7 breast cancer cell lines were assessed for change in tumor size over 72 hours following treatment. Each cell line was treated with a series of concentrations of 0.1 to 50 µM of vehicle (n = 1,593), lapatinib (n = 1,650), neratinib (n = 1,626) and staurosporine (n = 2,920). We assessed the organoid growth patterns using z-transformed measurements of area under the curve (AUC), linear growth rate, interquartile range, initial and final size (Supplementary Figure 8A). Sample population of tumor organoids from BT-474 and MCF-7 under various pharmacological treatments display a diverse set of growth patterns, arranged by AUC metric. Cell line and treatment type were dispersed across the sample population, thus supporting our decision to use a single set of classifier training data for both cell lines and all treatment conditions. We tested whether tumor organoids derived from BT-474 displayed differences in their growth patterns compared to organoids derived from MCF-7 (Supplementary Figure 8B). We found significant differences in growth patterns of BT-474 and MCF-7 derived organoids across treatments (Supplementary Figure 9C). In most conditions (10 out of 12 conditions), the initial size, final size and linear growth rate of MCF-7 derived organoids were larger than BT-474 organoids in all three pharmacological treatment conditions (Supplementary Figure 9B-C) ($p < 0.0001$, Mann-Whitney U-test). In two conditions, the linear growth rate of BT-474 derived organoids in 1 µM lapatinib (fold change = -0.70, $p = 2.76 \times 10^{-2}$) and 0.1 µM neratinib (fold change = -0.82, $p = 3.82 \times 10^{-3}$) were found to be greater than MCF-7 derived organoids. We did not find strong differences in growth patterns among BT-474 and MCF-7 derived tumor organoids in 0.1 µM lapatinib treated wells.

A

MCF-7		6 hours	24 hours		48 hours		72 hours	
		Mean mass ± SD	Mean mass ± SD	p-value	Mean mass ± SD	p-value	Mean mass ± SD	p-value
Vehicle	1% DMSO	1.36 ± 0.84	1.56 ± 1.05	-	1.77 ± 1.33	-	1.95 ± 1.61	-
Staurosporine	0.1 µM	1.30 ± 0.84	1.27 ± 0.89	2.11×10^{-5}	1.39 ± 1.07	1.31×10^{-5}	1.44 ± 1.21	2.49×10^{-6}
	1 µM	1.28 ± 0.84	1.18 ± 0.77	1.93×10^{-9}	1.10 ± 0.73	2.24×10^{-17}	1.03 ± 0.70	2.80×10^{-21}
	10 µM	1.30 ± 0.78	1.11 ± 0.69	1.49×10^{-13}	1.01 ± 0.65	6.73×10^{-24}	0.93 ± 0.64	3.24×10^{-30}
Neratinib	0.1 µM	1.47 ± 1.03	1.62 ± 1.18	1	1.86 ± 1.51	1	2.03 ± 1.74	1
	1 µM	1.45 ± 0.96	1.57 ± 1.09	1	1.68 ± 1.22	1	1.79 ± 1.40	1
	10 µM	1.39 ± 1.07	1.30 ± 0.98	0.0036	1.16 ± 0.92	2.90×10^{-9}	0.92 ± 0.77	6.82×10^{-19}
Lapatinib	0.1 µM	1.38 ± 1.03	1.49 ± 1.19	0.9072	1.73 ± 1.47	1	1.79 ± 1.56	1
	1 µM	1.40 ± 0.83	1.61 ± 1.11	1	1.84 ± 1.38	1	2.02 ± 1.69	1
	10 µM	1.29 ± 0.83	1.30 ± 0.98	0.0011	1.42 ± 1.11	0.0013	1.50 ± 1.29	0.0006
Kruskal-Wallis p-value		0.3169	2.21×10^{-22}		4.57×10^{-45}		5.13×10^{-60}	

B

BT-474		6 hours		24 hours		48 hours		72 hours	
		Mean mass ± SD	p-value	Mean mass ± SD	p-value	Mean mass ± SD	p-value	Mean mass ± SD	p-value
Vehicle	1% DMSO	1.12 ± 0.61	-	1.27 ± 0.69	-	1.52 ± 0.84	-	1.77 ± 1.00	-
Staurosporine	0.1 µM	1.10 ± 0.57	1	1.22 ± 0.67	1	1.39 ± 0.82	0.0756	1.56 ± 0.96	0.0093
	1 µM	1.02 ± 0.53	0.0901	0.76 ± 0.39	2.27×10^{-32}	0.63 ± 0.34	1.28×10^{-57}	0.57 ± 0.32	3.03×10^{-62}
	10 µM	1.02 ± 0.51	0.1342	0.79 ± 0.44	1.59×10^{-28}	0.63 ± 0.36	4.55×10^{-56}	0.56 ± 0.32	2.52×10^{-62}
Neratinib	0.1 µM	1.04 ± 0.46	1	0.97 ± 0.44	4.86×10^{-6}	0.97 ± 0.45	5.09×10^{-14}	0.98 ± 0.46	6.93×10^{-18}
	1 µM	1.08 ± 0.54	1	0.98 ± 0.49	4.34×10^{-7}	0.86 ± 0.40	1.19×10^{-20}	0.81 ± 0.36	1.48×10^{-27}
	10 µM	0.92 ± 0.42	0.0043	0.70 ± 0.31	3.73×10^{-21}	0.59 ± 0.28	1.99×10^{-31}	0.53 ± 0.21	4.71×10^{-34}
Lapatinib	0.1 µM	1.05 ± 0.52	1	1.13 ± 0.57	0.2512	1.23 ± 0.61	0.0025	1.31 ± 0.67	1.83×10^{-5}
	1 µM	1.08 ± 0.54	1	1.00 ± 0.49	3.37×10^{-5}	0.96 ± 0.45	1.80×10^{-14}	0.93 ± 0.43	1.70×10^{-21}
	10 µM	1.09 ± 0.47	1	0.91 ± 0.45	7.72×10^{-10}	0.86 ± 0.40	3.31×10^{-20}	0.83 ± 0.41	2.13×10^{-24}
Kruskal-Wallis p-value		0.0007		4.25×10^{-70}		1.38×10^{-141}		7.68×10^{-168}	

Table S4.1: Organoid mass distributions. (A) Comparisons of mean mass of MCF-7 organoids calculated via HSLCI. We first performed a Kruskal-Wallis test to determine if one sample stochastically dominates another. If the p-value was less than 0.05, we then performed Mann-Whitney U-tests for each sample against the vehicle control at the respective time point. Data is presented in Figure 4.3B. **(B)** Comparisons of mean mass of BT-474 organoids calculated via HSLCI. We first performed a Kruskal-Wallis test to determine if one sample stochastically dominates another. If the p-value was less than 0.05, we then performed Mann-Whitney U-tests for each sample against the vehicle control at the respective time point. Data is presented in Figure 4.3C.

A

MCF-7		Time (h)	n	Organoid Behavior (%)		
				Gained Mass	Stable	Lost Mass
Vehicle	1% DMSO	12	800	23.2	67.4	9.4
		24	794	44.8	36.0	19.1
		48	764	48.6	24.1	27.4
		72	715	50.8	16.6	32.6
Staurosporine	0.1 µM	12	481	8.7	72.3	18.9
		24	481	21.8	46.8	31.4
		48	458	31.7	27.3	41.0
		72	436	32.8	20.4	46.8
	1 µM	12	508	10.2	74.6	15.2
		24	505	11.7	56.6	31.7
		48	490	13.7	36.9	49.4
		72	460	10.0	31.3	58.7
	10 µM	12	539	6.9	64.7	28.4
		24	538	8.4	40.3	51.3
		48	523	9.0	22.9	68.1
		72	494	8.3	16.2	75.5
Neratinib	0.1 µM	12	205	19.5	67.3	13.2
		24	206	43.7	38.8	17.5
		48	196	49.5	27.0	23.5
		72	184	49.5	21.7	28.8
	1 µM	12	222	18.0	71.6	10.4
		24	221	37.6	45.2	17.2
		48	214	44.4	30.8	24.8
		72	203	46.3	24.6	29.1
	10 µM	12	223	14.3	68.6	17.0
		24	219	12.8	51.1	36.1
		48	213	8.0	34.3	57.7
		72	199	4.5	18.1	77.4
Lapatinib	0.1 µM	12	218	21.1	66.5	12.4
		24	214	35.5	43.5	21.0
		48	203	42.9	24.6	32.5
		72	187	43.3	22.5	34.2
	1 µM	12	202	17.8	69.8	12.4
		24	202	47.5	33.2	19.3
		48	190	55.3	21.1	23.7
		72	177	53.7	21.5	24.9
	10 µM	12	251	15.5	62.5	21.9
		24	252	32.5	31.0	36.5
		48	238	36.1	18.9	45.0
		72	220	37.7	10.0	52.3

B

BT-474		Time (h)	n	Organoid Behavior (%)		
				Gained Mass	Stable	Lost Mass
Vehicle	1% DMSO	12	419	30.1	59.9	10.0
		24	415	62.4	26.7	10.8
		48	409	80.9	10.8	8.3
		72	387	80.9	7.2	11.9
Staurosporine	0.1 µM	12	335	31.0	55.2	13.7
		24	334	49.7	38.3	12.0
		48	334	65.9	17.7	16.5
		72	327	72.8	11.0	16.2
	1 µM	12	277	11.9	39.0	49.1
		24	276	10.9	19.9	69.2
		48	275	5.5	12.0	82.5
		72	266	2.6	9.4	88.0
	10 µM	12	276	11.6	47.5	40.9
		24	273	12.1	24.9	63.0
		48	273	6.6	13.9	79.5
		72	266	4.5	7.9	87.6
Neratinib	0.1 µM	12	121	14.9	57.0	28.1
		24	120	15.0	40.8	44.2
		48	121	20.7	34.7	44.6
		72	116	28.4	22.4	49.1
	1 µM	12	132	12.9	56.8	30.3
		24	131	15.3	37.4	47.3
		48	131	10.7	22.1	67.2
		72	128	7.0	22.7	70.3
	10 µM	12	103	12.6	42.7	44.7
		24	106	8.5	30.2	61.3
		48	105	4.8	8.6	86.7
		72	103	0.0	7.8	92.2
Lapatinib	0.1 µM	12	125	22.4	64.8	12.8
		24	126	42.1	45.2	12.7
		48	124	66.9	19.4	13.7
		72	117	69.2	17.9	12.8
	1 µM	12	126	12.7	65.1	22.2
		24	126	18.3	39.7	42.1
		48	125	18.4	29.6	52.0
		72	126	18.3	25.4	56.3
	10 µM	12	122	11.5	57.4	31.1
		24	122	9.8	27.0	63.1
		48	118	11.9	17.8	70.3
		72	114	11.4	14.9	73.7

Table S4.2: Proportions of organoids that gained, lost, and maintained mass by treatment condition. (A) Proportions of MCF-7 organoids. **(B)** Proportions of BT-474 organoids. Data is plotted in Figure 5A.

		MCF-7		BT-474	
		Viability ± SD	p-value	Viability ± SD	p-value
Vehicle	1% DMSO	1.00 ± 0.22		1.00 ± 0.22	
Staurosporine	0.1 µM	0.50 ± 0.08	<0.0001	0.78 ± 0.09	0.0006
	1 µM	0.17 ± 0.04	<0.0001	0.04 ± 0.01	<0.0001
	10 µM	0.13 ± 0.04	<0.0001	0.01 ± 0.00	<0.0001
Neratinib	0.1 µM	1.02 ± 0.15	0.8463	0.40 ± 0.10	<0.0001
	1 µM	0.92 ± 0.12	0.4623	0.25 ± 0.04	<0.0001
	10 µM	0.08 ± 0.01	<0.0001	0.13 ± 0.05	<0.0001
Lapatinib	0.1 µM	1.00 ± 0.04	0.9452	0.64 ± 0.11	0.0004
	1 µM	1.01 ± 0.05	0.8598	0.38 ± 0.08	<0.0001
	10 µM	0.66 ± 0.08	0.0018	0.26 ± 0.03	<0.0001
	50 µM	0.14 ± 0.04	<0.0001	0.01 ± 0.00	<0.0001

Table S4.3: Organoid viability analysis by endpoint ATP assay. Comparisons of cell viability measured by ATP assay. P-values calculated by unpaired t-test with Welch's correction. Data is presented in Figure 5B.

Video S4.1: MCF-7 organoids treated with the vehicle control. Scan the QR code to access the video or visualize at the following link: https://youtu.be/bUBq-ZChFM0

Video S4.2: BT-474 organoids treated with the vehicle control. Scan the QR code to access the video or visualize at the following link: https://youtu.be/AzSc8WW5KBA

Acknowledgements

Chapter 5: Beyond traditional drug panels: screening alternative treatment modalities

One of the key limitations to the drug screening methodologies described in the previous chapters is the type of therapies that can be studied. For instance, drugs that have an indirect mechanism of action against tumors, such as prodrugs, stromal cell targeting compounds, and immunotherapies, require modified models to yield useful information. We have focused on developing a high-throughput system for screening clinically used prodrugs on sarcoma organoids to provide a wholistic picture of organoid drug response. Another existing challenge in the field is the assessment of non-systemic therapies such as radiation. The investigation of radiotherapy requires the development of new treatment protocols and accompanying analytical methods to identify response. By building platforms for the investigation of prodrugs and radiotherapy, we provide a more comprehensive view of the functional outcomes of the available treatment options for patients with cancer.

Investigating prodrugs with organoids

Introduction

Several therapies are delivered as prodrugs, requiring chemical modification to become active anti-tumor compounds[210]. These molecules are particularly difficult to study *in vitro* or *ex vivo* as many are metabolized in the liver by a family of Cytochrome P450 enzymes, oxygenases responsible for the degradation of compounds for clearance[211]. A considerable amount of these metabolites cannot be synthesized *in vitro* due to their instability and reactivity[212]. Even those that can be produced are susceptible to deactivation by undesirable side reactions, and can precipitate in solution[213]. The existing methods for reproducing drug metabolism *in vitro* include Transwell assays, custom-designed bioreactors, and even microfluidic devices[214–216]; however, these

systems rarely have the scalability required for high-throughput screening. Additionally, the current gold standard for studying drug metabolism is the use of mouse models that are time and resource intensive making them less than ideal candidates for high-throughput assays. By developing an *ex vivo* system to metabolize therapeutics, we can circumvent the need to test liver-metabolized drugs in low-throughput *in vitro* systems and PDX models.

We are working to develop a platform that permits screening of drugs such as ifosfamide, cyclophosphamide, irinotecan, and imatinib. Each of these is currently a part of the guidelines for the clinical management of bone cancer as described by the National Comprehensive Cancer Network®[1,217]. Ifosfamide, cyclophosphamide, and irinotecan are part of first- and second-line therapies for osteosarcoma and Ewing sarcoma, while imatinib is one of the few drugs recommended for the treatment of chordomas. The ability to screen these drugs both alone and in combination therapies will better inform clinicians on their efficacy for individual patients. We elected to pursue a co-culture model that incorporates hepatocytes within our current screening platform so prodrugs can be metabolized and exert their cytotoxic effects within the same well.

Results

Development of a novel tumor-liver co-culture system compatible with laboratory automation

We set to develop an automation-compatible system for co-culturing tumor and hepatic organoids. To meet this need, we developed the miniature liver insert (MLI), a custom-designed 3D printed well insert, capable of introducing a 3D organoid culture in a mini-ring and automation-compatible format (**Figure 5.1A**). Unlike Transwell inserts, the MLI leaves the center of the well accessible by fluid handlers for media changes and the addition of treatments (**Figure 5.1B**). The MLI is portable and automation compatible as it can be easily added or removed to wells of interest. The low profile of the rim ensures that the MLI does not interfere with the lid of the well plate. We use a commercially available 3D printer and biocompatible resin to print over 100 inserts

simultaneously (**Figure 5.1C**) that can then be autoclaved for sterility. The MLI is designed to hold 10 µL of hydrogel between two concentric circular plates **(Figure 5.1A)**. Both the top and bottom of the hydrogel are exposed to the media in the well to maximize the surface area available for diffusion between the hydrogel and external environment. Once crosslinked, the hydrogel remains stable between the concentric rings until the gel and its cellular contents can be removed via centrifugation. The concentric ring design also facilitates imaging within the MLI to monitor organoid growth and morphology (**Figure 5.1D**). Using this system, we have successfully maintained co-cultures of hepatic and tumor organoids for up to 10 days.
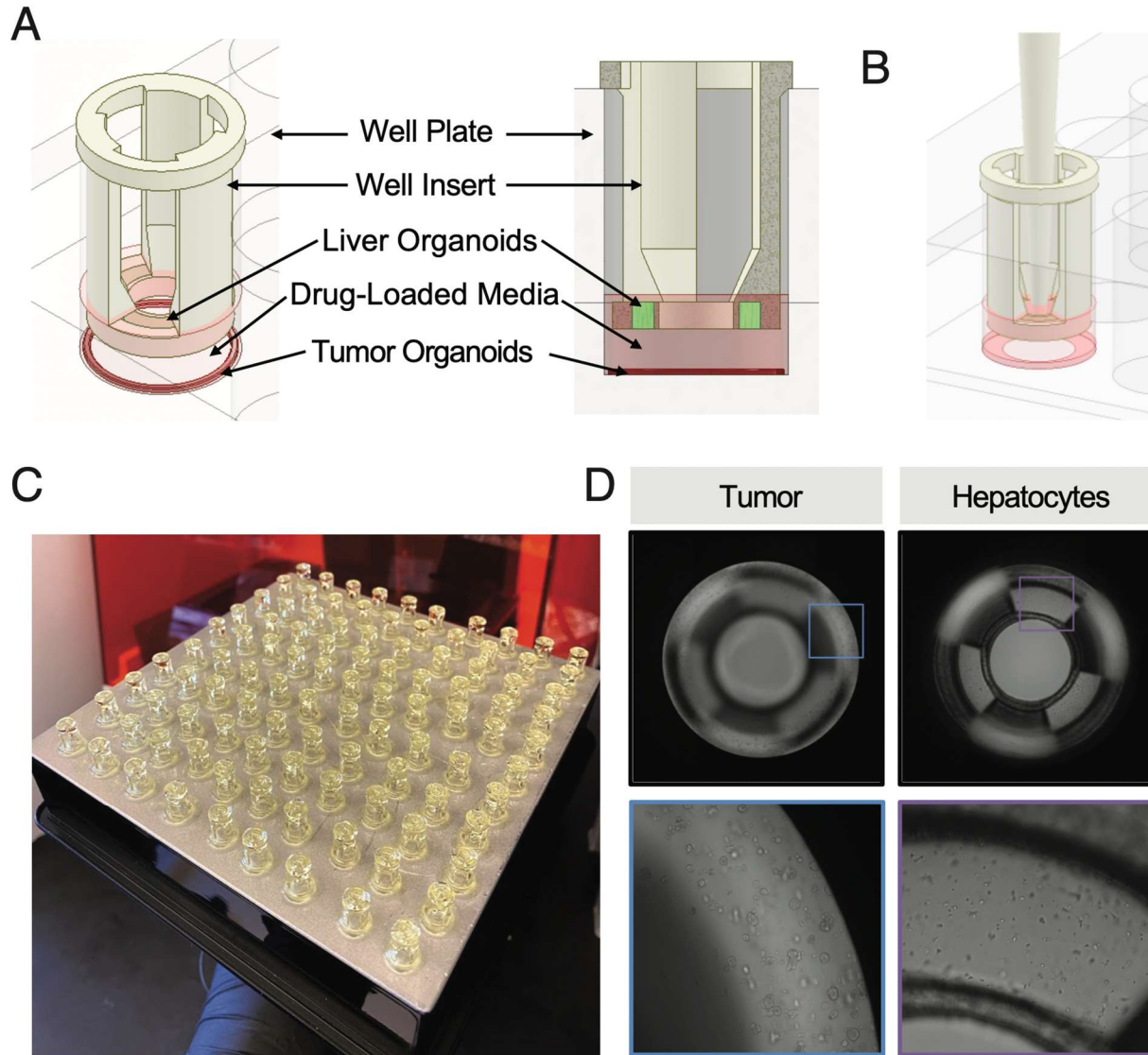
Figure 5.1: Design and manufacturing of the MLI. (A) Labeled schematics of the miniature liver insert (MLI) in a 96-well plate. The 3D-printed structure hangs from the rim of the well and immerses a 3D culture of hepatic organoids into the media within the well plate. Tumor organoids cultured in the mini-ring format can be cultured in the well below the MLI. **(B)** Schematic depicting the compatibility of the MLI with automated fluid handling. The pipette tip used to exchange media does not touch the MLI or the mini-ring seeded in the plate below. **(C)** Image of the production of over 100 MLIs through stereolithography printing of biocompatible resin. **(D)** Whole-well and magnified brightfield images showing the simultaneous culture of MCF-7 organoids and HepaRG cells co-cultured in the system.

Optimization of Cytochrome P450 enzyme expression in the MLI

The next task we pursued was identifying the optimal culture conditions for ensuring consistent expression of the metabolic proteins needed to activate the prodrugs. In our preliminary experiments, we tested both HepaRG (Thermo-Fisher) and HepG2 cell lines (Hera BioLabs). HepaRG cells are terminally differentiated human hepatocytes while HepG2 cells originate from a patient with hepatocellular carcinoma. The specific type of HepG2 cells used in our studies have been genetically modified to express only the 3A4 isoform of Cytochrome P450 (CYP). We opted to use the HepG2-204 cells instead of the HepaRG (**Figure S5.1**) and unmodified HepG2 cells to reduce the likelihood of undesirable metabolic inactivation mediated by other CYP isoforms.

Once the cell line was selected, we assessed the impact of multiple cell seeding densities and hydrogel concentrations on CYP3A4 expression (**Figure 5.2A**). We assayed the activity of the CYP3A4 enzymes in the HepG2-204 cell line compared to another HepG2 with all CYP isoforms knocked out (HepG2-hPORKO) as a negative control. We found that the knockout cell line showed no CYP3A4 activity after eight days of culture (**Figure 5.2A**). We did not observe any difference in the metabolic capacity of HepG2-204 organoids seeded at different densities within variable ratios of media to Matrigel. These findings suggest that the organoids in the MLI grow to a similar extent over eight days despite the initial number of cells seeded initially (**Figure 5.2B**). We serially imaged the organoids every 24 hours throughout the experiment and found that MLIs seeded at 15,000 cells/insert tended to lose hepatocytes as they became overgrown **(Figure 5.2B)**. Based upon the similar metabolic capacity across all tested conditions and the loss of cells due to overgrowth, we elected to proceed with using 10,000 cells per MLI in our standard (3:4) mixture of media to Matrigel.
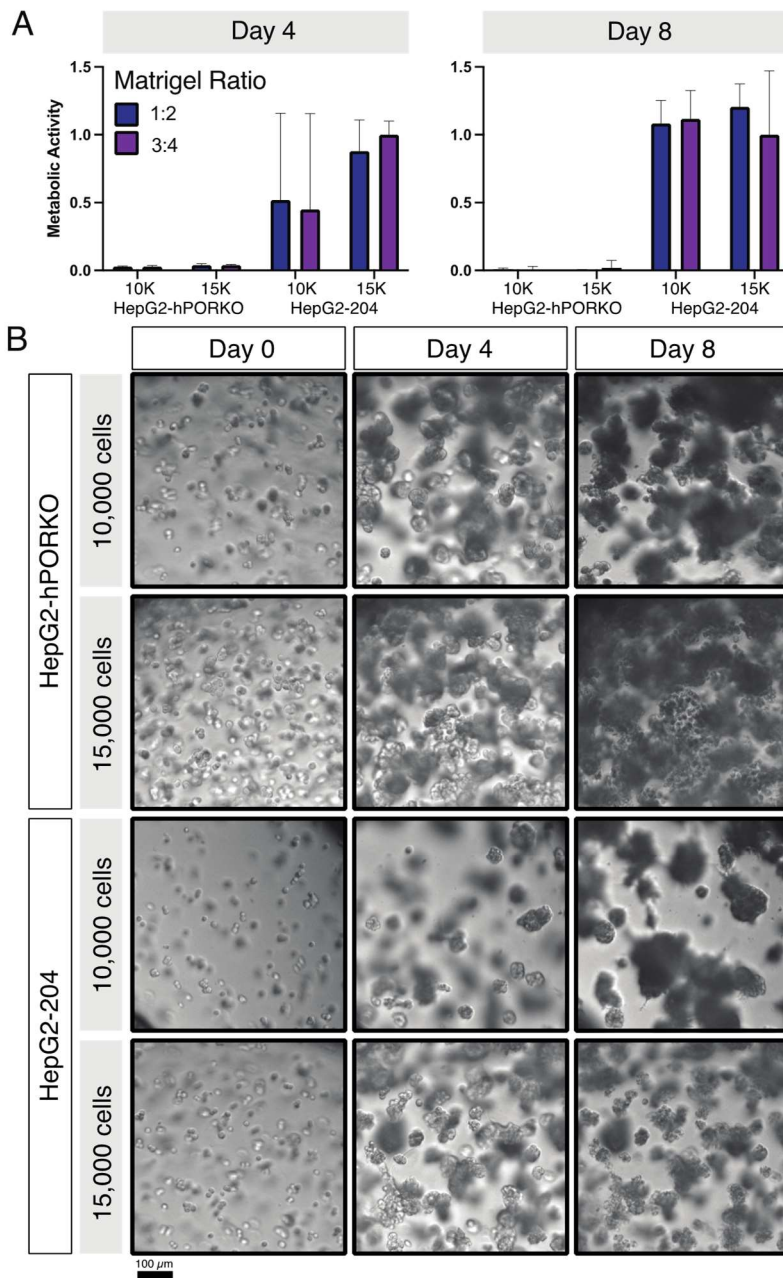
Figure 5.2: Optimizing culture conditions for hepatocyte culture in the MLI. (A) Metabolic activity of cytochrome P450 3A4 in hepatic organoid cultures in the MLI 4, 6, and 8 days after seeding. CYP3A4 activity is normalized to the 15,000 cells/well condition in a 3:4 mixture of media and Matrigel for each day. **(B)** Representative images of the hepatic organoids formed from HepG2-hPORKO and HepG2-204 cells 0-, 4-, 6-, and 8-days post-seeding at 10,000 or 15,000 cells per insert.

Screening prodrugs with the MLI

To test the viability of using the MLI within the context of drug screening, we co-cultured tumor organoids derived from fibrosarcoma (HT-1080) and osteosarcoma (HOS) cell lines. We assessed the viability of both the hepatic organoids and the tumor organoids after X days of treatment with two concentrations of cyclophosphamide and ifosfamide (**Figure 5.3**). Although we were unable to identify a signal of response amongst the tumor organoids (**Figure 5.3A, B**), we observed minor reductions in hepatic organoid viability when treated with ifosfamide. This trend appeared in HepG2-204 organoids co-cultured with both HT-1080 and HOS organoids but was only statistically significant (p-value = 0.0007 and 0.0025, 50 and 100 µM, respectively) for those in co-culture with HOS. These results led us to form the hypothesis that the hepatic organoids were capable of metabolizing ifosfamide into its active cytotoxic metabolite; however, the active metabolite was not reaching the tumor organoids in a sufficient concentration to induce organoid death.

We decided to test this hypothesis by reducing the barriers to metabolite diffusion throughout the system. Both the distance between the organoid cultures and the hydrogel encapsulating the organoids act as limiting factors to the diffusion of active metabolites. We addressed both of these issues by modifying the design of the MLI to suspend the organoid culture closer to the bottom of the well plate (**Figure 5.3B**). This adjustment changed the distance from the MLI to the bottom of the plate from 1.8mm to 0.5mm, reducing the distance of diffusion by more than a factor of three. The second modification we made was to invert the co-culture. We cultured the tumor organoids in the MLI and the hepatocytes in 2D on the bottom of the plate, thus eliminating the need for embedding hepatic organoids in a diffusion-limiting hydrogel. Prior literature demonstrated that the HepG2-204 cells showed excellent metabolic activity in 2D culture[218]. When performing pilot experiments using the inverted arrangement, we tested ifosfamide at a concentration of 50 and 100 µM. By reducing the diffusion distance, we were able

to see indications of response to ifosfamide treatment. Though we observed a trend of decreasing tumor organoid viability in response to treatment, there was notable variability between the organoid responses in each co-culture. Because of this variability, we have been unable to confirm the dose-dependent effects of ifosfamide treatment on tumor organoids cultured with hepatocytes.
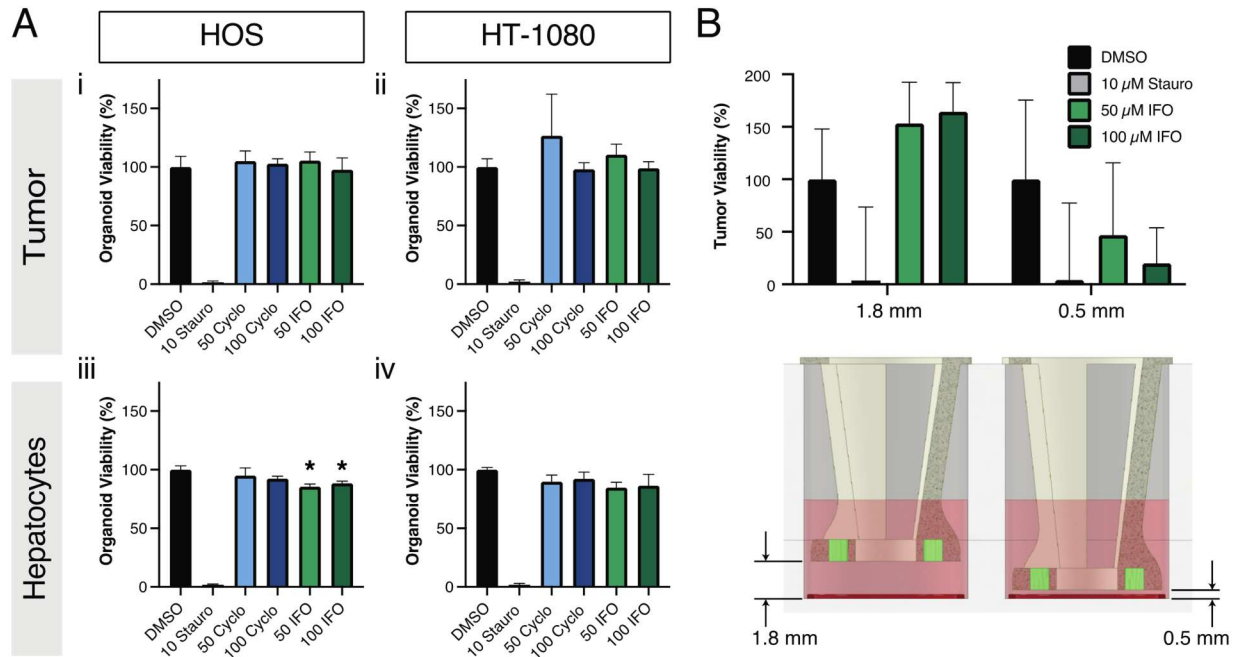
Figure 5.3: Prodrug screening on co-cultures of tumor organoids and MLI. (A) (i) Viability of HT-1080 organoids when treated with 50 and 100 µM cyclophosphamide or 50 and 100 µM ifosfamide in the presence of the MLI. (ii) Viability of HOS organoids when treated 50 and 100 µM cyclophosphamide or 50 and 100 µM ifosfamide in the presence of the MLI. (iii) Viability of HepG2-204 organoids seeded in the MLI when co-cultured with HT-1080 organoids and exposed to 50 and 100 µM cyclophosphamide and ifosfamide for 5 days. (iv) Viability of HepG2-204 organoids seeded in the MLI when co-cultured with HOS organoids and exposed to 50 and 100 µM cyclophosphamide and ifosfamide for 5 days. **(B)** Viability of tumor organoids (HOS) seeded in the MLI cultured in wells with 2D HepG2-204 cells. Treatment with 50 and 100 µM ifosfamide led to reduced organoid viability in tumor organoids cultured 0.5 mm from the hepatocytes compared to tumor organoids separated by 1.8 mm after 5 treatments over 5 days of co-culture. Renderings of the modified MLI design used to minimize the distance between the hepatic organoid cultures and the tumor organoid rings are shown below.

Discussion and Outlook

The major benefit of the MLI over other in vitro methods for introducing drug metabolism is that it is designed for high-throughput automation. Batches of 100 inserts are printed with a stereolithography printer using biocompatible resin and autoclaved before use. The open center of the insert allows the use of automated fluid handlers without risk of disrupting the tumor or hepatic organoids. Additionally, the MLI design allows for continuous, noninvasive imaging of cells cultured on the bottom of the well and within the MLI by simply changing the focal plane.

Though the logistical aspects of the platform are performing as expected, we have yet to see definitive data that suggests hepatocytes seeded in the MLI can reproducibly and reliably metabolize prodrugs into their active, cytotoxic forms for uptake by co-cultured tumor organoids. We hypothesized that this could be a result of limited metabolic capacity of the hepatic organoids, sub-optimal culture conditions relating to the cell density and ECM, or to the distance that must be bridged by diffusing active metabolites. Despite extensive work investigating each of these hypotheses, we are unable to make claims regarding the efficacy of the platform in studying these drugs. One of the leading hypotheses as to the lack of efficacy of the platform is that the hepatocytes are metabolizing the compounds into inactive formulations. Though we have attempted to control this by using hepatocytes genetically modified to express only the CYP3A4 isoform, outside environmental conditions and metabolite instability may still cause inactivation.

Moving forward, we have identified three primary directions for further development. The first is to expand the number and concentration ranges of drugs tested. We plan to add irinotecan, a prodrug topoisomerase inhibitor, which has a stable metabolite SN-38 that can be screened independently as a positive control[219]. The second is altering the environment in which the hepatocytes are cultured to reduce the oxygen tension to levels found within the pericentral zone of the liver where most drug metabolism occurs *in vivo*[220,221]. Another approach that will be studied is the use of microsomes, subcellular fractions of hepatocytes, that contain the metabolic

enzymes of interested[222]. These microsomes can be derived from homogeneous cell populations to maintain consistency while eliminating other cellular machinery that may interfere with the metabolism and exportation of the active compound. Though our work thus far has yet to achieve the goal of metabolizing prodrugs for drug screening, it does support the notion that tumor models must capture enough complexity of the biological system to be useful. Our results thus far suggest that additional modifications to the drug treatment, co-culture conditions, or microenvironment will be needed to make this screening approach a reality.

Methods

Design and Manufacturing of the MLI

The MLI was designed in Inventor (Autodesk) and 3D printed using a Form3B (Formlabs). The object was exported as an STL file from Inventor before being loaded for slicing and printing in PreForm (Formlabs). In PreForm, the model was oriented to print with the rim touching the surface of the build platform to maximize resolution of the features suspended within the well. The parts were then printed using biocompatible BioMed Amber resin (Formlabs) and post-processed by removing excess resin with two 10-minute washes in isopropyl alcohol followed by drying with compressed air. Parts were allowed to fully dry in ambient conditions for at least 30 minutes prior to curing them in the Form Cure lightbox for 30 minutes at 70°C. Once cured, all MLIs were autoclaved for sterility prior to use.

Cell Lines

Multiple hepatocyte cell lines were used in this study. HepaRG cells (Thermo-Fisher) were cultured per the distributor's recommendations using two media variants: Thaw, Plate, and General Purpose, and Maintenance and Metabolism medium. Three genetically modified HepG2 cell lines (HepG2-204, HepG2-206, and HepG2-hPORKO) (Hera BioLabs) were cultured in

EMEM medium supplemented with 10% FBS. Cell lines were maintained in culture below passage 10 for use in experiments.

Cytochrome P450 Metabolic Activity Analysis

The metabolic capacity of the MLI was assessed using the P450-Glo™ assay (Promega) used in accordance with the manufacturer's instructions. We suspended hepatocytes (either HepaRG or HepG2-204) in the media-Matrigel mixture at the prescribed density. We then loaded 10 µL of the cell-matrix suspension to the MLI by depositing material in the concentric rings. We incubated the MLIs at 37°C to crosslink the gel prior to adding medium. The loaded MLIs were placed in a 96-well plate and medium was added using an automated fluid handler (Nimbus, Hamilton). Medium was replenished daily beginning on day 3 and proceeding to day 7. On the final day, media containing the P450-Glo™ reagent was added to each well. After 24 hours, we transferred the medium to a new well plate and added the luciferase detection reagent and measured the luminescence on a plate reader (Molecular Devices).

Drug screening experiments with the MLI

Both tumor cells and hepatocytes were seeded on day 0 and allowed to grow into organoids over three days. Cells were suspended in a 3:4 solution of medium to Matrigel per our standard protocol[9,138]. Tumor cells were seeded around the periphery of each well of a 96-well while hepatocytes were seeded in the MLI as described above. On day 3, we initiated the co-culture of the organoids by transferring the MLIs to the well plate with the tumor organoids. Drug-loaded medium was then supplied to each well and replaced every 24 hours. Brightfield images were also acquired using a high-content imaging system (Celigo, Nexcelom) daily. After 5 days of co-culture, the MLIs were transferred to a separate plate and spun at 800xg for 5 minutes to remove the gel from insert. The viability of both tumor and hepatic organoids were measured using an ATP-release assay (Promega).

Investigating radiotherapy and chemoradiation treatment modalities with organoids

Introduction

Radiotherapy (RT) is one of the primary treatment options for many types of cancer, especially advanced and non-surgical cases[1,2]. Because of its broad clinical utility, functional precision medicine platforms that identify lesions sensitive to radiotherapy would be useful in crafting treatment plans. External beam radiation methods, such as stereotactic body radiation therapy (SBRT) are indicated for bone and soft tissue sarcomas[1,2]. SBRT treats tumors by delivery high-doses of X-rays that cause DNA damage that lead to cell death over time. Unlike cytotoxic drugs, radiation therapies may not be immediately effective at causing cell death as treatment relies upon the gradual accumulation of DNA mutations in the tumor over multiple fractions leading to different mechanisms of cell death[223]. Beyond the differing mechanisms of action against cancer cells, radiotherapy also requires the use of specialized equipment to generate and deliver X-rays to the tissue. Because of the differences in the mechanism of action and method for delivering therapy, we sought to develop a protocol for screening radiotherapy in tumor organoids.

Several other studies have studied radiotherapy on tumor organoids with the same goal of predicting patient-response to treatment[64,90,224]. Pasch et al. developed organoids from patients with colorectal cancer and tested combination chemoradiation with 5-fluorouracil (5-FU). They observed a variety of patient-specific responses to treatment including organoid death, stagnation, and growth. Moreover, they observed a varying extent of synergism between the treatment modalities in each patient. Another study of nasopharyngeal organoids by Lucky et al had similar findings using larger organoids[224]. They identified hypoxia and varied microenvironmental conditions as key drivers of resistance to treatment. They also found that varied dosing schedules with multiple fractions led to different outcomes. Hsu et al built upon this

work and were successfully able to generate colorectal cancer organoids that predicted response to radiotherapy in patients[90]. In a panel of five cases, patient response as measured using RECIST criteria correlated with the extent of organoid response *in vitro* and the organoids effectively predicted two patients with complete responses to therapy.

Existing studies have demonstrated the predictive power of organoids for testing RT in small groups of patients. Our goal was to build upon these results to create a system for screening larger panels of combination drug and radiotherapies. The pipeline we have developed for the investigation of radiation therapy on tumor organoids builds upon our existing mini-ring platform. By building the protocol around the existing high-throughput framework for evaluating treatments, our platform has the unique ability to accommodate combination chemotherapy and radiotherapy that can better mimic the treatment regimens prescribed clinically.

Results

Organoids show molecular and cellular response to radiotherapy

Our first goal was to verify that organoids cultured in our system were susceptible to radiotherapy. We used a UPS-like cell line, KP3172R, that had shown sensitivity to RT in 2D experiments (unpublished data, Kalbasi Lab UCLA). We seeded KP3172R organoids at a density of 2,500 cells per well in our standard mini-ring conformation[9,138] in three separate 96-well plates. Each plate was treated with a varying dose of radiation up to 12 Gy (**Figure 5.4A**). We found that organoids radiated with a single fraction of 12 Gy radiation showed numerous γH2AX foci 45 minutes after treatment compared to untreated organoids indicating extensive DNA damage within some cells (**Figure 5.4A**). Interestingly, we observed significant heterogeneity in the number of γH2AX foci in radiated nuclei amongst individual cells within larger organoids (**Figure 5.4A**). After 72 hours of culture, we assessed the viability of the organoids with an ATP assay and found a reduction in organoid viability for treated specimens (**Figure 5.4B**).
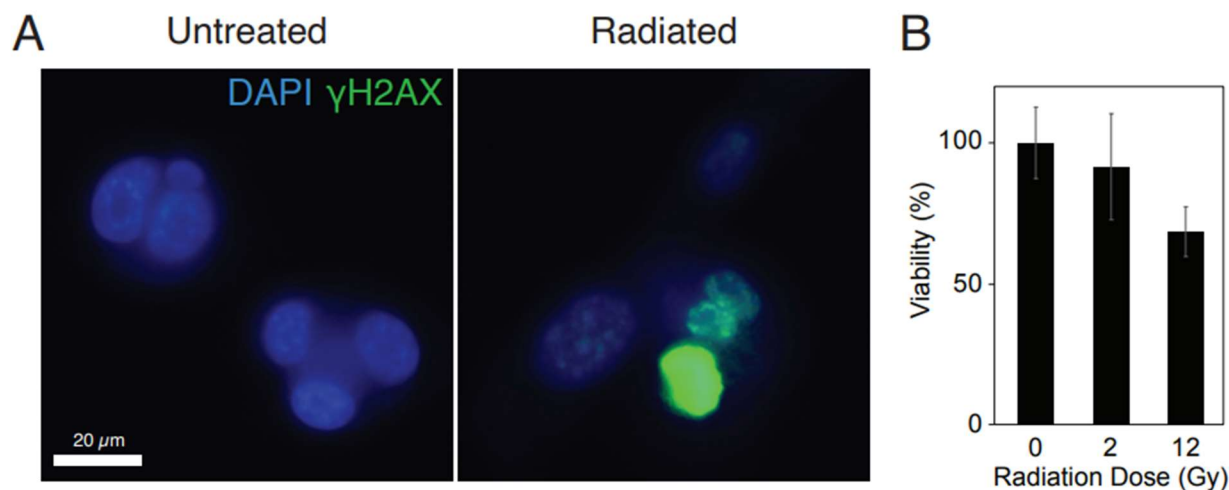
Figure 5.4: UPS organoids respond to radiation therapy. (A) Immunofluorescent staining of γH2AX shows DNA damaged only in irradiated KP3172R cells. **(B)** Radiation-dependent reduction in cell viability in the same cells 72h post-exposure.

Once establishing that the model showed sensitivity to RT, we proceeded to test the impact of multiple radiotherapy fractions on viability. We plated organoids in a 96-well plate and radiated each column of organoids with up to 5 fractions of 6 Gy RT. To collect time-resolved data regarding response to treatment, we measured organoid viability using serial brightfield imaging every 24 hours. Using these images, we segmented each image using a neural network, calculated the surface area covered by in-focus organoids, and normalized the covered area of each well to the covered area in the same well prior to treatment[10]. We found a clear separation between the growth of radiated and untreated organoids; however, there was no additional inhibition of organoid growth from added radiation doses over time (**Figure 5.5A**).

An open question following the preliminary RT studies was the impact of location within the hydrogel on organoid growth. We used a high-content imaging system (Celigo, Nexcelom) to take three images per position at varying focal distances. The first plane would focus on the organoids growing near the surface of the plate, the other two imaging planes were 100 and 150 μm above the surface of the plate. The lowest imaging plane tended to capture 2D cell growth on

the well bottom, while the focal planes away from the surface focused on organoids in 3D. We found the middle plane to provide the most representative data regarding 3D organoid growth as the lowest plane was skewed by the exponential 2D cell growth and the higher plane captured too few organoids within the gel to provide a reliable signal (**Figure 5.5B**).

While our previous data suggested that we were capable of measuring organoid response to RT alone, we were also interested in testing the platform's utility for combination therapies. Our collaborators in the Kalbasi Lab (UCLA) identified a dsRNA drug, BO-112[225,226], that showed synergistic behavior with RT when tested on KP3172R cells in 2D culture and PDX models. We screened three radiation doses (0, 4, and 8 Gy) in tandem with three doses of BO-112 (0, 0.5, and 1 mg/mL) on organoids seeded at two densities (500 and 1000 cells/well) (**Figure 5.5C**). We first assessed the toxicity of BO-112 in the absence of RT and found that organoids seeded at 1000 cells/well showed a dose-response with the 1 mg/mL dose of BO-112 leading to a strong inhibition of growth during treatment (**Figure 5.5C**). Surprisingly, KP3172R organoids seeded at 500cells/well demonstrated the inverse trend in which increasing doses of BO-112 stimulated 3D organoid growth over time. When assessing the impact of RT alone, we observed similar patterns of decreased organoid growth across both seeding densities (**Figure 5.5D**). Finally, we calculated the normalized area under the growth curves (normalized AUC) to compare the combinatorial effects of RT and BO-112. Our results were consistent with the experiments above in that we observed different responses based on cell density. For sparsely seeded organoids, treatment with BO-112 was a driver of growth in the absence of RT, but also conferred radioprotective effects when used concurrently with RT (**Figure 5.5E**). While 1mg/mL was able to maintain net organoid growth despite 8 Gy RT, BO-112 delivered at 0.5 mg/mL was unable to overcome the 8 Gy RT dose (**Figure 5.5E**). Combination BO-112 and RT for organoids seeded at 1000 cells/well, however, was effective in augmenting the response of either treatment alone (**Figure 5.5E**).
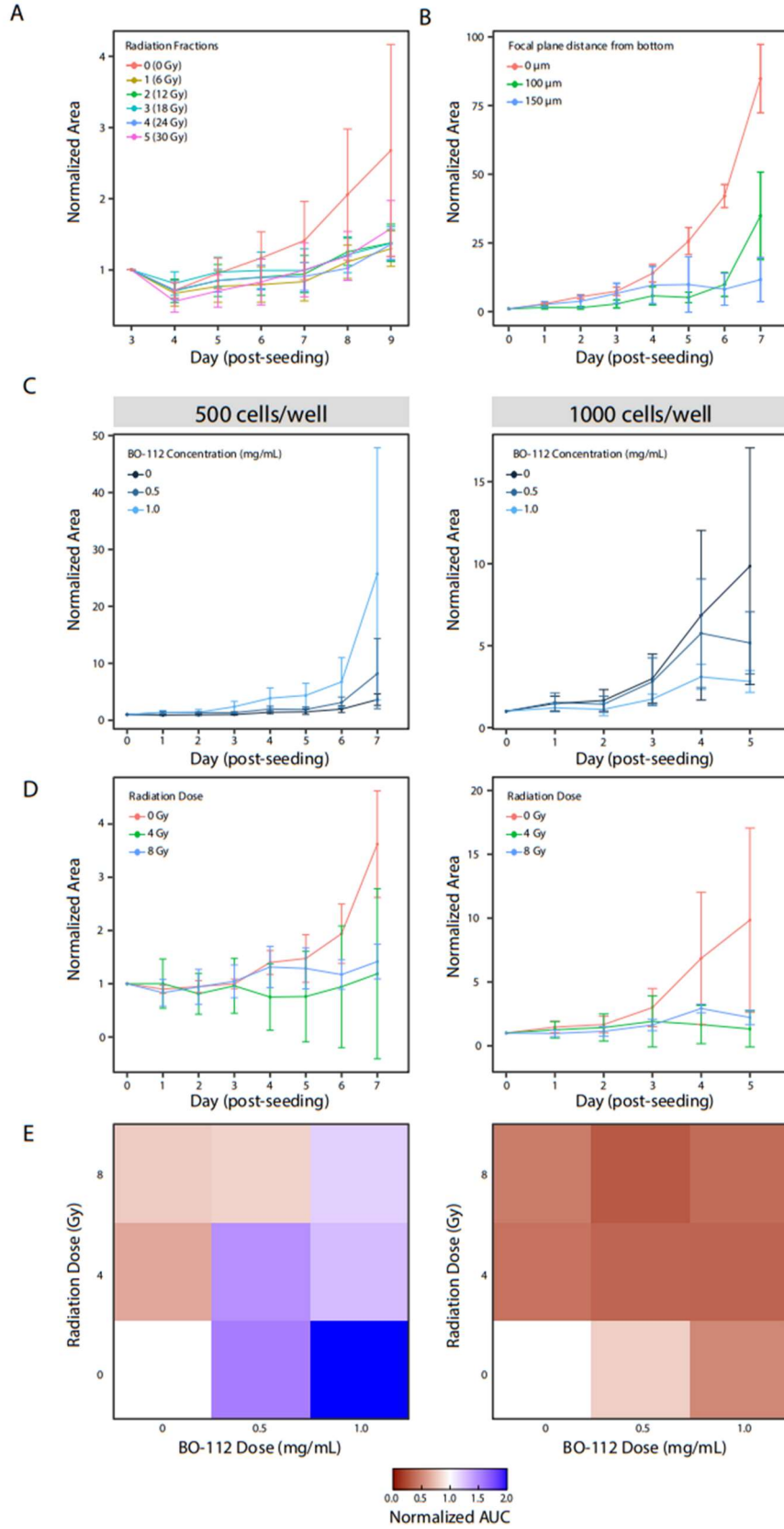
Figure 5.5: Effect of RT on sarcoma organoids. (A) Effect of multiple fractions of RT over time. Each dose was 6 Gy and doses were 24 hours apart. Cross-sectional area of organoids within each well were measured by segmenting brightfield images with a trained U-Net model. Organoid area was normalized to the organoid coverage immediately preceding treatment on day 3. **(B)** Organoid growth differs by position within the 3D hydrogel. Images were taken at three focal planes: directly above the glass bottom, 100 μm above the glass, and 150 μm above the glass. **(C-E)** Comparison of combination RT and BO-112 treatment on KP3172R cells. Cells were seeded at 500 and 1000 cells/well and treated with 0, 4, or 8 Gy RT and 0, 0.5, or 1 mg/mL BO-112. **(C)** Organoid response to treatment with BO-112 treatment in the absence of RT. **(D)** Organoid response to treatment with RT in the absence of BO-112. **(E)** Heatmaps of the normalized area under curve (AUC) of organoids treated with combinations of BO-112 and RT.

Concurrent drug and radiotherapy interventions yield synergistic responses in organoids

Given the promising results of our pilot investigation with one drug, we pursued a study incorporating a subset of drugs that are either currently used or under investigation as radiosensitizers. We cultured organoids for three days prior to administering one dose of RT (0, 4, or 8 Gy) and drug. Drugs were screened at 1uM, except for BO-112 that was tested at 1 mg/mL, cisplatin tested at 50 μM, and carboplatin tested at 25 μM. We performed both image analysis to measure growth (**Figure 5.6A**) and an ATP assay to measure organoid viability (**Figure 5.6B**). As seen in previous experiments, we observed a cell density dependent response to treatment with organoids seeded at 5000 cells/well showing greater resistance to 4 Gy radiation than their less dense counterparts (**Figure 5.6A**). We observed broad drug-related toxicity in our positive control, staurosporine, in addition to trabectedin and lurbinectedin (**Figure 5.6A**). Prexasertib, a checkpoint kinase inhibitor indicated for platinum-resistant tumors, showed a synergist effect when co-administered with 8 Gy radiation at both cell densities. Doxorubicin showed a similar additive effect of both modalities of treatment; however, this can only be seen in organoids seeded at 2000 cells/well (**Figure 5.6A**). To further investigate the effects of treatment, we performed an ATP assay on each plate. Due to experimental limitations, all organoids seeded in a single plate

were exposed to a given dose of radiation. This limits our ability to effectively normalize the data outcomes to effectively compare viability across radiation doses. Despite this limitation, we still observed an added combinatorial effect of prexasertib on organoids seeded at 5000 cells/well (**Figure 5.6B**). Likewise, carboplatin, doxorubicin, and gemcitabine also showed stronger responses to combination 8 Gy RT and drug treatment in the denser organoid cultures. In the 2000 cells/well condition, we only see a reliable additive effect of doxorubicin and 8 Gy treatment (**Figure 5.6B**).
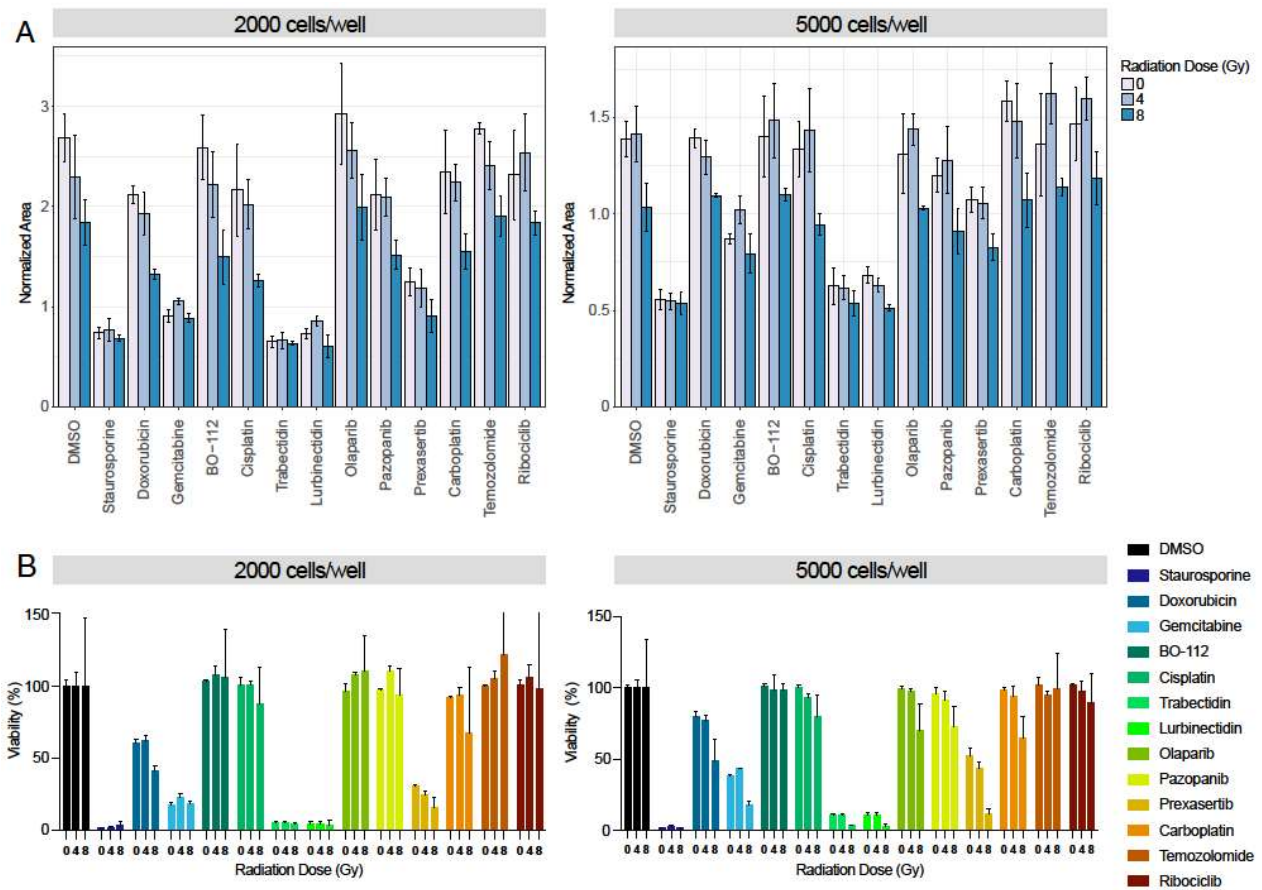
Figure 5.6: Combination RT and drug screening on sarcoma organoids. (A) Normalized area of organoids on day 5 post-seeding. Treatment was administered on day 3. Cells were plated at both 2,000 and 5,000 cells/well. Red bars correspond to non-radiated organoids, green and blue correspond to 4 and 8 Gy treatment, respectively. **(B)** Organoid viability measured by ATP assay. Viability values normalized to the luminescence of DMSO-treated organoids for each radiation dose. Each color represents a different drug, the three bars in each group represent the escalating radiation dose.

Discussion

Though we are not the first group to radiate organoids[60,64,90,93], the novelty of our work lies within the ability to do so within the context of a high-throughput screening system. Pasch et al. and Hsu et al. have demonstrated the ability to correlate organoid response to radiotherapy and patient response to treatment in a small subset of patients[64,90]. Our goal is to build upon our existing drug screening pipeline to develop a system to identify combination chemoradiotherapies likely to be effective for individual patients. Our drug screening data showing variable efficacy of treatments across four patient-derived cell lines provides the foundation for launching further investigations on organoids derived directly from surgical biopsies and resections.

One of the key advancements that enables this work is the use of our brightfield image segmentation technique to track organoid growth over time (**Figure S5.1**). This analysis is best-suited for radiated organoids as it allows for more frequent sampling of growth and it eliminates the need for endpoint viability assays that may be unable to detect changes in growth rate for slow-growing samples. Though it does have advantages, the measurements are more sensitive to variability due to debris in the well, hydrogel folding, and different patterns of organoid growth in each well. While the current model is trained on 200 images across an array of tumor types, broader models may need to be trained to accommodate the enormous heterogeneity in organoid morphology. ATP assays, though effective for making comparisons within a single well plate, are difficult to adapt to multi-plate experiments as untreated negative controls would be needed on

each plate. Though we have successfully used lead blocks to shield portions of the plate from radiation, these blocks are not effective and preventing exposure to scattered X-rays and can be logistically challenging to implement when trying to shield a handful of wells. Moving forward, we intend to investigate the use of other endpoint assays, such as fluorescent live/dead stains, to make absolute measurements that can be compared across plates.

Though the preliminary drug screening results establish the feasibility of testing drug-radiotherapy combinations, additional testing will be required to identify the optimal drug concentrations and seeding densities. For example, the cytotoxic effects of trabectedin and lurbinectedin were sufficient in the absence of RT to kill most organoids and must be tested at lower concentrations to identify additive or synergistic effects between treatments. In addition, the striking differences in response to BO-112 in KP3172R cells based upon the seeding density provide an important lesson that response to therapy is heavily dependent on the environmental conditions. One potential solution is to perform drug screens on organoids seeded at a variety of densities, however this option may be limited as this work proceeds to screening patient-derived organoids originating from scarce and precious samples.

Overall, the body of work conducted thus far shows that the mini-ring drug screening platform can be adapted to screen combination chemoradiotherapies with the assistance of machine learning-based image analysis. Though the optimal seeding densities, drug concentrations, and radiation doses can be further optimized in future experiments, we have established basic parameters and the chemoradiation HTS organoid platform will be a powerful tool to functionally screen an additional treatment modality crucial for soft tissue sarcoma and other tumor types.

Methods

Cell Culture

KP3172R and USARC2 cells were cultured in petri dishes with DMEM supplemented with 10% FBS and 1% penicillin-streptomycin up to passage 10. Medium was changed every three days and cells were passaged when approaching 80% confluence.

Immunofluorescence

We performed immunofluorescence on radiated organoids to confirm the presence of γH2AX foci indicative of DNA damage. We fixed the organoids by adding 10% buffered formalin and incubating for 5 minutes at 37°C. Organoids were then placed on ice for 30 minutes and stored overnight at 4°C. Samples were permeabilized using 0.5% Triton X-100 in PBS for 1 hour with gentle agitation. We then added an FBS-based blocking buffer for 3 hours followed by overnight incubation with the primary antibody (ab195188, Abcam). Images were acquired with a fluorescent microscope (Zeiss) and post-processed in Zen Blue (Zeiss).

Growth analysis in brightfield images using U-Net

We image the organoids daily using a high-content microscope that scans two focal planes per well. The resulting whole-well images are exported in TIF format at a resolution of 1 µm/pixel. We then implement our previously developed methodology to segment and quantify regions of the image containing organoids[95]. We use a convolutional neural network with a U-Net architecture[104] to segment the regions of the images containing organoids. This model is based on a ResNet-34 model[123] trained on 223 manually-labelled images spanning an array of tumors of origin to capture the diverse organoid morphologies observed in this study. In the manually labelled dataset, only in-focus organoids are marked for inclusion in the area calculation; this is done to minimize measuring the same organoid across both focal planes. The original weights were derived from a model pretrained on the ImageNet dataset[124] and the final model was trained

over 80 epochs using a cross-entropy loss function. The trained model was then used to segment each image by splitting the image into 512x512 pixel sections, applying the model to each section, and reassembling the sections to recreate the whole segmented image (16,896x16896 pixels).

We then implement OpenCV to calculate the total area of the organoids in each focal plane. This area is then averaged across both focal planes and growth is measured by normalizing to the area covered by organoids on the first day of imaging of the same well. The resulting data was then plotted using GraphPad Prism as normalized area over time.

Drug Screening Experiments

Cells were suspended in our standard hydrogel matrix composed of 3 parts medium to 4 parts Matrigel and deposited around the periphery of each well of a 96-well plate[9,138]. Organoids were allowed to grow for three days prior to treatment and were imaged daily for the duration of the experiment. Organoids were radiated using an X-ray cabinet and treatment was added immediately after RT using an automated liquid handler. Radiation schedules varied as described in the Results section above for each experiment.
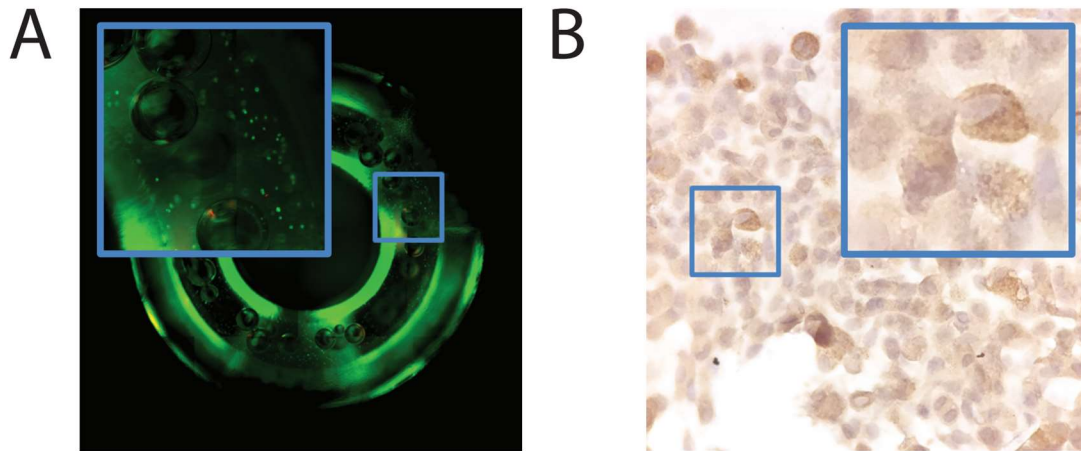
Figure S5.1: Hepatocyte viability and Cytochrome P450 expression in the MLI after 72 hours. (A) Fluorescent image of viable HepaRG cells loaded in the MLI. Live cells are stained with acridine orange (green), and dead cells are stained with propidium iodide (red). **(B)** Immunohistochemical staining of Cytochrome P450 3A4 of HepaRG cells cultured in the MLI for 72 hours. Brown staining indicates cytoplasmic expression of the cytochrome P450 enzyme.
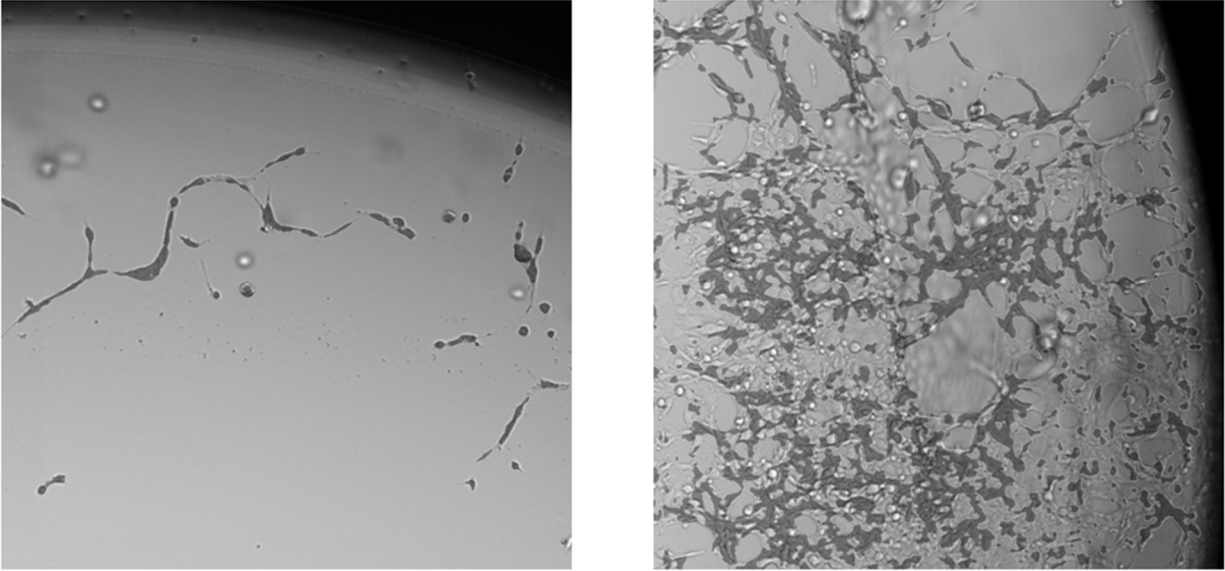
Figure S5.2: U-Net performance on spindle-morphology and high-density organoid networks. Machine-learning based segmentation of UPS organoids is effective at low cell densities but has difficulty when segmenting extensive networks of cells across multiple focal planes.

Chapter 6: Conclusions and Outlook

While precision medicine is not a new concept, the technology that enables its use in clinical care is developing at a rapid pace. Thanks to massive reductions in cost, genomic sequencing is now a standard component of the cancer diagnosis strategy for many tumors[227]. While the full potential of genomic precision medicine has yet to be reached, approaches like functional precision medicine may fill the gap. Thus far, patient-derived tumor organoids have been the leading tool in functional precision medicine assays testing therapies on live tissue. Several studies have demonstrated promising early results in using organoids as surrogates of patient response to treatment[50,51,55,90,93] and multiple groups abroad are proceeding with clinical trials to rigorously evaluate their utility.

The platforms used to establish and analyze organoids used in functional assays differ from group to group. We have developed our mini-ring screening methodology[9,78] to be scalable with laboratory automation and have applied the system to organoids derived from a variety of tumor types. Chapter 3 describes our work with sarcoma organoids and demonstrates that a clinical functional precision medicine pipeline is not only feasible, but also informative. Our findings highlight the heterogeneity found amongst the different histologic subtypes of sarcoma and anecdotal evidence suggests that functional approaches can predict genomic features and patient response.

The clinical implementation of organoid-based assays will require further advances in automation and analysis to provide wholistic understandings of tumor response to treatment. To address this need, we developed a bioprinting pipeline to automate the seeding of our organoid models. This also allowed us to optimize each model for imaging using a high-speed live cell interferometer capable of providing time-resolved mass data with single-organoid resolution. This

platform has the unique ability to probe the heterogeneity in organoid response to treatment that may lead to more informed drug selection in clinical practice.

The further development of systems for screening prodrugs and radiotherapy will expand the utility of functional precision medicine beyond traditional drug libraries. Platforms like these will allow for a comprehensive investigation of all treatment options available to patients and physicians. The limited early success of our MLI platform stands as an important reminder that not all physiological phenomena can be captured easily in simplified models. However, an in-depth understanding of the biological processes at play can provide clues as to how to intelligently increase the complexity of the model without sacrificing the ease of use and throughput of the system. Additionally, our radiation screening results highlight the need for the proper selection of both the model and the analytical methods to fully understand response to treatment. Other treatment modalities that also require new development include immunotherapies and stromal cell-targeting drugs, but the expansion of the capabilities of *in vitro* platforms will be a necessary step in recommending the best possible treatment for each patient.

As this field of research progresses, clinical trials evaluating the relationship between organoid and patient response will be essential in driving progress. Open questions regarding the optimal environmental conditions, duration of culture, and required complexity of the models used remain to be answered. While these platforms are currently in the early stages of investigation, commercial systems have already started to appear and will further attract funding to make the vision of functional precision medicine a reality. Just as genome sequencing made its transition from laboratory bench to patient bedside, organoid screening systems are destined to take a similar path. As the search for improved clinical outcomes continues, precision medicine - in all of its forms - will be instrumental in guiding the selection of treatments and providing hope to patients battling cancer.

Bibliography

1. NCCN Guidelines Version 2.2023: Bone Cancer. (2022).

2. NCCN Guidelines Version 2.2022: Soft Tissue Sarcoma. (2022).

3. Ginsburg, G. S. & Phillips, K. A. Precision Medicine: From Science To Value. *Health Affairs* **37**, 694–701 (2018).

4. Koh, W.-J., Anderson, B. O. & Carlson, R. W. NCCN resource-stratified and harmonized guidelines: A paradigm for optimizing global cancer care. *Cancer* **126**, 2416–2423 (2020).

5. Burrell, R. A., McGranahan, N., Bartek, J. & Swanton, C. The causes and consequences of genetic heterogeneity in cancer evolution. *Nature* **501**, 338–345 (2013).

6. Sachs, N. *et al.* A Living Biobank of Breast Cancer Organoids Captures Disease Heterogeneity. *Cell* **172**, 373-386.e10 (2018).

7. Skubitz, K. M., Pambuccian, S., Manivel, J. C. & Skubitz, A. P. N. Identification of heterogeneity among soft tissue sarcomas by gene expression profiles from different tumors. *J Transl Med* **6**, 23–23 (2008).

8. Bousquet, M. *et al.* Whole-exome sequencing in osteosarcoma reveals important heterogeneity of genetic alterations. *Ann Oncol* **27**, 738–44 (2016).

9. Phan, N. *et al.* A simple high-throughput approach identifies actionable drug sensitivities in patient-derived tumor organoids. *Commun Biol* **2**, 1–11 (2019).

10. Al Shihabi, A. *et al.* Personalized chordoma organoids for drug discovery studies. *Science Advances* **8**, eabl3674.

11. Stanta, G. & Bonin, S. Overview on Clinical Relevance of Intra-Tumor Heterogeneity. *Front. Med.* **5**, (2018).

12. Boutros, P. C. *et al.* Spatial genomic heterogeneity within localized, multifocal prostate cancer. *Nature Genetics* **47**, 736–745 (2015).

13. Martelotto, L. G., Ng, C. K., Piscuoglio, S., Weigelt, B. & Reis-Filho, J. S. Breast cancer intra-tumor heterogeneity. *Breast Cancer Res* **16**, 210 (2014).

14. Dentro, S. C. *et al.* Characterizing genetic intra-tumor heterogeneity across 2,658 human cancer genomes. *Cell* **184**, 2239-2254.e39 (2021).

15. Tsimberidou, A. M., Fountzilas, E., Nikanjam, M. & Kurzrock, R. Review of precision cancer medicine: Evolution of the treatment paradigm. *Cancer Treatment Reviews* **86**, 102019 (2020).

16. Morgan, G., Aftimos, P. & Awada, A. Current-day precision oncology: from cancer prevention, screening, drug development, and treatment – have we fallen short of the promise? *Current Opinion in Oncology* **28**, 441–446 (2016).

17. Flaherty, K. T. *et al.* The Molecular Analysis for Therapy Choice (NCI-MATCH) Trial: Lessons for Genomic Trial Design. *J Natl Cancer Inst* **112**, 1021–1029 (2020).

18. Do, K., Coyne, G. O. & Chen, A. P. An overview of the NCI precision medicine trials—NCI MATCH and MPACT. *Chinese Clinical Oncology* **4**, 31–31 (2015).

19. NCI-MATCH Treatment Arms Table. *ECOG-ACRIN Cancer Research Group* https://ecog-acrin.org/nci-match-eay131/.

20. Damodaran, S. *et al.* Phase II Study of Copanlisib in Patients With Tumors With PIK3CA Mutations: Results From the NCI-MATCH ECOG-ACRIN Trial (EAY131) Subprotocol Z1F. *JCO* **40**, 1552–1561 (2022).

21. Salama, A. K. S. *et al.* Dabrafenib and Trametinib in Patients With Tumors With BRAFV600E Mutations: Results of the NCI-MATCH Trial Subprotocol H. *JCO* **38**, 3895–3904 (2020).

22. Azad, N. S. *et al.* Nivolumab Is Effective in Mismatch Repair–Deficient Noncolorectal Cancers: Results From Arm Z1D—A Subprotocol of the NCI-MATCH (EAY131) Study. *JCO* **38**, 214–222 (2020).

23. Kalinsky, K. *et al.* Effect of Capivasertib in Patients With an AKT1 E17K-Mutated Tumor: NCI-MATCH Subprotocol EAY131-Y Nonrandomized Trial. *JAMA Oncology* **7**, 271–278 (2021).

24. Phase II Study of Taselisib in PIK3CA-Mutated Solid Tumors Other Than Breast and Squamous Lung Cancer: Results From the NCI-MATCH ECOG-ACRIN Trial (EAY131) Subprotocol I | JCO Precision Oncology. https://ascopubs.org/doi/full/10.1200/PO.21.00424.

25. Clark, A. S. *et al.* Abstract LB-010: Molecular analysis for therapy choice (NCI-MATCH, EAY131) arm Z1B: Phase II trial of palbociclib for CCND1, 2 or 3 amplified tumors. *Cancer Research* **79**, LB-010 (2019).

26. Subbiah, V. *et al.* Abstract CT160: BVD-523FB (Ulixertinib) in Patients with Tumors with BRAF Fusions, or with Non-V600E, Non-V600K BRAF Mutations: Results from the NCI-MATCH ECOG-ACRIN Trial (EAY131) Sub-protocol EAY131-Z1L. *Cancer Research* **82**, CT160 (2022).

27. Janku, F. *et al.* NCI-MATCH Arms N & P: Phase II study of PI3K beta inhibitor GSK2636771 in patients (pts) with cancers (ca) with PTEN mutation/deletion (mut/del) or PTEN protein loss. *Annals of Oncology* **29**, viii137 (2018).

28. Voest, E. E. & Bernards, R. DNA-Guided Precision Medicine for Cancer: A Case of Irrational Exuberance? *Cancer Discov* **6**, 130–132 (2016).

29. Prasad, V., Fojo, T. & Brada, M. Precision oncology: origins, optimism, and potential. *Lancet Oncol* **17**, e81–e86 (2016).

30. Tannock, I. F. & Hickman, J. A. Limits to Personalized Cancer Medicine. *https://doi.org/10.1056/NEJMsb1607705* (2016) doi:10.1056/NEJMsb1607705.

31. Lam, S. S.-Y., He, A. B.-L. & Leung, A. Y.-H. Treatment of acute myeloid leukemia in the next decade – Towards real-time functional testing and personalized medicine. *Blood Reviews* **31**, 418–425 (2017).

32. Friedman, A. A. *et al.* Feasibility of Ultra-High-Throughput Functional Screening of Melanoma Biopsies for Discovery of Novel Cancer Drug Combinations. *Clin Cancer Res* **23**, 4680–4692 (2017).

33. Letai, A. Functional precision cancer medicine-moving beyond pure genomics. *Nat Med* **23**, 1028–1035 (2017).

34. de Souza, N. Organoids. *Nature Methods* **15**, 23–23 (2018).

35. Lo, Y.-H., Karlsson, K. & Kuo, C. J. Applications of organoids for cancer biology and precision medicine. *Nat Cancer* **1**, 761–773 (2020).

36. Porter, R. J., Murray, G. I. & McLean, M. H. Current concepts in tumour-derived organoids. *Br J Cancer* **123**, 1209–1218 (2020).

37. Birgersdotter, A., Sandberg, R. & Ernberg, I. Gene expression perturbation in vitro—A growing case for three-dimensional (3D) culture systems. *Seminars in Cancer Biology* **15**, 405–412 (2005).

38. Pickl, M. & Ries, C. H. Comparison of 3D and 2D tumor models reveals enhanced HER2 activation in 3D associated with an increased response to trastuzumab. *Oncogene* **28**, 461–468 (2009).

39. Izumchenko, E. *et al.* Patient-derived xenografts effectively capture responses to oncology therapy in a heterogeneous cohort of patients with solid tumors. *Annals of Oncology* **28**, 2595–2605 (2017).

40. Ben-David, U. *et al.* Patient-derived xenografts undergo murine-specific tumor evolution. *Nature Genetics* **49**, 1567–1575 (2017).

41. Fetah, K. *et al.* The emergence of 3D bioprinting in organ-on-chip systems. *Prog. Biomed. Eng.* **1**, 012001 (2019).

42. Gunti, S., Hoke, A. T. K., Vu, K. P. & London, N. R. Organoid and Spheroid Tumor Models: Techniques and Applications. *Cancers* **13**, 874 (2021).

43. Katt, M. E., Placone, A. L., Wong, A. D., Xu, Z. S. & Searson, P. C. In Vitro Tumor Models: Advantages, Disadvantages, Variables, and Selecting the Right Platform. *Frontiers in Bioengineering and Biotechnology* **4**, (2016).

44. Wilding, J. L. & Bodmer, W. F. Cancer Cell Lines for Drug Discovery and Development. *Cancer Research* **74**, 2377–2384 (2014).

45. Goodspeed, A., Heiser, L. M., Gray, J. W. & Costello, J. C. Tumor-Derived Cell Lines as Molecular Models of Cancer Pharmacogenomics. *Molecular Cancer Research* **14**, 3–13 (2016).

46. Driehuis, E., Kretzschmar, K. & Clevers, H. Establishment of patient-derived cancer organoids for drug-screening applications. *Nat Protoc* **15**, 3380–3409 (2020).

47. Granat, L. M. *et al.* The promises and challenges of patient-derived tumor organoids in drug development and precision oncology. *Animal Models and Experimental Medicine* **2**, 150–161 (2019).

48. Wagner, S. *et al.* Tumour-Derived Cell Lines and Their Potential for Therapy Prediction in Patients with Metastatic Colorectal Cancer. *Cancers* **13**, 4717 (2021).

49. Brodin, B. A. *et al.* Drug sensitivity testing on patient-derived sarcoma cells predicts patient response to treatment and identifies c-Sarc inhibitors as active drugs for translocation sarcomas. *Br J Cancer* **120**, 435–443 (2019).

50. Nagle, P. W., Plukker, J. Th. M., Muijs, C. T., van Luijk, P. & Coppes, R. P. Patient-derived tumor organoids for prediction of cancer treatment response. *Seminars in Cancer Biology* **53**, 258–264 (2018).

51. Wensink, G. E. *et al.* Patient-derived organoids as a predictive biomarker for treatment response in cancer patients. *npj Precis. Onc.* **5**, 1–13 (2021).

52. Shankaran, A., Prasad, K., Chaudhari, S., Brand, A. & Satyamoorthy, K. Advances in development and application of human organoids. *3 Biotech* **11**, 257 (2021).

53. LeSavage, B. L., Suhar, R. A., Broguiere, N., Lutolf, M. P. & Heilshorn, S. C. Next-generation cancer organoids. *Nat. Mater.* **21**, 143–159 (2022).

54. Jensen, L. H. *et al.* Functional precision medicine in colorectal cancer based on patient-derived tumoroids and in-vitro sensitivity drug testing. *JCO* **39**, e15567–e15567 (2021).

55. Ooft, S. N. *et al.* Patient-derived organoids can predict response to chemotherapy in metastatic colorectal cancer patients. *Science Translational Medicine* **11**, eaay2574 (2019).

56. Post, J. B., Roodhart, J. M. L. & Snippert, H. J. G. Colorectal Cancer Modeling with Organoids: Discriminating between Oncogenic RAS and BRAF Variants. *Trends in Cancer* **6**, 111–129 (2020).

57. Buzzelli, J. N., Ouaret, D., Brown, G., Allen, P. D. & Muschel, R. J. Colorectal cancer liver metastases organoids retain characteristics of original tumor and acquire chemotherapy resistance. *Stem Cell Research* **27**, 109–120 (2018).

58. van de Wetering, M. *et al.* Prospective Derivation of a Living Organoid Biobank of Colorectal Cancer Patients. *Cell* **161**, 933–945 (2015).

59. Vlachogiannis, G. *et al.* Patient-derived organoids model treatment response of metastatic gastrointestinal cancers. *Science* **359**, 920–926 (2018).

60. Park, M. *et al.* A Patient-Derived Organoid-Based Radiosensitivity Model for the Prediction of Radiation Responses in Patients with Rectal Cancer. *Cancers* **13**, 3760 (2021).

61. Forsythe, S. D. *et al.* Patient-Specific Sarcoma Organoids for Personalized Translational Research: Unification of the Operating Room with Rare Cancer Research and Clinical Implications. *Ann Surg Oncol* (2022) doi:10.1245/s10434-022-12086-y.

62. Li, X. *et al.* Breast cancer organoids from a patient with giant papillary carcinoma as a high-fidelity model. *Cancer Cell Int* **20**, 86 (2020).

63. Tanaka, N. *et al.* Head and neck cancer organoids established by modification of the CTOS method can be used to predict in vivo drug sensitivity. *Oral Oncology* **87**, 49–57 (2018).

64. Pasch, C. A. *et al.* Patient-Derived Cancer Organoid Cultures to Predict Sensitivity to Chemotherapy and Radiation. *Clin Cancer Res* **25**, 5376–5387 (2019).

65. Yao, Y. *et al.* Patient-Derived Organoids Predict Chemoradiation Responses of Locally Advanced Rectal Cancer. *Cell Stem Cell* **26**, 17-26.e6 (2020).

66. Wang, Z., Samanipour, R., Koo, K. & Kim, K. Organ-on-a-chip platforms for drug delivery and cell characterization: A review. *Sens. Mater* **27**, 487–506 (2015).

67. Kimura, H., Sakai, Y. & Fujii, T. Organ/body-on-a-chip based on microfluidic technology for drug discovery. *Drug Metabolism and Pharmacokinetics* **33**, 43–48 (2018).

68. Skardal, A., Shupe, T. & Atala, A. Organoid-on-a-chip and body-on-a-chip systems for drug screening and disease modeling. *Drug Discovery Today* **21**, 1399–1411 (2016).

69. Shuler, M. L. Advances in organ-, body-, and disease-on-a-chip systems. *Lab Chip* **19**, 9–10 (2018).

70. Benien, P. & Swami, A. 3D tumor models: history, advances and future perspectives. *Future Oncology* **10**, 1311–1327 (2014).

71. Kimlin, L. C., Casagrande, G. & Virador, V. M. In vitro three-dimensional (3D) models in cancer research: An update. *Molecular Carcinogenesis* **52**, 167–182 (2013).

72. Zhang, B., Korolj, A., Lai, B. F. L. & Radisic, M. Advances in organ-on-a-chip engineering. *Nat Rev Mater* **3**, 257–278 (2018).

73. Goldman, A. *et al.* Temporally sequenced anticancer drugs overcome adaptive resistance by targeting a vulnerable chemotherapy-induced phenotypic transition. *Nat Commun* **6**, 6139 (2015).

74. Yu, L., Chen, M. C. W. & Cheung, K. C. Droplet-based microfluidic system for multicellular tumor spheroid formation and anticancer drug testing. *Lab Chip* **10**, 2424–2432 (2010).

75. Fan, Y., Nguyen, D. T., Akay, Y., Xu, F. & Akay, M. Engineering a Brain Cancer Chip for High-throughput Drug Screening. *Sci Rep* **6**, 25062 (2016).

76. Dufresne, A., Brahmi, M., Karanian, M. & Blay, J.-Y. Using biology to guide the treatment of sarcomas and aggressive connective-tissue tumours. *Nature Reviews Clinical Oncology* **15**, 443–458 (2018).

77. American Cancer Society. *Cancer Facts & Figures 2022*. https://www.cancer.org/content/dam/cancer-org/research/cancer-facts-and-statistics/annual-cancer-facts-and-figures/2022/2022-cancer-facts-and-figures.pdf (2022).

78. Nguyen, H. T. L. & Soragni, A. Patient-Derived Tumor Organoid Rings for Histologic Characterization and High-Throughput Screening. *STAR Protoc* **1**, (2020).

79. Mackall, C. L., Meltzer, P. S. & Helman, L. J. Focus on sarcomas. *Cancer Cell* **2**, 175–178 (2002).

80. Miller, R. W., Young, J. L. & Novakovic, B. Childhood cancer. *Cancer* **75**, 395–405 (1995).

81. Siegel, R. L., Miller, K. D., Fuchs, H. E. & Jemal, A. Cancer statistics, 2022. *CA: A Cancer Journal for Clinicians* **72**, 7–33 (2022).

82. Perry, J. A., Seong, B. K. A. & Stegmaier, K. Biology and Therapy of Dominant Fusion Oncoproteins Involving Transcription Factor and Chromatin Regulators in Sarcomas. *Annual Review of Cancer Biology* **3**, 299–321 (2019).

83. Damerell, V., Pepper, M. S. & Prince, S. Molecular mechanisms underpinning sarcomas and implications for current and future therapy. *Sig Transduct Target Ther* **6**, 1–19 (2021).

84. Nacev, B. A. *et al.* Clinical sequencing of soft tissue and bone sarcomas delineates diverse genomic landscapes and potential therapeutic targets. *Nat Commun* **13**, 3405 (2022).

85. Carmagnani Pestana, R., Groisberg, R., Roszik, J. & Subbiah, V. Precision Oncology in Sarcomas: Divide and Conquer. *JCO Precision Oncology* 1–16 (2019) doi:10.1200/PO.18.00247.

86. McConnell, L. *et al.* A novel next generation sequencing approach to improve sarcoma diagnosis. *Mod Pathol* **33**, 1350–1359 (2020).

87. Racanelli, D. *et al.* Next-Generation Sequencing Approaches for the Identification of Pathognomonic Fusion Transcripts in Sarcomas: The Experience of the Italian ACC Sarcoma Working Group. *Front. Oncol.* **10**, 489 (2020).

88. Lucchesi, C. *et al.* Targetable Alterations in Adult Patients With Soft-Tissue Sarcomas. *JAMA Oncol* **4**, 1398–1404 (2018).

89. van der Graaf, W. T. A., Tesselaar, M. E. T., McVeigh, T. P., Oyen, W. J. G. & Fröhling, S. Biology-guided precision medicine in rare cancers: Lessons from sarcomas and neuroendocrine tumours. *Seminars in Cancer Biology* **84**, 228–241 (2022).

90. Hsu, K.-S. *et al.* Colorectal Cancer Develops Inherent Radiosensitivity That Can Be Predicted Using Patient-Derived Organoids. *Cancer Res* **82**, 2298–2312 (2022).

91. Pasch, C. A. *et al.* Patient-Derived Cancer Organoid Cultures to Predict Sensitivity to Chemotherapy and Radiation. *Clin Cancer Res* **25**, 5376–5387 (2019).

92. Ooft, S. N. *et al.* Patient-derived organoids can predict response to chemotherapy in metastatic colorectal cancer patients. *Sci. Transl. Med.* **11**, eaay2574 (2019).

93. Yao, Y. *et al.* Patient-Derived Organoids Predict Chemoradiation Responses of Locally Advanced Rectal Cancer. *Cell Stem Cell* **26**, 17-26.e6 (2020).

94. Tiriac, H. *et al.* Organoid Profiling Identifies Common Responders to Chemotherapy in Pancreatic Cancer. *Cancer Discov* **8**, 1112–1129 (2018).

95. Al Shihabi, A. *et al.* Personalized chordoma organoids for drug discovery studies. *Science Advances* **8**, eabl3674 (2022).

96. Forsythe, S. D. *et al.* Patient-Specific Sarcoma Organoids for Personalized Translational Research: Unification of the Operating Room with Rare Cancer Research and Clinical Implications. *Ann Surg Oncol* **29**, 7354–7367 (2022).

97. Pinieux, G. de *et al.* Nationwide incidence of sarcomas and connective tissue tumors of intermediate malignancy over four years using an expert pathology review network. *PLOS ONE* **16**, e0246958 (2021).

98. Tfayli, Y., Baydoun, A., Naja, A. S. & Saghieh, S. Management of myxoid liposarcoma of the extremity (Review). *Oncology Letters* **22**, 1–11 (2021).

99. Phan, N. *et al.* A simple high-throughput approach identifies actionable drug sensitivities in patient-derived tumor organoids. *Commun Biol* **2**, 78 (2019).

100. Tebon, P. J. *et al.* Drug screening at single-organoid resolution via bioprinting and interferometry. 2021.10.03.462896 Preprint at https://doi.org/10.1101/2021.10.03.462896 (2022).

101. Nguyen, H. T. L. *et al.* A rapid platform for 3D patient-derived cutaneous neurofibroma organoid establishment and screening. 2022.11.07.515469 Preprint at https://doi.org/10.1101/2022.11.07.515469 (2022).

102. Kim, S. *et al.* PubChem in 2021: new data content and improved web interfaces. *Nucleic Acids Res* **49**, D1388–D1395 (2021).

103. Martens, M. *et al.* WikiPathways: connecting communities. *Nucleic Acids Research* **49**, D613–D621 (2021).

104. Ronneberger, O., Fischer, P. & Brox, T. U-Net: Convolutional Networks for Biomedical Image Segmentation. in *Medical Image Computing and Computer-Assisted Intervention – MICCAI 2015* (eds. Navab, N., Hornegger, J., Wells, W. M. & Frangi, A. F.) 234–241 (Springer International Publishing, 2015). doi:10.1007/978-3-319-24574-4_28.

105. Iversen, P. W., Eastwood, B. J., Sittampalam, G. S. & Cox, K. L. A Comparison of Assay Performance Measures in Screening Assays: Signal Window, Z' Factor, and Assay Variability Ratio. *Journal of Biomolecular Screening* **11**, 247–252 (2006).

106. Atmaramani, R., Pancrazio, J. J. & Black, B. J. Adaptation of robust Z' factor for assay quality assessment in microelectrode array based screening using adult dorsal root ganglion neurons. *Journal of Neuroscience Methods* **339**, 108699 (2020).

107. Narasimhan, V. *et al.* Medium-throughput drug screening of patient-derived organoids from colorectal peritoneal metastases to direct personalized therapy. *Clin Cancer Res* **26**, 3662–3670 (2020).

108. Yoo, C. *et al.* Multicenter phase II study of everolimus in patients with metastatic or recurrent bone and soft-tissue sarcomas after failure of anthracycline and ifosfamide. *Invest New Drugs* **31**, 1602–1608 (2013).

109. Said, R. & Tsimberidou, A.-M. Targeted Therapy in Cancer. in *The MD Anderson Manual of Medical Oncology* (eds. Kantarjian, H. M., Wolff, R. A. & Rieber, A. G.) (McGraw Hill Education, 2022).

110. Stacchiotti, S., Sommer, J., & Chordoma Global Consensus Group. Building a global consensus approach to chordoma: a position paper from the medical and patient community. *Lancet Oncol* **16**, e71-83 (2015).

111. Walcott, B. P. *et al.* Chordoma: current concepts, management, and future directions. *The Lancet Oncology* **13**, e69-76 (2012).

112. Juric, D. *et al.* Phosphatidylinositol 3-Kinase α-Selective Inhibition With Alpelisib (BYL719) in PIK3CA-Altered Solid Tumors: Results From the First-in-Human Study. *J Clin Oncol* **36**, 1291–1299 (2018).

113. Juric, D. *et al.* Alpelisib Plus Fulvestrant in PIK3CA-Altered and PIK3CA-Wild-Type Estrogen Receptor–Positive Advanced Breast Cancer: A Phase 1b Clinical Trial. *JAMA Oncology* **5**, e184475 (2019).

114. André, F. *et al.* Alpelisib for PIK3CA-Mutated, Hormone Receptor–Positive Advanced Breast Cancer. *New England Journal of Medicine* **380**, 1929–1940 (2019).

115. Gatalica, Z., Xiu, J., Swensen, J. & Vranic, S. Molecular characterization of cancers with NTRK gene fusions. *Mod Pathol* **32**, 147–153 (2019).

116. Davis, J. L. *et al.* Infantile NTRK-associated Mesenchymal Tumors. *Pediatr Dev Pathol* **21**, 68–78 (2018).

117. Laetsch, T. W. *et al.* Larotrectinib for paediatric solid tumours harbouring NTRK gene fusions: phase 1 results from a multicentre, open-label, phase 1/2 study. *The Lancet Oncology* **19**, 705–714 (2018).

118. Tebon, P. J. *et al.* Drug screening at single-organoid resolution via bioprinting and interferometry. 2021.10.03.462896 Preprint at https://doi.org/10.1101/2021.10.03.462896 (2022).

119. Tsuda, Y. *et al.* Impact of chemotherapy-induced necrosis on event-free and overall survival after preoperative MAP chemotherapy in patients with primary high-grade localized osteosarcoma. *The Bone & Joint Journal* **102-B**, 795–803 (2020).

120. Du, X.-H., Wei, H., Zhang, P., Yao, W.-T. & Cai, Q.-Q. Heterogeneity of Soft Tissue Sarcomas and Its Implications in Targeted Therapy. *Front Oncol* **10**, 564852 (2020).

121. Pillozzi, S. *et al.* Soft Tissue Sarcoma: An Insight on Biomarkers at Molecular, Metabolic and Cellular Level. *Cancers (Basel)* **13**, 3044 (2021).

122. Zhang, J.-H., Chung, T. D. Y. & Oldenburg, K. R. A Simple Statistical Parameter for Use in Evaluation and Validation of High Throughput Screening Assays. *SLAS Discovery* **4**, 67–73 (1999).

123. He, K., Zhang, X., Ren, S. & Sun, J. Deep Residual Learning for Image Recognition. in 770–778 (2016).

124. Deng, J. *et al.* ImageNet: A large-scale hierarchical image database. in *2009 IEEE Conference on Computer Vision and Pattern Recognition* 248–255 (2009). doi:10.1109/CVPR.2009.5206848.

125. Garcia, E. P. *et al.* Validation of OncoPanel: A Targeted Next-Generation Sequencing Assay for the Detection of Somatic Variants in Cancer. *Arch Pathol Lab Med* **141**, 751–758 (2017).

126. Ma, Y.-S. *et al.* The power and the promise of organoid models for cancer precision medicine with next-generation functional diagnostics and pharmaceutical exploitation. *Translational Oncology* **14**, 101126 (2021).

127. Drost, J. & Clevers, H. Organoids in cancer research. *Nat Rev Cancer* **18**, 407–418 (2018).

128. Bhola, P. D. *et al.* High-throughput dynamic BH3 profiling may quickly and accurately predict effective therapies in solid tumors. *Sci. Signal.* **13**, (2020).

129. Guillen, K. P. *et al.* A breast cancer patient-derived xenograft and organoid platform for drug discovery and precision oncology. *bioRxiv* 2021.02.28.433268 (2021) doi:10.1101/2021.02.28.433268.

130. Marquart, J., Chen, E. Y. & Prasad, V. Estimation of the Percentage of US Patients With Cancer Who Benefit From Genome-Driven Oncology. *JAMA Oncol* **4**, 1093–1098 (2018).

131. Kapałczyńska, M. *et al.* 2D and 3D cell cultures – a comparison of different types of cancer cell cultures. *Arch Med Sci* **14**, 910–919 (2018).

132. Jensen, C. & Teng, Y. Is It Time to Start Transitioning From 2D to 3D Cell Culture? *Frontiers in Molecular Biosciences* **7**, (2020).

133. Cheon, D.-J. & Orsulic, S. Mouse Models of Cancer. *Annual Review of Pathology: Mechanisms of Disease* **6**, 95–119 (2011).

134. Cekanova, M. & Rathore, K. Animal models and therapeutic molecular targets of cancer: utility and limitations. *Drug Des Devel Ther* **8**, 1911–1922 (2014).

135. Lee, S. H. *et al.* Tumor Evolution and Drug Response in Patient-Derived Organoid Models of Bladder Cancer. *Cell* **173**, 515-528.e17 (2018).

136. Schutgens, F. & Clevers, H. Human Organoids: Tools for Understanding Biology and Treating Diseases. *Annu Rev Pathol* **15**, 211–234 (2020).

137. Mazzocchi, A., Soker, S. & Skardal, A. 3D bioprinting for high-throughput screening: Drug screening, disease modeling, and precision medicine applications. *Applied Physics Reviews* **6**, 011302 (2019).

138. Nguyen, H. T. L. & Soragni, A. Patient-Derived Tumor Organoid Rings for Histologic Characterization and High-Throughput Screening. *STAR Protoc* **1**, (2020).

139. Daly, A. C., Prendergast, M. E., Hughes, A. J. & Burdick, J. A. Bioprinting for the Biologist. *Cell* **184**, 18–32 (2021).

140. Mao, S. *et al.* Bioprinting of in vitro tumor models for personalized cancer treatment: a review. *Biofabrication* **12**, 042001 (2020).

141. Kang, Y., Datta, P., Shanmughapriya, S. & Ozbolat, I. T. 3D Bioprinting of Tumor Models for Cancer Research. *ACS Appl. Bio Mater.* **3**, 5552–5573 (2020).

142. Liu, T., Delavaux, C. & Zhang, Y. S. 3D bioprinting for oncology applications. *Journal of 3D Printing in Medicine* **3**, 55–58 (2019).

143. Yi, H.-G. Introduction to bioprinting of in vitro cancer models. *Essays in Biochemistry* (2021) doi:10.1042/EBC20200104.

144. Huang, D. *et al.* High-Speed Live-Cell Interferometry: A New Method for Quantifying Tumor Drug Resistance and Heterogeneity. *Anal. Chem.* **90**, 3299–3306 (2018).

145. Murray, G. F. *et al.* Live Cell Mass Accumulation Measurement Non-Invasively Predicts Carboplatin Sensitivity in Triple-Negative Breast Cancer Patient-Derived Xenografts. *ACS Omega* **3**, 17687–17692 (2018).

146. Reed, J. *et al.* Rapid, Massively Parallel Single-Cell Drug Response Measurements via Live Cell Interferometry. *Biophysical Journal* **101**, 1025–1031 (2011).

147. Bon, P., Maucort, G., Wattellier, B. & Monneret, S. Quadriwave lateral shearing interferometry for quantitative phase microscopy of living cells. *Opt. Express, OE* **17**, 13080–13094 (2009).

148. Murray, G. *et al.* Application of Quantitative Phase Imaging mass accumulation measurements to research and clinical problems in cancer. in *Quantitative Phase Imaging V* (eds. Popescu, G. & Park, Y.) 49 (SPIE, 2019). doi:10.1117/12.2514597.

149. Murray, G. F., Guest, D., Mikheykin, A., Toor, A. & Reed, J. Single cell biomass tracking allows identification and isolation of rare targeted therapy-resistant DLBCL cells within a mixed population. *Analyst* **146**, 1157–1162 (2021).

150. Zangle, T. A. & Teitell, M. A. Live-cell mass profiling: an emerging approach in quantitative biophysics. *Nat Methods* **11**, 1221–1228 (2014).

151. Barer, R. Interference Microscopy and Mass Determination. *Nature* **169**, 366–367 (1952).

152. Barer, R., Ross, K. F. A. & Tkaczyk, S. Refractometry of Living Cells. *Nature* **171**, 720–724 (1953).

153. Barer, R. & Joseph, S. Refractometry of Living Cells : Part I. Basic Principles. *Journal of Cell Science* **s3-95**, 399–423 (1954).

154. Ross, K. F. A. *Phase Contrast and Interference Microscopy for Cell Biologists*. (Edward Arnold, 1967).

155. Barer, R. & Tkaczyk, S. Refractive Index of Concentrated Protein Solutions. *Nature* **173**, 821–822 (1954).

156. Chun, J. *et al.* Rapidly quantifying drug sensitivity of dispersed and clumped breast cancer cells by mass profiling. *Analyst* **137**, 5495 (2012).

157. Murray, G. F. *et al.* QPI Allows in vitro Drug Screening of Triple Negative Breast Cancer PDX Tumors and Fine Needle Biopsies. *Front. Phys.* **7**, 158 (2019).

158. Alam, A. U., Howlader, M. M. R. & Deen, M. J. The effects of oxygen plasma and humidity on surface roughness, water contact angle and hardness of silicon, silicon dioxide and glass. *J. Micromech. Microeng.* **24**, 035010 (2014).

159. Nair, K. *et al.* Characterization of cell viability during bioprinting processes. *Biotechnology Journal* **4**, 1168–1177 (2009).

160. Boularaoui, S., Al Hussein, G., Khan, K. A., Christoforou, N. & Stefanini, C. An overview of extrusion-based bioprinting with a focus on induced shear stress and its effect on cell viability. *Bioprinting* **20**, e00093 (2020).

161. Szymański, P., Markowicz, M. & Mikiciuk-Olasik, E. Adaptation of High-Throughput Screening in Drug Discovery—Toxicological Screening Tests. *Int J Mol Sci* **13**, 427–452 (2011).

162. Miles, B. & Lee, P. L. Achieving Reproducibility and Closed-Loop Automation in Biological Experimentation with an IoT-Enabled Lab of the Future. *SLAS TECHNOLOGY: Translating Life Sciences Innovation* **23**, 432–439 (2018).

163. Kroll, T. *et al.* Molecular characterization of breast cancer cell lines by expression profiling. *Journal of Cancer Research and Clinical Oncology* **128**, 125–134 (2002).

164. Dai, X., Cheng, H., Bai, Z. & Li, J. Breast Cancer Cell Line Classification and Its Relevance with Breast Tumor Subtyping. *J Cancer* **8**, 3131–3141 (2017).

165. Comşa, Ş., Cîmpean, A. M. & Raica, M. The Story of MCF-7 Breast Cancer Cell Line: 40 years of Experience in Research. *Anticancer Research* **35**, 3147–3154 (2015).

166. Lee, A. V., Oesterreich, S. & Davidson, N. E. MCF-7 Cells—Changing the Course of Breast Cancer Research and Care for 45 Years. *JNCI: Journal of the National Cancer Institute* **107**, (2015).

167. Ayoub, N. M., Ibrahim, D. R., Alkhalifa, A. E. & Al-Husein, B. A. Crizotinib induced antitumor activity and synergized with chemotherapy and hormonal drugs in breast cancer cells via downregulating MET and estrogen receptor levels. *Invest New Drugs* **39**, 77–88 (2021).

168. Bush, S. J., Chen, L., Tovar-Corona, J. M. & Urrutia, A. O. Alternative splicing and the evolution of phenotypic novelty. *Philosophical Transactions of the Royal Society B: Biological Sciences* **372**, 20150474 (2017).

169. Liu, Y. *et al.* Impact of Alternative Splicing on the Human Proteome. *Cell Reports* **20**, 1229–1241 (2017).

170. Climente-González, H., Porta-Pardo, E., Godzik, A. & Eyras, E. The Functional Impact of Alternative Splicing in Cancer. *Cell Reports* **20**, 2215–2226 (2017).

171. Chuang, T.-J. *et al.* Integrative transcriptome sequencing reveals extensive alternative trans-splicing and cis-backsplicing in human cells. *Nucleic Acids Research* **46**, 3671–3691 (2018).

172. Barer, R. & Ross, K. a. F. Refractometry of living cells. *J Physiol* **118**, 38P-39P (1952).

173. Ershov, D. *et al.* Bringing TrackMate into the era of machine-learning and deep-learning. 2021.09.03.458852 Preprint at https://doi.org/10.1101/2021.09.03.458852 (2021).

174. TrackMate: An open and extensible platform for single-particle tracking - ScienceDirect. https://www.sciencedirect.com/science/article/pii/S1046202316303346.

175. Chen, T. & Guestrin, C. XGBoost: A Scalable Tree Boosting System. in *Proceedings of the 22nd ACM SIGKDD International Conference on Knowledge Discovery and Data Mining* 785–794 (Association for Computing Machinery, 2016). doi:10.1145/2939672.2939785.

176. Tamaoki, T. *et al.* Staurosporine, a potent inhibitor of phospholipidCa++dependent protein kinase. *Biochemical and Biophysical Research Communications* **135**, 397–402 (1986).

177. Feldinger, K. & Kong, A. Profile of neratinib and its potential in the treatment of breast cancer. *Breast Cancer (Dove Med Press)* **7**, 147–162 (2015).

178. Johnston, S. R. D. & Leary, A. Lapatinib: a novel EGFR/HER2 tyrosine kinase inhibitor for cancer. *Drugs Today (Barc)* **42**, 441–453 (2006).

179. Liston, D. R. & Davis, M. Clinically Relevant Concentrations of Anticancer Drugs: A Guide for Nonclinical Studies. *Clin Cancer Res* **23**, 3489–3498 (2017).

180. Keyvanjah, K. *et al.* Pharmacokinetics of neratinib during coadministration with lansoprazole in healthy subjects. *Br J Clin Pharmacol* **83**, 554–561 (2017).

181. Gerstung, M. *et al.* The evolutionary history of 2,658 cancers. *Nature* **578**, 122–128 (2020).

182. Park, J. J. H., Hsu, G., Siden, E. G., Thorlund, K. & Mills, E. J. An overview of precision oncology basket and umbrella trials for clinicians. *CA: A Cancer Journal for Clinicians* **70**, 125–137 (2020).

183. Senft, D., Leiserson, M. D. M., Ruppin, E. & Ronai, Z. A. Precision Oncology: The Road Ahead. *Trends in Molecular Medicine* **23**, 874–898 (2017).

184. Schwartzberg, L., Kim, E. S., Liu, D. & Schrag, D. Precision Oncology: Who, How, What, When, and When Not? *American Society of Clinical Oncology Educational Book* 160–169 (2017) doi:10.1200/EDBK_174176.

185. Tiriac, H. *et al.* Organoid Profiling Identifies Common Responders to Chemotherapy in Pancreatic Cancer. *Cancer Discovery* **8**, 1112–1129 (2018).

186. Xu, R., Zhou, X., Wang, S. & Trinkle, C. Tumor organoid models in precision medicine and investigating cancer-stromal interactions. *Pharmacology & Therapeutics* **218**, 107668 (2021).

187. Veninga, V. & Voest, E. E. Tumor organoids: Opportunities and challenges to guide precision medicine. *Cancer Cell* **39**, 1190–1201 (2021).

188. Kane, K. I. W. *et al.* Determination of the rheological properties of Matrigel for optimum seeding conditions in microfluidic cell cultures. *AIP Advances* **8**, 125332 (2018).

189. Zangle, T. A., Teitell, M. A. & Reed, J. Live Cell Interferometry Quantifies Dynamics of Biomass Partitioning during Cytokinesis. *PLoS ONE* **9**, e115726 (2014).

190. Reed, J. *et al.* Live Cell Interferometry Reveals Cellular Dynamism During Force Propagation. *ACS Nano* **2**, 841–846 (2008).

191. Reed, J. *et al.* High throughput cell nanomechanics with mechanical imaging interferometry. *Nanotechnology* **19**, 235101 (2008).

192. Ledwig, P. & Robles, F. E. Epi-mode tomographic quantitative phase imaging in thick scattering samples. *Biomed. Opt. Express, BOE* **10**, 3605–3621 (2019).

193. Espiritu, S. M. G. *et al.* The Evolutionary Landscape of Localized Prostate Cancers Drives Clinical Aggression. *Cell* **173**, 1003-1013.e15 (2018).

194. Somasundaram, R., Villanueva, J. & Herlyn, M. Chapter Eleven - Intratumoral Heterogeneity as a Therapy Resistance Mechanism: Role of Melanoma Subpopulations. in *Advances in Pharmacology* (ed. Smalley, K. S. M.) vol. 65 335–359 (Academic Press, 2012).

195. Auffinger, B., Spencer, D., Pytel, P., Ahmed, A. U. & Lesniak, M. S. The role of glioma stem cells in chemotherapy resistance and glioblastoma multiforme recurrence. *Expert Review of Neurotherapeutics* **15**, 741–752 (2015).

196. Lacerda, L., Pusztai, L. & Woodward, W. A. The role of tumor initiating cells in drug resistance of breast cancer: Implications for future therapeutic approaches. *Drug Resistance Updates* **13**, 99–108 (2010).

197. Dobin, A. *et al.* STAR: ultrafast universal RNA-seq aligner. *Bioinformatics* **29**, 15–21 (2013).

198. Kim, D., Paggi, J. M., Park, C., Bennett, C. & Salzberg, S. L. Graph-based genome alignment and genotyping with HISAT2 and HISAT-genotype. *Nat Biotechnol* **37**, 907–915 (2019).

199. Chen, S., Zhou, Y., Chen, Y. & Gu, J. fastp: an ultra-fast all-in-one FASTQ preprocessor. *Bioinformatics* **34**, i884–i890 (2018).

200. Auwera, G. A. V. der & O'Connor, B. D. *Genomics in the Cloud: Using Docker, GATK, and WDL in Terra*. (O'Reilly Media, Incorporated, 2020).

201. Sayols, S., Scherzinger, D. & Klein, H. dupRadar: a Bioconductor package for the assessment of PCR artifacts in RNA-Seq data. *BMC Bioinformatics* **17**, 428 (2016).

202. Li, B. & Dewey, C. N. RSEM: accurate transcript quantification from RNA-Seq data with or without a reference genome. *BMC Bioinformatics* **12**, 323 (2011).

203. Shen, S. *et al.* rMATS: Robust and flexible detection of differential alternative splicing from replicate RNA-Seq data. *PNAS* **111**, E5593–E5601 (2014).

204. Lo Giudice, C., Tangaro, M. A., Pesole, G. & Picardi, E. Investigating RNA editing in deep transcriptome datasets with REDItools and REDIportal. *Nat Protoc* **15**, 1098–1131 (2020).

205. Uhrig, S. *et al.* Accurate and efficient detection of gene fusions from RNA sequencing data. *Genome Res* **31**, 448–460 (2021).

206. Haas, B. J. *et al.* Accuracy assessment of fusion transcript detection via read-mapping and de novo fusion transcript assembly-based methods. *Genome Biology* **20**, 213 (2019).

207. Nicorici, D. *et al.* FusionCatcher – a tool for finding somatic fusion genes in paired-end RNA-sequencing data. *bioRxiv* 011650 (2014) doi:10.1101/011650.

208. P'ng, C. *et al.* BPG: Seamless, automated and interactive visualization of scientific data. *BMC Bioinformatics* **20**, 42 (2019).

209. Huang, D. *et al.* Identifying fates of cancer cells exposed to mitotic inhibitors by quantitative phase imaging. *Analyst* **145**, 97–106 (2019).

210. Giang, I., Boland, E. L. & Poon, G. M. K. Prodrug applications for targeted cancer therapy. *AAPS J* **16**, 899–913 (2014).

211. Manikandan, P. & Nagini, S. Cytochrome P450 Structure, Function and Clinical Significance: A Review. *Current Drug Targets* **19**, 38–54 (//).

212. Skarbek, C. *et al.* Preactivated Oxazaphosphorines Designed for Isophosphoramide Mustard Delivery as Bulk Form or Nanoassemblies: Synthesis and Proof of Concept. *Journal of Medicinal Chemistry* **58**, 705–717 (2015).

213. Fleming, R. A. An Overview of Cyclophosphamide and Ifosfamide Pharmacology. *Pharmacotherapy: The Journal of Human Pharmacology and Drug Therapy* **17**, 146S-154S (1997).

214. Li, Z., Li, D., Guo, Y., Wang, Y. & Su, W. Evaluation of hepatic drug-metabolism for glioblastoma using liver-brain chip. *Biotechnol Lett* **43**, 383–392 (2021).

215. Zhang, J., Wu, J., Li, H., Chen, Q. & Lin, J.-M. An in vitro liver model on microfluidic device for analysis of capecitabine metabolite using mass spectrometer as detector. *Biosensors and Bioelectronics* **68**, 322–328 (2015).

216. Rajan, S. A. P. *et al.* Probing prodrug metabolism and reciprocal toxicity with an integrated and humanized multi-tissue organ-on-a-chip platform. *Acta Biomaterialia* **106**, 124–135 (2020).

217. Biermann, J. S. *et al. Bone Cancer*. vol. Version 1.2020 (2019).

218. Hashizume, T. *et al.* Advantages of Human Hepatocyte-Derived Transformants Expressing a Series of Human Cytochrome P450 Isoforms for Genotoxicity Examination. *Toxicological Sciences* **116**, 488–497 (2010).

219. Santos, A. *et al.* Metabolism of irinotecan (CPT-11) by CYP3A4 and CYP3A5 in humans. *Clin Cancer Res* **6**, 2012–2020 (2000).

220. Cunningham, R. P. & Porat-Shliom, N. Liver Zonation – Revisiting Old Questions With New Technologies. *Frontiers in Physiology* **12**, (2021).

221. Kietzmann, T. Metabolic zonation of the liver: The oxygen gradient revisited. *Redox Biology* **11**, 622–630 (2017).

222. Knights, K. M., Stresser, D. M., Miners, J. O. & Crespi, C. L. In Vitro Drug Metabolism Using Liver Microsomes. *Current Protocols in Pharmacology* **74**, 7.8.1-7.8.24 (2016).

223. Sia, J., Szmyd, R., Hau, E. & Gee, H. E. Molecular Mechanisms of Radiation-Induced Cancer Cell Death: A Primer. *Frontiers in Cell and Developmental Biology* **8**, (2020).

224. Lucky, S. S. *et al.* Patient-Derived Nasopharyngeal Cancer Organoids for Disease Modeling and Radiation Dose Optimization. *Frontiers in Oncology* **11**, (2021).

225. Kalbasi, A. *et al.* Uncoupling interferon signaling and antigen presentation to overcome immunotherapy resistance due to JAK1 loss in melanoma. *Science Translational Medicine* **12**, eabb0152 (2020).

226. Márquez-Rodas, I. *et al.* Intratumoral nanoplexed poly I:C BO-112 in combination with systemic anti–PD-1 for patients with anti–PD-1–refractory tumors. *Science Translational Medicine* **12**, eabb0391 (2020).

227. Horak, P., Fröhling, S. & Glimm, H. Integrating next-generation sequencing into clinical oncology: strategies, promises and pitfalls. *ESMO Open* **1**, e000094 (2016).